REVERSE DIBLOCK COPOLYMER MICELLAR GROWTH OF DESIGNER NANOPARTICLES FOR ENHANCED SURFACES

REVERSE DIBLOCK COPOLYMER MICELLAR GROWTH OF DESIGNER NANOPARTICLES FOR ENHANCED SURFACES

BY

RAMIS ARBI, B.Sc.

A THESIS
SUBMITTED TO THE DEPARTMENT OF ENGINEERING PHYSICS
AND THE SCHOOL OF GRADUATE STUDIES
OF MCMASTER UNIVERSITY
IN PARTIAL FULFILMENT OF THE REQUIREMENTS
FOR THE DEGREE OF
DOCTOR OF PHILOSOPHY

Doctor of Philosophy (2022) McMaster University
(Engineering Physics) Hamilton, Ontario, Canada

TITLE:	Reverse diblock copolymer micellar growth of designer nanoparticles for enhanced surfaces
AUTHOR:	Ramis Arbi B.Sc., (Materials Science and Nanoengineering) Sabanci University, Istanbul, Turkey
SUPERVISOR:	Ayse Z. Turak
NUMBER OF PAGES:	xxviii, 206

Abstract

Diblock copolymers like poly(styrene)-*block*-poly(2-vinylpyridine) pave the way for controllable self-assembled monolayers of nanoparticles. Using particular polymer weights and concentration, spherical micelles of PS-b-P2VP can be constructed with a non-polar PS corona and a polar P2VP core. Various precursor salts can be loaded into the core of the micelles due to interactions with the polar core which forms as the active site for nanoparticle growth. The PS corona protects the core from the atmosphere and non-polar solvents. The micelles can then act as nanobeakers for aqueous chemistry in two ways; spontaneous reactions between precursors result in nanoparticles or the trapping of precursor salts can be oxidized or reduced using polymer removal techniques like gas plasmas. In this way, reverse micelles are a facile method of growing metal, metal oxide or dielectric nanoparticles. Process parameters, such as concentration, molecular weights, nature of solvents and type of precursor salt, offer control over the periodicity and size of the monolayer of nanoparticles. Reverse micelle templating is a potentially useful nanofabrication method for tailor-made nanoparticles for use in electrical and optical devices which is not limited to form-factor of substrates. In this thesis, obstacles are identified that hinder the utility of PS-b-P2VP templated nanoparticles in device fabrication. The polymer is insulating which is detrimental to electrical applications. Additionally, the characterization of a monolayer of polymers, thus far, is limited to structural techniques such as SEM and AFM. This thesis sheds light on the mechanism of precursor loading in the micelle core, discusses the efficiency of different polymer removal techniques and uses vibrational spectroscopy for the characterization of monolayers of polymer, loaded polymer and nanoparticles. We have tested enhanced Raman methods using AFM probes to extend the resolution of normal Raman to view monolayers of empty polymers as well. Moreover, using $FeCl_3$-loaded polymer micelles, the control offered by PS-b-P2VP templated growth on the crystal structure of nanoparticles is laid bare. The usefulness of the technique is further divulged by using ordered γ-Fe_2O_3 nanoparticles in water-splitting photoanodes where they show an increased efficiency with the inclusion of nanoparticles and their periodicity. This is just an example of devices using reverse micelle templated nanoparticles, paving the way for future applications. The flexibility of this method is further revealed by constructing self-assembled Au/SnO_2 nanojunctions within the PS-b-P2VP micelle cores. This was done by exploiting the spontaneous redox reaction between $HAuCl_4$ and $SnCl_2$ in an aqueous environment, and so can be replicated for other metals and metal oxides like Pt, Pd, Ag, TiO_2 and ZnO_2. The composite nanoparticles formed exhibit a tunable size and dispersion as typically seen with PS-b-P2VP micelles and so, can be used for various applications which require metal/metal oxide junctions.

Acknowledgements

It is said that it takes a village to raise a child and there is a village of people I would like to acknowledge in helping me raise this thesis.

Dr. Ayse Turak, my supervisor, who gave me the opportunity to work on these projects and helped me navigate my way around dead ends. I would not have been able to get so far without your endless support, I am grateful to have you in my corner!

My supervisory committee, Dr. Ignatio Vargas-Baca and Dr. Oleg Rubel, for all the advice and direction over the years. Your questions helped make my studies more robust and scientific.

Muhammad Munir 'Mama' Khan, my group member, who has been by my side throughout the journey. I am glad we started together, you have been a source of immense relief and support, especially when nothing worked. My other group mates, Pedro Oliviera, Seung Il Lee, Jinglan Tan, Linan Cui and group alums, Dr. Lok Shu Hui, Kunyu Liang, Amr Ibrahim and Greg Hanta, who helped me not only with miscellaneous experiments but also provided a critical audience for my far-fetched theories.

Doris Stevanovic, Robert Laidler, and Emma Trueman, who helped me navigate the McMaster maze and enabled me to integrate myself as well as I have. Dr. Zhillin

Peng for trusting me with the SEM and all the help you provided. Dr. Alex Adronov and Dr. William Bodnaryk for all the help with the Raman spectroscope. Dr. Heera Marway for helping fix the AFM a million times. All the folks at CEDT, CCEM, Engineering Physics and McMaster University as a whole who have helped me in pushing forward.

All my friends here, Sudarshan Sharma, Dr. Atriya Biswas, Dr. Sumedh Dhale, Paramita Bhattacharyya, Connor Wong, Matt Vukovic, Dr. Dawson Bonneville, Dr. Maureen Lagos, Cameron Naraine, Bruno Frare, Tahoora Hashemi, Faizaan Sheikh, and many others, for all the laughs and shenanigans. You know who you are! All my friends who have kept me company virtually through thick and thin; a special shoutout to Ali Mahad and Usman Syed who kept me alive with all our games and chats, Fatemah Haji and Nawaal Haji who have been a source of immense emotional support and Ahlam Premjee who has heard me rant about everything and anything. You all are gems.

My parents and my siblings for their unending love and support, even when I was absent for all the big moments. You have my heartfelt gratitude for patiently standing by me as I get distracted by anything that piques my curiosity.

List of Publications

1. **Arbi, R.**, Hui, L.S., Dittrich, M., Turak, A., 2021. **Utility of far-field effects from tip-assisted Raman spectroscopy for the detection of a monolayer of diblock copolymer reverse micelles for nanolithography.** Physical Chemistry Chemical Physics 23, 11065–11074. https://doi.org/10.1039/D1CP01399H

* I am the first author of this article and my role in the paper was data collection, analysis and writing. I collected the normal Raman, inverted Raman, polarized Raman and Interference-enhanced measurements and performed the processing and analysis of the collected data from all techniques. Lok Shu Hui preformed the Surface enhance Raman spectroscopy measurements, ucTERS measurements, and the preparation of the ucTERS probes. Dr. Dittrich provided the inverted AFM/Raman spectrometer at University of Toronto and the ucTERS measurements and set-up. Under Dr. Turak's guidance, I wrote the article in its entirety, with reviews and edits from the other coauthors.

2. **Arbi, R.**, Ibrahim, A., Goldring-Vandergeest, L., Liang, K., Hanta, G., Hui, L.S., Turak, A., 2021. **Role of hydration and micellar shielding in tuning the structure of single crystalline iron oxide nanoparticles for designer**

applications. Nano Select 2, 2419–2431.
https://doi.org/10.1002/nano.202100085

* I am the first author of this article and my role in the paper was data collection, analysis and writing. I collected the Raman spectra of most samples and I did the experimental fitting, peak assignment and phase analysis for all of the samples. I was also responsible for the analysis and collection of AFM and SEM included. I also wrote the manuscript in its entirety under the supervision of Dr. Turak.The annealed samples were prepared by Amr Ibrahim and Kunyu Liang and the Raman collection for them was done by Lok Shu Hui. The QNM scans were acquired and analyzed by Greg Hanta. The DLS analysis and calculations for the Flory-Huggins parameter in the supplementary was done by Liora Goldring-Vandergeest. The EDX and TEM micrographs included in the supplementary were performed by Kunyu Liang.

3. Tokubuchi, T., **Arbi, R.I.**, Zhenhua, P., Katayama, K., Turak, A., Sohn, W.Y., 2021. **Enhanced photoelectrochemical water splitting efficiency of hematite (α-Fe_2O_3)-Based photoelectrode by the introduction of maghemite (γ-Fe_2O_3) nanoparticles**. Journal of Photochemistry and Photobiology A: Chemistry 410, 113179.
https://doi.org/10.1016/j.jphotochem.2021.113179

* I am a co-author in this article where reverse micelle templated γ-Fe_2O_3 monolayers were applied on the FTO-hematite interface of a water-splitting photoelectrode for improved charge extraction which was observed to be dependent

on the order of the nanoparticle array. I was responsible for the growth, deposition and characterization of the nanoparticles used for this study. Moreover, I was also responsible for confirming the presence of γ-Fe_2O_3 after the solvothermal deposition of hematite using Raman spectroscopy, for which a variety of substrates were analyzed before settling on MgO for a featureless background. This involved analysis, fitting and assignment of all the Raman spectra. I also performed the AFM and SEM imaging of the nanoparticle arrays and analyzed the order of dispersion using a Mathematica spatial statistics package, Dislocate. All parts of the manuscript involving the characterization of nanoparticle arrays were written by me. Moreover, I prepared the γ-Fe_2O_3 decorated FTO substrates prior to hematite deposition which was done by our co-authors at Chuo University. The electrical characterization of the devices was also performed at Chuo University.

4. Munir, M., Tan, J., **Arbi, R.**, Oliveira, P., Leeb, E., Salinas, Y., Scharber, M.C., Sariciftci, N.S., Turak, A., 2022. **Enhanced Stokes Shift and Phase Stability by Cosynthesizing Perovskite Nanoparticles ($MAPbI_3$/$MAPbBr_3$) in a Single Solution.** Advanced Photonics Research 2100372. https://doi.org/10.1002/adpr.202100372

* I am a co-author in this article and contributed in the spectroscopic measurements, experimental design and the editing for this manuscript.

5. Munir, M., **Arbi, R.**, Scharber, M.C., Salinas, Y., Sariciftci, N.S., Turak, A., 2020. **Anionic exchange route to synthesize highly uniform, stable and luminescent MAPBr nanoparticles.** Presented at the Optical Devices and

Materials for Solar Energy and Solid-state Lighting, Optical Society of America, pp. PvTu3G-5.
https://doi.org/10.1364/PVLED.2020.PvTu3G.5

* I contributed in the spectroscopic measurements, experimental design and the editing for this manuscript.

6. Munir, M., **Arbi, R.**, Oliveria, P., Hui, L.S., Bumstead, M., Hanta, G., Liang, K., Ibrahim, A., Yu, H., Turak, A., 2021. **Photonics made to order: reverse micelle templating as a universal approach to functional nanoparticles.** Presented at the 2021 Photonics North (PN), IEEE, pp. 1–2.
https://doi.org/10.1109/PN52152.2021.9597948

* I contributed to the background work mentioned in this article.

7. Hui, L., Beswick, C., Getachew, A., Heilbrunner, H., Liang, K., Hanta, G., **Arbi, R.**, Munir, M., Dawood, H., Isik Goktas, N., 2019. **Reverse Micelle Templating Route to Ordered Monodispersed Spherical Organo-Lead Halide Perovskite Nanoparticles for Light Emission.** ACS Applied Nano Materials 2, 4121–4132.
https://doi.org/10.1021/acsanm.9b00585

* I contributed by performing the relative Quantum Yield measurements for this paper.

8. Zhu, E., **Arbi, R.**, Turak, A., 2020. **Phase changes in PS-b-P2VP reverse micelles by pressurized CO2 for nanostructure deposition.** Presented

at the 2020 Photonics North (PN), IEEE, pp. 1–1. https://doi.org/10.1109/PN50013.2020.9167011

- I contributed in the spectroscopic measurements, experimental design and the editing for this manuscript.

9. Lee, S.I., Liang, K., Hui, L.S., **Arbi, R.**, Munir, M., Lee, S.J., Kim, J.W., Kim, K.J., Kim, W.Y., Turak, A., 2021. **Necessity of submonolayer LiF anode interlayers for improved device performance in blue phosphorescent OLEDs.** Journal of Materials Science: Materials in Electronics 32, 1161–1177. https://doi.org/10.1007/s10854-020-04889-0

   * I contributed by performing AFM measurements for this article.

10. Lin, N., Verma, D., Saini, N., **Arbi, R.**, Munir, M., Jovic, M., Turak, A., 2021. **Antiviral nanoparticles for sanitizing surfaces: a roadmap to self-sterilizing against COVID-19.** Nano Today 40, 101267. https://doi.org/10.1016/j.nantod.2021.101267

    * I contributed in the discussion, literature research and review of this article.

11. Bonneville, D.B., Kiani, K.M., Frankis, H.C., **Arbi, R.**, Munir, M., Turak, A., Knights, A.P., Bradley, J.D., Albert, M., Sask, K.N., n.d. **Hybrid Si-TeO2 waveguide Bragg resonators coated in PMMA for biological sensing.** Link to pre-print

    * I contributed in the surface functionalization by oxygen plasma for this experiment.

12. Saad, A., Shen, H., Cheng, Z., **Arbi, R.**, Guo, B., Hui, L., Liang, K., Liu, S., Attfield, J., Turak, A., n.d. **Mesoporous ternary nitrides of earth-abundant metals as oxygen evolution electrocatalyst.** Nano-Micro Lett. 12, 79 (2020).
    https://doi.org/10.1007/s40820-020-0412-8

* I contributed in the discussion, literature research and review of this article.

Contents

List of Figures

List of Tables

Abbreviations and Symbols

Abbreviations

PS-b-P2VP	poly(styrene)-b-poly(2-vinylpyridine)
2VP	2-vinyl pyridine
OPV	Organic Photovoltaics
LED	Light Emitting Diodes
RMD	Reverse Micelle Deposition
UV	Ultraviolet
Vis	Visible
XPS	Xray Photoelectron Spectroscopy
EDS	Energy Dispersive Spectroscopy
AFM	Atomic Force Microscopy
FTIR	Fourier Transform Infrared Spectroscopy

SPR	Surface Plasmonic Resonance
SEM	Scanning Electron Microscopy
TEM	Transmission Electron Microscopy
FTO	Flourine-doped Tin Oxide
ITO	Indium Tin Oxide
LSPR	Localized Surface Plasmonic Resonance
SPP	Surface Plasmon Polaritons
LSP	Localized Surface Plasmons
TERS	Tip-enhanced Raman Spectroscopy
SERS	Surface-enhanced Raman Spectroscopy
IERS	Interference-enhanced Raman Spectroscopy
CFSE	Crystal Field Stabilization Energy
CN	Cyanide
HOMO	Highest Occupied Molecular Orbital
LUMO	Lowest Unoccupied Molecular Orbital
QNM	Quantitative Nanomechanical Mapping
SQUID	Superconducting Quantum Interference Device

Symbols

α	Alpha
γ	Gamma
ϵ	Epsilon
β	Beta
Δ	Delta

Chapter 1

Introduction

1.1 Background and Motivation

Nanofabrication can be categorized in two main groups; "top-down" or "bottom-up" approaches. As the names suggest, the former relies on a larger structure which is either broken down or etched away to give nanostructures while the latter mainly forms the wider array of synthesis methods which rely on forming nanostructures from precursors. Nanoparticle decoration of surfaces with uniform size and ordered dispersions have been of considerable interest for applications where surface wettability, overlayer adhesion, or work function modification are desirable. Nanostructures also find widespread use for applications that exploit properties where they differ from that of their typical bulk counterparts. A smaller subset of these bottom-up approaches are self-assembly techniques using templating methods which have been a matter of great interest for their potential in easy and cheap fabrication. [1,2]

Diblock copolymer lithography relies on amphiphillic diblock copolymers which self-assemble into predictable patterns when suspended in a solvent and deposited on a surface. [3–9]Diblock copolymers such as Poly(styrene)-b-poly(2-vinylpyridine) (PS-b-P2VP) consist of two chains of copolymers bound to each other. [7–19] In the presence of a selective solvent, diblock copolymers self-assemble in different arrangements, forming the backbone of diblock copolymer lithography. [3–5, 7, 8, 20]The control over diblock copolymer lithography emerges from the interactions and self-interactions between the two polymers while in different solvents. In terms of process parameters, this comes down to concentration of solution, nature of solvent, and molecular weight of each block which can be selected for desirable phases. [3–5, 7, 8, 20, 21] Above a critical micellar concentration (C_{cmc}) in a non-polar solvent, PS-b-P2VP self-assembles as spherical micelles, where P2VP forms the polar core and PS serves as the non-polar corona. The schematic in Figure 1.1 (a) shows the arrangement of each block copolymer in a spherical micelle. The hydrodynamic radius of the reverse micelles in the solution depends on the concentration and the molecular weight of the blocks. Additive polar solvent can also be used to 'swell' the core of the micelles, which effectively increases the micelle size. Different ratios of PS/P2VP fraction leads to a different equilibrium of self-interaction of the polymer and exhibits different periodicity of the polymer micelles. By optimizing the deposition parameters, cheap and facile deposition techniques can be used to obtain ordered monolayers of self-assembled micelles as shown in Figure 1.1 (b).

The polar micellar cores forms the site of nanoparticle synthesis when the precursor is introduced to the micelle solutions. The mechanisms of loading of the micellar core is split into two main categories; interaction of the metal ions with the P2VP units and osmotic pressure forcing the diffusion of the precursor salts from the non-polar solvent to the polar core. The core surrounded by the PS shell offers the

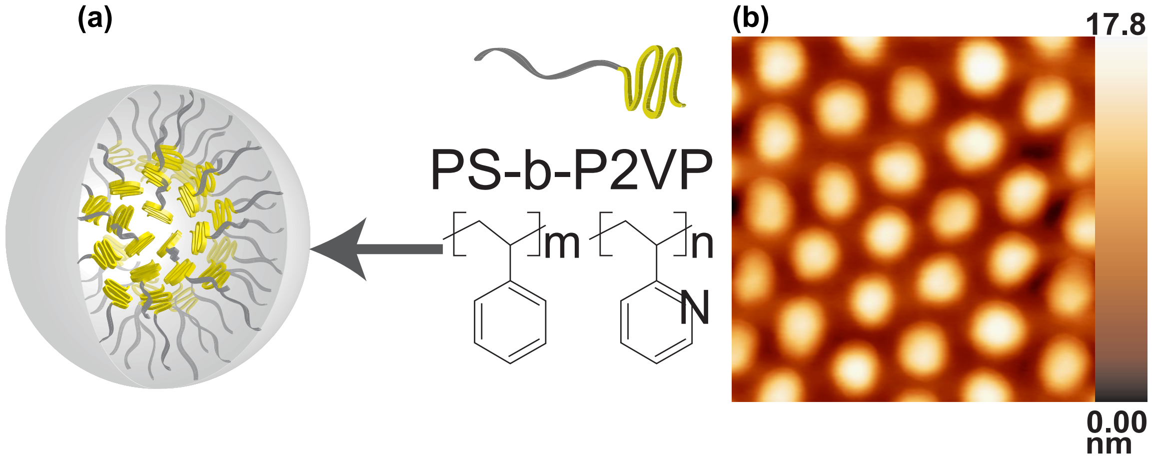

Figure 1.1: (a) Schematic of a PS-b-P2VP spherical micelle indicating the arrangement of the diblock copolymers which are indicated with the PS as a grey line and the P2VP as the yellow. (b) AFM image of a spin-coated monolayer of PS(75k)-b-P2VP(66.5k) micelles on a clean Si substrate.

precursors 'protection' from the environment, as in this way the reverse micelles act as nanosized reaction vessels for aqueous reactions resulting in desired nanoparticles. The entire process from formation of polymer micelles to nanoparticles is illustrated in the schematics Figure 1.2. Exploiting the micellar phase of PS-b-P2VP, a variety of metal, metal oxide and dielectric nanoparticles have been formed.

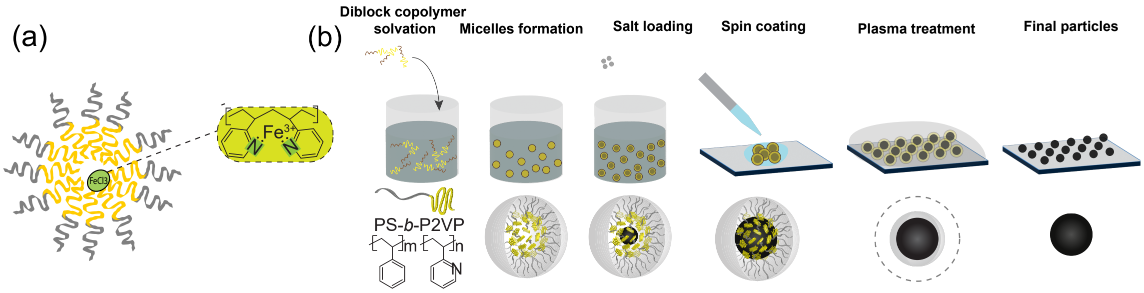

Figure 1.2: Schematic of (a) a single $FeCl_3$-loaded PS-b-P2VP micelle, indicating the trapping of the metal ion in the core and (b) reverse micelle deposition process including polymer removal from a monolayer to produce templated nanoparticles.

The use of PS-b-P2VP micelle templated nanoparticle arrays in devices is limited due toa few reasons. The presence of insulating polymer surrounding nanoparticles poses n obstacle for applications where electrical contact between layers is desirable. Moreover, the ability to characterize small amounts of material, down to monolayers, is important to assess the role of nanoparticles in any application. Typically, structural characterization like AFM can be used to visualize the topographical features of nanoparticles as in Figure 1.1 (b). They are extermely useful for structure sizes and elemental analysis but these techniques are limited in their ability to probe chemical properties such as molecular vibrations. Techniques like AFM and SEM are also costly and effort-consuming compared to non-invasive spectroscopic techniques such as Raman Spectroscopy which resolve fingerprint scattering patterns to identify structures. Normal Raman spectroscopy cannot, however, only resolve modes from monolayer of PS-b-P2VP micelles. To effectively use PS-b-P2VP reverse micelles as a method of producing ordered arrays of nanoparticles and use them in devices, there must be a good understanding of the mechanisms of polymer loading, polymer removal and there must be a cheap and reliable way of characterizing thin films just structural analysis.

1.2 Overview of thesis

The following thesis is a combination of published work or work that is in the process of being published and with these articles, I hope to shed light on the viability of using diblock copolymers for self-assembled templated nanoparticles. This technique can be employed for the synthesis of a nanoparticles of different materials and, therefore, is useful for a variety of applications. Reverse Micelle deposition is also enticing for its flexibility in deposition for a variety of solution-deposition methods such as spin-coating, spray-coating, dip-coating, and roll-to-roll printing can be used.

I have attempted to address challenges in the growth and use of PS-b-P2VP templated monolayers of nanoparticles; Chapter 2 discusses polymer removal and its effect on the resulting nanoparticles while Chapter 3 expands on our ability to visualize the polymer at different points of the process and discusses the ability of viewing monolayers of loaded micelles. This ability to characterize small amounts of materials and to track polymer removal opens the avenue for control and monitoring the entire process. Chapter 3 also discusses the ability to characterize and synthesize various transition metal oxides and noble metal nanoparticles using metal halide precursors.

Chapter 4 exhibits our understanding of the system in terms of the control offered over monolayers of Fe_2O_3 nanoparticles, allowing us to control the amount of each polymorph (hematite, maghemite and magnetite) grown and this, in turn, allows us to tune the particles for specific applications. The usefulness of this ability is illustrated in the second article in Chapter 4 which employs ordered and disordered arrays of γ-Fe_2O_3 nanoparticles in hematite-based photoelectrodes for water splitting. With this article, we can see the effect of enhanced charge extraction on current density due to the α/γ-Fe_2O_3 junction. Ordered nanoparticles are observed to deliver a greater efficiency. This chapter forms an example of the possibilities that this technique offers in tailor-making nanoparticles that can be used in devices.

Chapter 5 extends the discussion to the use of reverse micelle templating for the growth of composite nanoparticles. In this case, we have reported successful growth of SnO_2-Au nanoparticles which can easily be characterized using spectroscopic methods such as XPS, Raman and UV/Vis spectroscopy. By controlling the amount of precursors, the size of nanoparticles and their properties were tuned. This included optical properties and magnetic properties. We discuss the merit of SnO_2-Au nanoparticles for use in catalysis where greater surface area from hexagonally packed nanoparticles would be a boon and in photonic applications where we observed a decreased loss in waveguide transmission when the nanoparticles were used as a cladding layer. This chapter serves to outline the flexibility of the PS-b-P2VP system in making designer novel structures and its applicability to device fabrication.

Due to the inclusion of articles that are published or in the process, there is a significant overlap in the introduction and experimental methods in all the chapters. The introduction of each paper discusses the merits and, where relevant, the challenges of using Reverse Micelle templating for the growth of nanoparticles. Discussions on the different kind of nanoparticles that are possible using this method has also been included. In case of the experimental methods, similar techniques were employed in the characterization of the template and the nanoparticles, ranging from vibrational spectroscopy to electron and force microscopy, and so there is some overlap in the discussion of the characterization of empty and loaded polymer.

Chapter 2

Removal of polymer template from deposited layers

2.1 Submitted: Effectivity of Plasma Etching on Template Removal of Reverse Micelle Deposited Nanoparticles

Declaration

Effectivity of Plasma Etching on Template Removal of Reverse Micelle Deposited Nanoparticles

Authors: Ramis Arbi, Muhammad Munir, David Hoyle, Staz Dogel, and Ayse Turak

This manuscript has been submjtted to **Elsevier Polymers** awaiting review.

2.1.1 Introduction

Over the past two decades, nanometer-sized materials and devices have attracted much research interest, due to the wide variety of prospective applications of nanomaterials in electronics, high-density data storage, chemical sensing, drug delivery, medical diagnostic systems, and nanocatalysis [22–27]. The explosive growth in solution processed semiconductors has also driven new emerging technologies with organic, hybrid, perovskite and all inorganic-nanoparticle systems developing significantly over the last four decades due to the promise of cheap, flexible displays and lights and the sources to power them. Though they have impacted the consumer landscape, such devices have not dominated the market as has been long predicted, as a roadblock in effective nanoparticle device development is homogeneity, uniformity and effective size control, in the materials and at various interfaces [28].

Uniformity and periodicity of nanoparticle arrays is essential particularly in controlling electrical [15, 29–32], optical [12, 33, 34] and catalytic properties [35] of decorated surfaces and interfaces. Self-assembly of amphiphilic block copolymers is a model example of a "bottom-up" approach to the construction of nano-objects on large areas. Di-block copolymers, due to their amphiphilic nature, spontaneously form core-corona micelles in selective solvents. Using the micelles as "nanoreactors" allows the formation of highly controllable nanoparticles for a wide variety of materials [11–17]. One widely used system is poly(styrene)-b-poly(2-vinyl pyridine), where pyridine acts as a monodentate ligand for a variety of transition metal and halogen ions [36]. For many applications, however, post-processing is required to remove the polymer ligand shell from around the nanoparticle, as it can interfere with the electrical or catalytic properties.

Plasma etching, with reactive or inert gases, is an attractive low temperature option, as it is possible to remove the polymer template without losing the periodicity of the particle array [8,13,14]. Oxygen plasma in particular is effective due to reactive ion species which aid in its oxidative polymer cleaving action where the large organic structures fragment selectively into smaller volatile fractions [37–39]. It is typically selective towards the polymer and other organic molecules, leaving the inorganic nanoparticles unaffected, but often resulting in an oxygen terminated surface [40, 41]. However, the use of oxygen plasma can be detrimental for oxygen sensitive materials, such as metals, halides, or organic component containing hybrids. It can also be problematic for applications which involve nanoparticle decoration of organic active layers such as in organic optoelectronic devices [42]. This suggests the need to understand the plasma process and any alternative approaches for removing diblock copolymers as a template.

Amongst the many techniques at our disposal for examining the fabrication process of micelle templated particles, Raman spectroscopy is particularly useful in its ability to characterize the polymer micelles in small quantities [17, 43, 44]. Additionally, with transition metal salts such as iron chloride, a complex occurs with the nitrogen on the 2VP groups in the core of the micelles, which results in the enhancement of the ring stretching modes of the P2VP ring [43,45]. This allows for a unique opportunity to observe the changes in the Raman spectra of a monolayer of loaded micelles after progressive polymer removal to track the evolution of both polymer and oxide modes [17,43]. As various polymorphs of iron oxide exhibit distinct modes under Raman [17,46,47], the resulting phase of the nanoparticles after polymer removal, therefore, provides further insight about the mechanism of oxide growth.

In this contribution, we use the chemical fingerprints from Raman spectroscopy to compare the impact of oxygen plasma on iron chloride loaded reverse micelle templates and compare it to other gas plasmas in terms of its effectivity and action on the polymer. We have also extended the discussion to include two non-plasma related methods, UV/ozone assisted etching and electron cloud assisted etching, to assess their viability as polymer removal methods.

2.1.2 Materials and Methods

Reverse Micelle Preparation and Deposition

Polystyrene-block-poly(2-vinyl pyridine) powders (PS-b-P2VP, Polymer Source) of molecular weight, Mn: 750000-b-66500, were used for this study (also referred to as dense-core micelles). Where indicated, another polymer of weight, Mn: 28000-b-36000, was also used and labelled as crew-cut micelles. The polymer was dissolved in o-xylene, which is a selective solvent for PS, to a concentration of 3mgml^{-1}. The solutions were stirred for 24 hours, following which a precursor salt (in this case, anhydrous $FeCl_3$, 99.99 %, Sigma-Aldrich) was added. A loading ratio (salt:2VP) of 1.5 was used for this study to ensure strong complexation features in the Raman study. After an additional 24 hours of stirring, the solution as centrifuged for 15 min at 6500 rpm to separate the excess salt.

The loaded micelle solution (M/PS-b-P2VP) was then dynamically spin-coated at 2000 rpm for 45 seconds on to clean substrates. For SEM and AFM measurements, silicon substrates were used and for Raman measurements, aluminum foil substrates taped on glass were used.

Polymer Removal

Plasma Treatment

M/PS-b-P2VP films were introduced to different plasmas for varying amounts of time at a fixed chamber pressure in a RF plasma chamber (29.6W, Harrick), as listed in Table 2.1. Pure gases were alpha grade, used directly without drying.

Table 2.1: Chamber pressure under different gas environments for plasma treatments.

Gas	Chamber Pressure (mTorr)
Oxygen	800-900
Nitrogen	800-900
Argon	400-500
Hydrogen	1000

Mixed gases were achieved with 100mTorr of air being leaked into the chamber while maintaining the net chamber pressures listed in Table 2.1 for samples indicated as leaky O_2 or leaky N_2.

Hitachi ZoneSEM (UV/Ozone) Treatment

Hitachi Zone SEM Desktop Sample cleaner was used in multiple steps of 30 minutes of exposure under ultimate chamber vacuum using 1 min exposure intervals. The settings used offered the maximum power and exposure of the instrument. [48]

Hitachi Sparkle EC (Electron Cloud) Treatment

Hitachi Sparkle EC was used where the sample was irradiated with an electron cloud under ultra-high vacuum conditions ($< 10^{-9}$ Torr) and the vent of the chamber was connected to a residual gas analyzer (RGA) allowing for active monitoring of the fragments of selected masses, including CO_2 at 44 units. [49, 50]

Characterization

Raman Spectroscopy

Raman spectroscopy was performed by a Renishaw inVia spectrometer at 514 nm laser excitation on spin coated samples on Al foil. The laser power was set to 1 mW and an objective of 20x and 1800 Lines.mm^{-1} grating was used. The baseline of the spectra was created and then subtracted to highlight the peaks of interest. In addition, the spectra were smoothed using a Savitzky-Golay function in Origin and normalized in the region between 150 to 2000 cm^{-1}. The spectrum features were deconvoluted using Lorentzian line shape profiles to highlight the iron oxide characteristic peaks. The spectra were normalized in two ways and indicated as such: either between 0 and 1 for most analysis; or divided by the absolute intensity at 1000 cm^{-1} for the etch time study.

Scanning Electron Microscopy and Atomic Force Microscopy

To determine the micelle or nanoparticle sizes after deposition, scanning electron microscope (SEM) and AFM measurements were performed. SEM micrographs were obtained with a FEI VERSA 3D using an accelerating voltage of 5kV - 10kV and probe current of 12 - 27 pA. The images were analyzed using ImageJ.

Atomic force microscopy (AFM) micrographs were collected using an Asylum MFP-3D instrument (Oxford Instruments AsylumResearch) in alternating current (AC) mode under ambient environment. AFM probes(Nanotools, EBD-NCH) with a spring constant of 40 N m $^{-1}$ and a resonance frequency at 330 kHz were used in non-contact tapping mode for surface scans. AFM images were analyzed using WSxM 5.0. [51]

2.1.3 Results and Discussion

Raman spectroscopy is a versatile tool which can provide detailed information of the material based on the vibrational modes of the phonons. Using the Raman signatures of the precursors, the co-polymers and the various iron oxide polymorphs, we have previously performed a comprehensive analysis of the formation of iron oxide nanoparticles using $FeCl_3$ and poly(styrene)-block-poly(2-vinyl pyridine) (PS-b-P2VP) [17,43,45]. One factor that has enabled the study of the step by step evolution and dynamics of this process is the Raman visibility of all the moeities involved, from the as-received polymer to the final iron oxide nanoparticles. Of particular benefit is the emergence of a chemical fingerprint of the complexation of the nitrogen on the 2VP groups in the core of the micelles with transition metal salts, which results in the enhancement of the P2VP ring stretch modes over the PS ring breathing modes [43, 45]. These features can then be tracked over time to confirm complete polymer removal from a monolayer of salt loaded reverse micelles and the establish a consistent endpoint for the nanoparticle formation process. In the case of iron chloride loaded polymers, the endpoint is indicated by the presence of iron oxide Raman modes and absence of any polymer modes [17, 43].

Figure 2.1 (a) shows a schematic of the sequence of events that occur during the oxygen plasma etching of iron chloride loaded PS-b-P2VP micelles, to assist with the visualization of the process, mirrored by the Raman spectra in Figure 2.1 (b). The loaded micelles show the characteristic features associated with the complexation of iron chloride with P2VP (black curve in Figure 2.1 (b)): P2VP ring stretching modes (ν(19b), ν(19a), ν(8b) and ν(8a) in Wilson's numbering [52–54]) between 1480 and 1600 cm^{-1} [17, 43, 45], and twisting modes of the P2VP backbone backbone (γ(CH2) centered around 1320 cm^{-1}. A shoulder peak is also visible around 1150 cm^{-1}, which can be attributed to the CH-in plane bending in P2VP ring [45]. As the plasma interacts with the loaded micelle, these features slowly start to decrease in intensity as the polymer is etched away. In the case of iron chloride loaded micelles, after 15 mins in an oxygen plasma (green curve in Figure 2.1 (b)), there is the emergence of two modes at 700 cm^{-1} and 335 cm^{-1}, corresponding to γ-Fe_2O_3 [17]. After continuing plasma exposure, polymer related features decrease and the iron oxide related features increase until the endpoint is reached after 40 min (cyan curve in Figure 2.1 (b)), when no polymer features can be observed. Further plasma exposure results in a slight decrease in the intensity of the iron oxide related spectral features.

The polymer could also be visualized under the SEM and AFM therefore that was used to simultaneously confirm the removal of polymer. The loaded micelles and oxygen etched nanoparticles as observed under the SEM are given in Figure 2.1 (d) and (e) respectively, showing the polymer encapsulated salt converted into the iron oxide nanoparticles of smaller diameter. AFM imaging at intervals of polymer removal (shown in Figure SI-1) show a decreasing size of particle upto a particular etching time beyond which no further size reduction was observed, which was taken as the nanoparticle formation endpoint. The endpoints observed by AFM agreed with the time stamps at which the complexation peaks disappear in the Raman spectra. Complete removal of the polymer can also be confirmed by elemental analysis in XPS, by tracking nitrogen in the pyridine ring in the core of the micelles. As can be seen in Figure SI-2, the XPS signal for the N1s peak can be observed for loaded micelles, decreasing in intensity with plasma interaction with the polymer until it disappears after complete polymer removal. This again coincides with the Raman predicted enpoints for the nanoparticle formation process.

This distinct behaviour observable in the Raman spectra allows for the different steps of the polymer removal process to be quantified. This can be done by plotting the decay of the resonant pyridine ring stretch mode (2VP) around 1600 cm^{-1} against etching time. This approach is more reliable in comparison to following the emergence of Fe_2O_3 peaks, as it allows confirmation of the selective removal of the polymer rather than just isotropic surface removal. In the latter case, the forming nanoparticle layer could act as a mask, in which case the Fe_2O_3 and loading peaks would coexist, leaving no reproducible method of establishing the endpoint of the process.

To maintain internal consistency, the area of the 2VP peaks were quantified by normalizing the spectra with respect to the intensity at 1000 cm^{-1}. For samples with polymers, this mode represents the dominant PS mode and for samples with no polymer, this mode represents the intensity of the background at that wavenumber. For completely removed polymer, the intensity at the complexation 2VP modes was the same as the background, therefore it is possible to use the normalized area ratio to measure the declining 2VP peaks with respect to etching time. For each process therefore, the end point is defined similarly as the point when the 2VP mode area was the same as the background and well-defined iron oxide related modes exist. To our benefit, various polymorphs of iron oxide exhibit distinct modes under Raman. The resulting phase of the nanoparticles, therefore, provides further insight about the mechanism of oxide growth under different conditions [17].

Different techniques were applied to the particle arrays progressively and the samples were characterized at various intervals to track the removal of polymer. Figure 2.1 (c) shows the percentage area of the fitted mode of the 2VP fraction of the polymer at different time steps of treatment. This allows direct comparison of the polymer removal speed of the different techniques.

Assorted Plasmas

As illustrated in Figure 2.1 (c), going from a loaded micelle of monolayers to nanoparticles takes 25 min to remove with both N_2 and O_2 mixed with leaked air (leaky N_2 and O_2), while using just the pure gases individually took longer than 40 min (40min and 50 min for O_2 and N_2 respectively). The changes in the Raman spectra with respect to exposure time follow the same pattern with slight differences in the final phase of Fe_2O_3 nanoparticles in leaky and pure O_2 and N_2 gases.

For the different plasma exposures, the unetched spectra initially shows the PS mode at 1000 cm^{-1} and the 2VP loading peaks between 1150 and 1600 cm^{-1}. The first observation after a short exposure is the loss of the PS mode, following which after about 10-15 min the 2VP peaks reduce in intensity while γ-Fe_2O_3 emerge around 300 cm^{-1} and 700 cm^{-1}. Further exposure to plasma results in complete removal of the polymer as 2VP peaks disappear and Fe_2O_3 modes remain.

The differences between N_2 and O_2 plasma action on the polymer removal process can be seen in the phases of the resulting nanoparticles as shown in Figure 2.1 (f). We have previously observed that in oxygen plasma, the predominant phase is spinel γ-Fe_2O_3 with some Fe_3O_4 [17, 43], as shown in Figure 2.1(f). Quantification of the phases was done using the same method as used previously in Arbi et al. [17] where the area of the fitted peaks were compared. In all four cases, spinel iron oxide was formed at the end point of the etching process. Additional air in an O_2 plasma has little impact on formation of iron oxide phases. In the case of N_2 plasmas, a higher ratio of Fe_3O_4 to γ-Fe_2O_3 was observed than for that in O_2 plasmas. This would be expected as Fe_3O_4 is an oxygen deficient iron oxide phase, with arbitrarily distributed cation vacancies forming at octohedral sites [55]. Etching in pure N_2 plasma shows the highest amount of Fe_3O_4.

O_2 and N_2 are expected to produce dominantly reactive plasmas, where highly reactive ionic O^+ and N^+ species are formed. In a reactive plasma, the highly energetic ions bombard the polymer, typically dissociating a C-H bond to produce a radical polymer species. An oxygen ion or molecule can react at this site to form a peroxide radical which can then form a hyperoxide with reaction of adjacent carbons [56]. These volatile fragments then can cleave off, removing the hydrocarbon, through a chemical etching process [57].

In the case of leaky plasmas, the mixture of gases with different breakdown voltages leads to reactive ion etching. Reactive ion etching combines plasma etching by a reactive gas plasma and sputtering etching by an inert gas plasma [38, 58, 59]. In the reactive etching case, the bombarding sputtering species are removing a inhibitor layer that forms as a result of the lower energy reactive ions, which are the selectively interacting with the polymer. Typically, the combination of ion bombardment to dissociate the bond with an inert gas, with a reactive chemical etching with volatile oxygen species, results in faster etching than either alone [60]. The presence of impurities in the plasma gas can also increase the degree of oxygen dissociation, again enhancing the etching effect [61]. This results in the faster removal of polymer with leaky gas plasma as opposed to the pure gas plasma, as expected for mixed gas plasmas.

For contrast, we also examined argon as a source of inert plasma species, which would remove polymer purely by energetic bombardment. As a consequence of random ionic bombardment without the accompanying oxidation, the action of the plasma was observed to be nonuniform over the entire surface. This lead to complete removal of all materials randomly over the surface or incomplete removal of polymer. The Raman spectra of Ar etched samples show the reduction of the polymer peaks without a proportional increase in Fe_2O_3 peaks as observed for the other plasmas, and therefore was not included in Figure 2.1 (c). On the contrary, increased exposure to Ar plasma led to the reappearance of the symmetric ring breathing PS mode at 1000 cm^{-1} and the spectra at the 50 min mark shows a mix of α-Fe_2O_3 and γ-Fe_2O_3 phases (as shown by the dotted pink and green lines, respectively, in Figure 2.2). We have previously observed that when it is not adequately shielded from the ambient environment by the micelle $FeCl_3$ will preferentially form α-Fe_2O_3 [17]. The observed behaviour with Ar plasma suggests some removal of the groups giving rise to the loading peaks, i.e. 2VP and $FeCl_3$, but potentially that the PS parts of the polymer remain. Additionally, the appearance of α-Fe_2O_3 suggests oxidation of the loaded salt after exposure to the ambient environment following the plasma treatment, rather than during plasma processing. This confirms the dual role that an oxygen plasma plays in the formation of some metal oxide particles – for iron oxide formation, the oxygen plasma simultaneously removes the polymer and oxidizes the entrapped salt. Additionally, it give some insights into the effect of the plasma on the polymers themselves. Typically in an O_2 plasma, the polymer peaks disappear starting with PS with the slower diminishing of 2VP loading peaks, whereas the opposite occurs in the Ar plasma case. This suggests that polymer oxidation plays a major role in the fractionation of PS, while P2VP, particularly with complexated with the metal, is more vulnerable to pure ionic bombardment.

H_2 plasma was also used as a reactive ion plasma, however, the endpoint of plasma removal could not be reached in the times tried for this study. At the 50 minute mark, iron related peaks have just started to appear and a reduction in the 2VP loading peaks can be observed. However, the polymer peaks are the dominant modes in the spectra, with even the PS ring breathing mode at 1000 cm^{-1} still visible. As observed under the SEM (see Figure SI-3), a significant decrease in the size of loaded micelles is observed after 50 minutes of exposure, suggesting that the plasma does have an effect on the loaded micelle system. As H_2 plasma is a reducing plasma, Fe metal might be expected to evolve as a result of the plasma process rather than iron oxide. Metallic iron does not show a change in polarizability or optical phonons and is, therefore, Raman invisible. In this case, the existence of polymer peaks suggests incomplete polymer removal over the duration tried, rather than formation of iron nanoparticles. Regardless of the form of the final particles, the Raman behaviour suggests that the H_2 plasma is the slowest of the gas plasmas used in this study.

Dependence on Molecular Weight of the polymer

Previously we have determined that different molecular weight PS-b-P2VP polymers, with the same ratio of PS to P2VP units, can be classified in their ability to protect the metal salt against hydration [17]. Dense-core polymers with higher molecular weight offer stiffer micelles and greater protection of the salt compared to lower molecular weight crew-cut micelles. The ability to protect the salt results in different phases of iron oxide: dense core micelles produce γ-Fe_2O_3 nanoparticles due to an absence of hydration in the core while crew cut micelles produce α-Fe_2O_3 nanoparticles. The larger and less stiff micelles are not able to protect $FeCl_3$ from hydration, which results in the formation hydroxides inside the micelle, which in turn result in α-Fe_2O_3 dominant nanoparticles under oxygen plasma etching [17].

Studying the progressive removal of polymer using O_2 from the two kinds of polymer micelles, as displayed in Figure 2.3, we can observe that the polymer peaks disappear much faster with strong iron oxide modes for α-Fe_2O_3 appearing after just 10 min for the lower molecular weight micelles. The endpoint of the process occurs at the 25 min etch mark for crew-cut as opposed to 45 minutes for the higher molecular weight dense-core micelles.

This behaviour can be explained in terms of the molecular weight of the two polymers. The molecular weight of the polymer is due to the number of styrene and 2-vinyl pyridine monomers that make up the entire polymer chain. As the dense-core micelles are formed using the heavier molecular weight polymers, and therefore have a higher number of monomers, the time taken to completely remove the polymer takes longer.

Plasma compared to other methods

We have also compared the plasma action to other low temperature techniques that are used for the fractionation and removal of organic contaminants for surface cleaning. We compared the effect of exposure to UV/ozone treatment (Hitachi Zone) and the recently developed electronic bombardment technique (Hitachi Sparkle) [49, 50].

Raman spectra of a monolayer of the Fe-loaded micelles after progressive treatment by both techniques are displayed in Figure 2.4. In the case of Zone, complete removal of the polymer with the emergence of γ-Fe_2O_3 modes took more than 16 hours, compared to less than an hour observed with reactive plasmas. We also examined thicker drop-cast samples (not shown), which required more than 60 hours of exposure, compared to 6 hours in an O_2 plasma.

Previous studies indicate that the effect of UV exposure on PS can lead to either cross-linking or scission, depending on the availability of oxygen and the exposure time. [62, 63] With the Hitachi Zone, we are utilizing UV in the presence of reactive oxygen species which should ideally lead to fragmentation and removal of the polymers. However, the Raman spectra is unchanged up to 6 hours expsure. After 6 hours, γ-Fe_2O_3 peaks began to emerge, and coexist with the complexated 2VP polymer modes. After continued exposure, the polymer peaks eventually reduce in intensity with the iron oxide modes increasing. As can be seen in Figure 2.4 (a), even after exposure times of up to 12 hours, the characteristic PS peak is observable with the Fe_2O_3 peaks. This suggests that beyond 6 hours is when the polymer blocks start being removed allowing for oxidation of the precursor salt. For shorter intervals, it is possible that the polymer is just being crosslinked. The emergence of γ-Fe_2O_3 nanoparticles is as would be expected in the rich oxygen species environment consisting of ozone as part of the mechanism of Zone etching.

In the case of Sparkle, where the sample was exposed to an electron beam, the run cycle was limited to 6 hours. As can be seen in Figure 2.4 (b), α-Fe_2O_3 peaks are just starting to emerge, nearly at the detection limit of the instrument, with the loaded polymer peaks still visible. Though the data in Figure 2.4 (b) is normalized, the relative intensity of the complexated peaks was seen to have decreased relative to the other visible peaks. As RGA spectra could be measured at the vent of the Spark EC chamber simultaneously with the electron bombardment, we examined the masses of any fractionated polymer evolving during the experiment (see Figure SI-4). A sharp decrease for the masses of 44 and 69 were observed in the RGA spectra after 6 hours exposure, at the same time as the iron oxide peaks emerged. This suggests that after 6 hours of exposure, the salt-loaded cores of the loaded micelles were exposed enough such that the thermodynamically stable α-Fe_2O_3 formed with the polymer-loaded $FeCl_3$ upon exposure to air during the Raman measurement, as also observed for crew-cut micelles and for Ar plasma etching. The exposure to the electron beam is performed under a vacuum environment and therefore, Sparkle EC is one of the few techniques which does not have a high energy oxygen environment. Similar to that observed for Ar etching, α-Fe_2O_3 dominant nanoparticles are formed. However, in this case, it appears that the micellar structure may have been disrupted by the electron bombardment, but that there was no significant removal of either PS or P2VP species.

2.1.4 Conclusion

In this article, we have discussed different methods of polymer removal for di-block copolymer micellar templates for nanoparticle depotion and assessed their effectivity in terms of removal mechanism and time. For that purpose, we have used Raman spectroscopy of $FeCl_3$-loaded polymer as a screening tool in this study. $FeCl_3$-loaded polymer shows enhanced P2VP Raman modes that allow tracking of the progression of polymer removal and nanoparticle formation throughout the entire formation process. Polymer removal is observable by the evolution of Raman features of the samples measured at various intervals. We have used reactive ion plasma (O_2 and N_2), reductive plasma (H_2) and inert plasma (Ar) in progressive intervals and analyzed the changes in relative Raman mode intensities of the loaded polymer. We discovered that reactive ion plasmas are the fastest way to remove the polymer, with mixed gases showing the shortest polymer removal times. H_2 had the slowest rate of polymer removal, with barely any change in the complexation peaks after the same length of plasma exposure as O_2 and N_2 required to completely remove the polymer. We have also used the same method to evaluate other methods to remove polymer such as UV/ozone exposure (Hitachi Zone) and electron bombardment (Hitachi Sparkle). Both these methods are considerably slower than any of the plasmas.

Interestingly, as the polymer removal method needs to serve two roles during the fabrication process for iron oxide nanoparticles, we observed different iron oxide polymorphs arising from various techniques. When there was abundant oxygen species during polymer removal (O_2, N_2, Zone), spinel phases were formed. Where the plasma did not participate in the oxidation of the precursor salt and $FeCl_3$ was exposed to the environment with polymer removal (Sparkle, Ar, H_2), αFe_2O_3 was formed. Comparing the effect of reactive and inert sputtering gases shows that polymer oxidation plays an important role in PS fractionation, while P2VP is more vulnerable to pure ionic bombardment. Using the characteristics peaks of Fe/PS-b-P2VP complexation in Raman as a fingerprint has proved insight into the nature of micellar removal under different conditions.

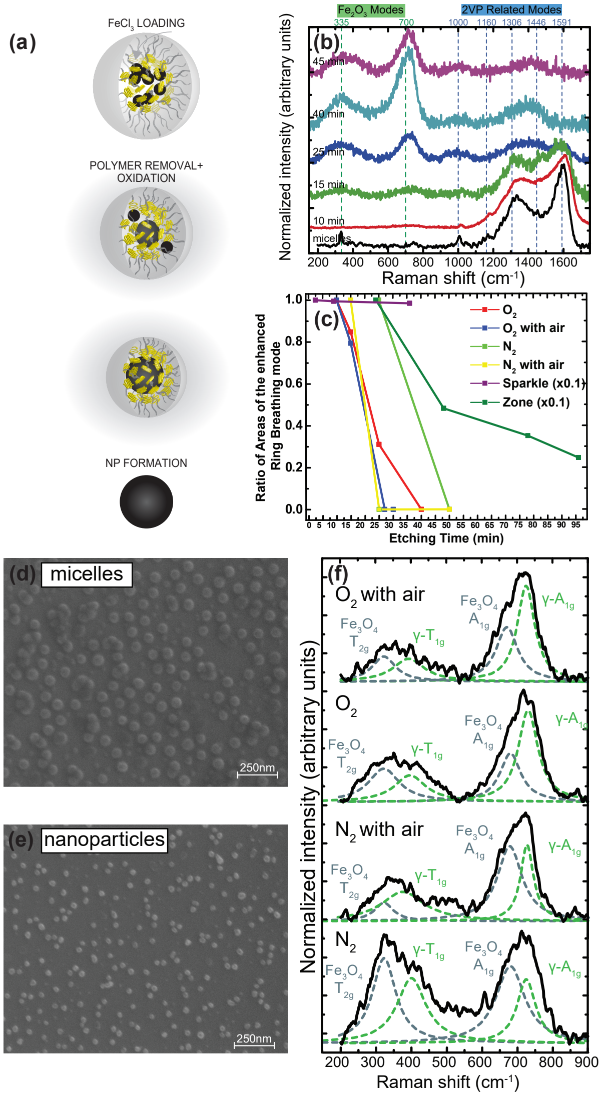

Figure 2.1: (a) Schematic of the loaded micelles, illustrating the removal of polymer by oxygen plasma. (b) Raman spectra of Fe/PS-b-P2VP micelle films at different times using oxygen plasma, normalized with respect to the intensity at 1000 cm^{-1} (c) Ratio of fitted breathing modes during etching for different techniques (d) SEM of Fe/PS-b-P2VP micelle film before plasma treatment, and (e) Fe_2O_3 nanoparticles after oxygen (with air) plasma treatment of 25 min. (f) Raman Spectra of iron oxide nanoparticles after complete polymer removal with Oxygen and Nitrogen plasmas, with and without leaked air, showing the fitted γ-Fe_2O_3 and Fe_3O_4 modes.

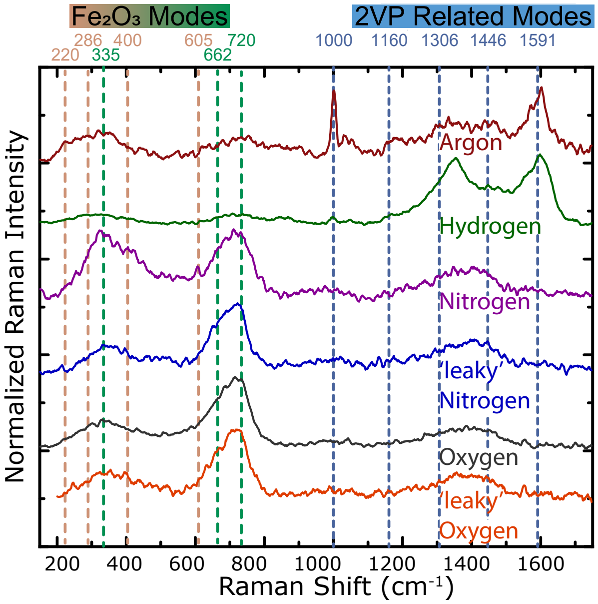

Figure 2.2: Raman spectra obtained after different gas plasma treatments of arrays of Fe/PS-b-P2VP micelle films after 50mins or at the process endpoint in each case.

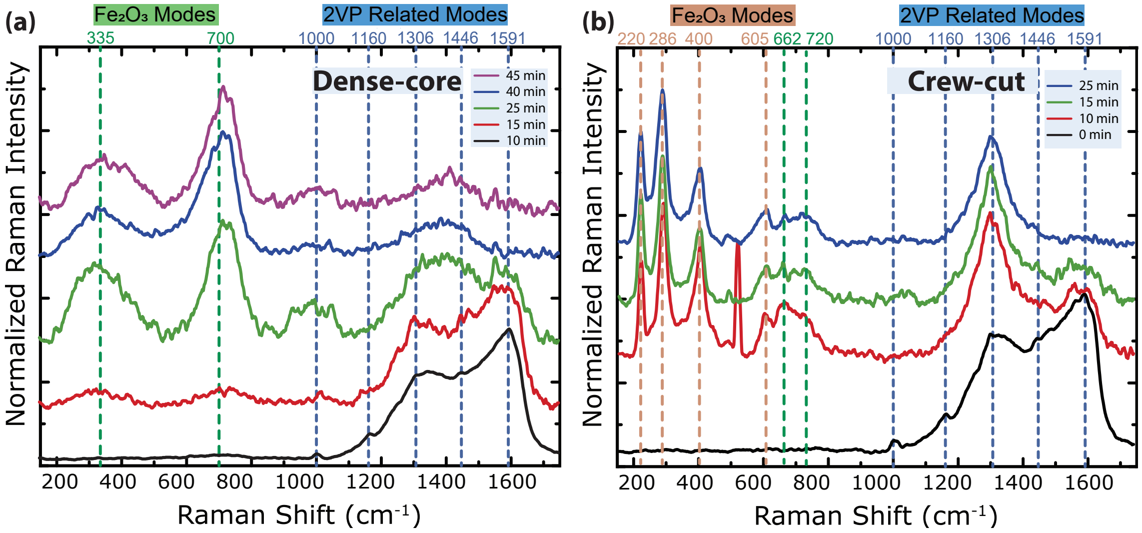

Figure 2.3: Raman spectra of Fe/PS-b-P2VP micelle films formed using dense-core and crew-cut micelles stacked with respect to oxygen plasma treatment time.

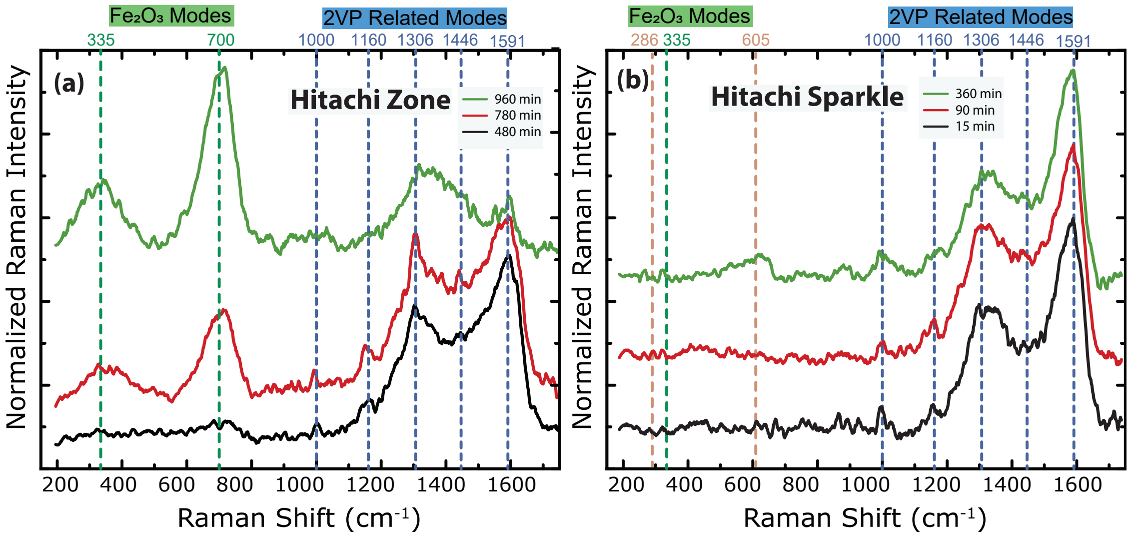

Figure 2.4: Raman spectra of Fe/PS-b-P2VP micelle films after treatment using the (a) Hitachi Zone and (b) Hitachi Sparkle stacked with respect to time.

Chapter 3

Visualizing the template and the particles

3.1 Publication: Utility of far-field effects from tip-assisted Raman spectroscopy for the detection of a monolayer of diblock copolymer reverse micelles for nanolithography

Declaration

Utility of far-field effects from tip-assisted Raman spectroscopy for the detection of a monolayer of diblock copolymer reverse micelles for nanolithography (Phys. Chem. Chem. Phys., 2021,23, 11065-11074)

Authors: Ramis Arbi, Lok Shu Hui, Maria Dittrich and Ayse Turak

This manuscript has been published in **RSC Physical Chemistry Chemical Physics** on **27th April 2021** on the cited page numbers and is available at the following link

https://doi.org/10.1039/D1CP01399H

3.1.1 Introduction

Nanoparticle decoration of surfaces with uniform size and ordered dispersions have been of considerable interest for applications where surface wettabillity [64, 65], overlayer adhesion [66], catalysis [67] or work function modification [30] are desirable. Nanostructures also find widespread use for applications that exploit nanoscale properties that differ from their typical bulk counterparts. With the rise of interest in applications for various nanoparticles, self-assembly techniques using templating methods have become increasingly attractive due to their potential for inexpensive and vsersatile fabrication. [1] However, challenges remains in the ability to characterize small volumes of material, which is often critical in understanding and, consequentially, exploiting nanoparticle properties. Self-assembly of nanoparticles using templating relies on molecules such as diblock copolymers [12, 43, 68, 69], nanotubes [70] and organic ligands [71, 72]. Interactions, between the 'binding' sites on the organic molecule and the nanoparticle precursor determine the nanoparticle dispersion defined by the dispersion of the template. The ability to detect the template is as significant as detecting the nanoparticles themselves. To that end, multiple techniques can be employed to probe nanoparticle and template shape, size and molecular composition.

A particularly versatile and useful technique is Raman spectroscopy, which relies on inelastic light-matter scattering events. It can provide detailed information of the material based on the vibrational modes of the phonons. The Raman spectra originates from the Stokes and anti-Stokes components in the dipole moment, from which the polarizibility can be expanded as a linear function of oscillation frequency [73]. As an incident photon interacts with a molecule, it induces a dipole moment P to the electron cloud. The Raman spectrum results from the frequency shift from the incident frequency (μ_0) of the photon as a result of the vibrational frequency of the molecule (μ_m). It is, therefore, capable of revealing material properties, such as the atomic bonds, vibrational states, purity, crystallinity and strain for a wide variety of materials which is otherwise missing or difficult to achieve in imaging techniques such as electron microscopy, and the methods can be used to complement each other. [74, 75]

Raman spectroscopy has benefits for soft matter and nanostructures over other techniques that provide information about atomic compositions and crystal structures such as energy-dispersive X-ray spectroscopy (EDX) [76], X-ray diffraction [77], electron energy loss spectroscopy [78] and X-ray photoelectron spectroscopy [79], where large sample volume, poor signal to noise ratio, beam damage and charging of non-conductive samples can be an issue. They may often fail to fully differentiate between phases of materials in the nano regime (especially for organic materials), or require large quantities of material or coatings to achieve sufficient conductivity. These are areas where Raman spectroscopy excels. It does not require the presence of a vacuum, conductive samples or dyes to resolve the signal from the sample and is relatively fast, depending on the number of accumulations and the area being scanned. For these reasons, Raman spectroscopy can be used as a fingerprint technique for the identification of nanomaterials and the phase they contain. [43]

Despite all its versatility, Raman often suffers from low scattering cross sections when applied to ultra-thin films and highly reflective materials due to the low inherent sensitivity of Raman scattering [80–82]. For very low volumes, such as monolayers and nanoparticles, the signal from the material of interest can be drowned out in the background scattering. This has lead to the development of and active research on a variety of enhanced Raman techniques to exploit its strengths while mitigating some of its weaknesses.

Tip-enhanced Raman spectroscopy (TERS) has emerged as a particularly useful and powerful technique [83–89]. It employs a fine scanning probe to obtain chemical and morphological information of samples containing structures in the nano-particular regime [90–92], and has demonstrated great success as a non-destructive fingerprinting technique. The TERS signal benefits predominantly from two contributions: near-field effects emerging from the sample area in the proximity of the scanning probe and far-field effects emerging from the illuminated sample area. [93] Some contribution also emerges from the charge transfer effect due to the interaction of the plasmonic metal on the tip and the sample. [94, 95]

The near-field effects arise from the creation and decay of localised surface plasmons (LSPs) and surface plasmon polaritons (SPPs) resulting from the sharp apex of the AFM tip. The plasmonic metal tip in the presence of a ‘perturbing media’ (the sample being characterized) provides a non-radiative decay channel for LSP into SPP in the near field [96]. The scattered light is observable as the enhanced TERS signal. This enhancement is highly dependant on the size and shape of the tip, with different sizes of the apex exhibiting different resonating frequencies, and the proximity of the tip to the surface. [83, 88] Additionally, due to the proximity of the plasmonic surface and the sample, enhancement due to chemical interactions also arise [97–100]. This chemical enhancement depends on the formation of charge transfer complexes between the plasmonic entity and the molecule of interest by absorption of photons of suitable wavelengths. Though this enhancement is useful for identification, the interaction between the plasmonic metal and the sample can sometimes lead to undesirable outcomes including destroying nanostructures on a surface. This is a particular concern for organic molecules with a high affinity for metals. For instance, polymers such as poly-2-vinylpyridine (P2VP) form complexes with plasmonic metals such as Ag or Au, and contact of P2VP structures with plasmonic moieties can lead to the destruction of those structures. [54, 101]

The far-field effects originate from a combination of variables, including laser spot size, laser path, polarization of light, and interference in transparent samples [83]. Typically, these form the TERS background signal as the near-field effects dominate the spectrum when the tip is engaged. To enhance the near-field contributions, care is usually taken to minimize the far-field effects. The ratio of near-field contribution to far-field contribution can be maximized by using light polarized perpendicular to the scanning probe, which confines free electrons on the metal surface at the apex. [102] The far-field and near-field contributions also exhibit different polarization, allowing for a minimum of the far-field effects. Additionally, TERS also benefits from non-linear optical processes such as second-harmonic generation and hyper Raman; however, to reap these benefits specific methodologies and samples need to be used. [83, 103] The interplay of mechanisms can also lead to the relaxation of Raman selection rules, allowing Raman forbidden modes to emerge. [73]

Due to these various mechanisms, the Raman spectrum from TERS are enhanced relative to normal Raman in terms of signal strength by orders of magnitude (10^4) and can exhibit modes which are not allowed under normal Raman scattering conditions [88]. Many of the mechanisms for signal enhancement are also found in other enhanced Raman techniques, such as interference-enhanced Raman (IERS), surface enhanced Raman (SERS), polarized Raman, or Coherent anti-Stokes Raman scattering (CARS), which might also provide better resolution than conventional Raman, though for highly specialized substrates or detector set-ups [53, 54, 80, 81, 83, 104–106] often limiting their use. Due to the nature of its enhancement, TERS has developed into a powerful tool for the characterization of surfaces and structures with a high spatial resolution. However, it is also intrinsically limited to small spatial areas (typically within a range of 20-80 nm from the AFM tip). [90–92, 107]

In this contribution, we describe a technique that benefits from the enhancement provided by employing a fine-tipped probe without the tip being in contact with the surface, taking advantage of the far-field effects. Unconventional Tip-assisted Raman Spectroscopy (uc-TARS) employs a bottom illuminated Raman set-up with a gold coated AFM tip to characterize thinner layers than are possible under typical Raman conditions. In terms of the versatility of applying this Raman approach to a variety of samples, this technique has set-up requirements similar to TERS; however, with the ability to scan larger areas and without the need for vacuum conditions or conductive samples, it represents a desirable approach that can be used to detect small amounts of soft materials. To exploit this technique, we here clarify the relative contributions of various near and far field effects to this unconventional approach, using Raman techniques which share those mechanisms to examine the resultant effects on a model system.

The material used for this investigation was polystyrene-*block*-poly(2 vinyl pyridine) (PS-*b*-P2VP), a diblock copolymer that is widely used in nanomaterial synthesis through reverse micelle templating [12,30,43,108–111]. Due to its chemical structure, it has many Raman accessible vibrational modes [53,54] with a particular sensitivity of the pyridine group to plasmonic metals. [54,112]. Taking advantage of diblock copolymer self-assembly, PS-*b*-P2VP also forms a variety of patterns when deposited from solution that can be easily manipulated, down to spatially distinctive nanostructures in a single monolayer. As such reverse micelles are used as nanoparticle template "nanoreactors" [11,68], it is of practical use to have a non-destructive technique that is able to characterize a single layer of polymer, so as to effectively examine larger surfaces decorated by reverse micelle templated nanoparticles.

Using uc-TARS, it was possible to detect a monolayer of PS-*b*-P2VP micelles and resolve the characteristic modes of the polymer. This spectrum was compared to spectra acquired using analogous samples to determine the mechanisms behind the enhancement achieved from uc-TARS. We have here identified a technique to probe molecular bond information of a monolayer of material that is not limited to a small scan area by exploiting effects beyond the near-field optics governing conventional tip enhanced approaches.

3.1.2 Experimental

Reverse micelles were prepared using polystyrene-*block*-poly(2 vinyl pyridine) (PS-*b*-P2VP, Polymer Source) diblock copolymers of weights Mn: 75000-b-66500; and Mn: 48500-b-70000. The powders were dissolved in o-xylene in concentrations above the critical micellar concentration, typically 3mg/ml. The solutions were magnetically stirred for at least 24 hours before sample preparation.

Raman samples were prepared using drop-casting for thick layers and spin-coating of 4μl of the polymer at 2000 rpm for monolayers. Multilayers were also achieved by spin coating multiple times. Thickness was determined using variable angle spectroscopic ellipsometery (J. A. Woolam IR-VASE M-200). For conventional Raman, the polymer solutions were drop-cast (4μl) on freshly cleaved KBr substrates due to the low background scattering (Supplemental Information Figure SI-1). For inverted set-up measurements (inverted Raman, uc-TARS and polarized Raman), the polymer solutions were spin-coated on a sapphire disk (Ted Pella Inc.). For SERS and IERS, specialized substrates were used for monolayer or multilayer deposition. For SERS substrates, 5nm of Ag was sputtered on a sapphire disk. For IERS, 120 nm of ITO was deposited on gold (Vacuulayer Inc.).

For conventional Raman, SERS and IERS measurements, a Renishaw InVia spectrometer was used. All measurements were top illuminated with 514 nm laser. The laser power was set to 10mW and an objective of 20x (NA=0.40) and 1800l per mm grating was used. For convenience, as the spectrometer is located parallel to the laser perpendicular to the surface being measured, this mode will be referred to as ”normal” Raman. For normal Raman measurements, the laser was focused at regions with visible residue (”coffee stain” area) where there was a larger amount of polymer.

The inverted set-up measurements were used for uc-TARS, polarized Raman, and bottom illuminated (i.e. inverted) Raman, performed on an NT-MDT AFM-Raman spectrometer. All measurements were bottom illuminated with a 514 nm laser. The objective involved was an oil-immersion 20x (NA=0.60) lens. A glass slide was placed on the lens after applying the immersion oil, the sapphire disk was in turn placed on the glass slide, with the polymer facing the lens. A second glass slide was secured on top to allow fastening of the sample.

For polarized measurements using the inverted set-up, the polarization was controlled using a Glenn-Taylor prism in the laser path. For uc-TARS, a gold coated AFM tip was engaged behind the sample so that the tip was not in contact with the polymer, but the glass slide holding the sample.

Figure SI-2 in the supplemental information shows a schematic version of the sample arrangements in each type of measurement.

The baseline of all spectra was subtracted using Origin and the spectra were smoothed using the Savitzky-Golay function. Furthermore, all spectra were normalized against the 1000cm^{-1} peak of PS symmetric ring breathing. Raw intensity values for each technique are summarized in Table SI-1 in the supplemental information.

Atomic force microscopy (AFM) characterization were carried out using an Asylum MFP-3D instrument in the alternating current mode under ambient environment on spin coated reverse micelles on Si wafers. The AFM images were processed by WSxM. [51]

3.1.3 Results and discussion

Figure 3.1 shows how the spectra for a monolayer of micelles collected using uc-TARS compared against the Raman spectra for a thick layer of micelles and bulk PS-*b*-P2VP, normalized to the peak at 1000 cm^{-1}. The peaks marked by dotted lines are a few of the most prominent Raman modes expected for the polymer – 1000 cm^{-1}, corresponding to the symmetric ring breathing of PS; 1454 cm^{-1}, corresponding to either the pyridine ring stretch in P2VP or methylene deformation in PS; and 1613 cm^{-1} corresponding to the pyridine ring stretch in P2VP [43, 53, 54]. PS-*b*-P2VP in different phases does not typically undergo any molecular change and, therefore, the same Raman modes would be expected for the bulk and micellar phases. As expected, Figure 3.1(d) shows no difference between the modes observed for micelles and bulk PS-*b*-P2VP, when they are normalized to the dominant PS mode. Using a Au coated tip behind the sample with bottom illumination, the uc-TARS spectra appears to exhibit modes at the expected wavenumber shifts for a monolayer of micelles; however, the relative intensities of the peaks are not consistent with those observed in the normal Raman spectra, suggesting a selective enhancement. In addition to the unexpected intensity of the peak at 1454 cm^{-1}, two peaks appear to emerge around 1200 cm^{-1} which can be assigned to CH-in plane bend from P2VP expected at 1195 cm^{-1} and CC stretch between the ring and the backbone from PS and P2VP expected at 1206 cm^{-1} and 1217 cm^{-1}. In the normal Raman spectra for the diblock copolymer, the peaks around 1200 cm^{-1} usually appear as just a broad peak around 1217 cm^{-1} for even large amounts of material. The peak observed below 800 cm $^{-1}$ can be assigned to twin peaks of sapphire (the substrate) expected around 750 cm^{-1} as will be discussed later. [113]

Figure 3.1 (a-c) illustrates schematically the differences in the sample arrangement for the collection of each spectra and their respective thicknesses. Typically, due to the low inherent sensitivity of Raman scattering, ultra-thin films and highly reflective materials are difficult to measure due to low scattering cross sections. [80–82] The lowest amount of volume detected by normal Raman depends on a variety of factors such as the material of interest and the substrates chosen. For PS-*b*-P2VP, we determined that the limit of normal Raman was around 120 nm, and detection of a monolayer of micelles is impossible (see supplemental information Figure SI-3). Therefore, the bulk and drop-cast layers have strong visible Raman modes, as they consist of a flake of polymer or multiple dropcast layers, respectively. Typically, drop-casting results in 6 layers of micelles, which are approximately 20-25nm in diameter per micelle. Samples prepared with lesser material were not able to be characterized (Figure SI-3). The success with a thicker layer comes from a greater signal-to-noise ratio resulting from easier focusing of the laser spot on a greater volume of the material of interest and greater signal contrast between the polymer signal and background. For a monolayer ($\sim$20 nm thickness), the signal from the polymer is typically drowned out amongst the background signal in normal Raman. On the other hand, the sample volume for uc-TARS was a monolayer. The enhancement achieved with uc-TARS appears to be on the order of 10^3 (Table SI-1), though a direct intensity comparison is complicated by the use of different Raman systems for measurement. Figure 3.2(a) shows the monolayer of micelles characterized using uc-TARS, where the micelles are arranged in a nearly hexagonally close-packed surface arrangement. The ability to distinguish a signal from a monolayer of polymer from the background using uc-TARS illustrates the benefits offered by this technique; however, to fully utilize its potential, the mechanisms behind the enhancement need to be identified. Additionally, although there is no apparent change in the Raman selection rules using uc-TARS, there is a clear selective enhancement favouring certain modes, as is evident from the different relative ratios of peak heights observed using uc-TARS and normal Raman for the normalized data.

Figure 3.2(b) shows the observed normal Raman spectra of homopolymers of

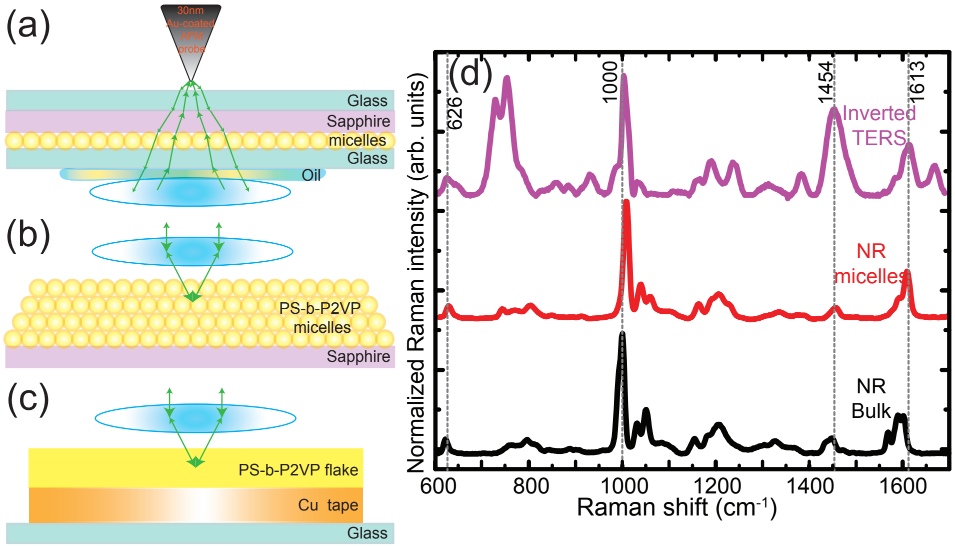

Figure 3.1: Configurations of various Raman set-ups for (a) Inverted TERS of monolayer micelles; (b) Normal Raman of drop-casted thick micelles layers on KBr and (c) Normal Raman of bulk PS-*b*-P2VP flake on Cu tape on glass. (d) Raman spectra of micelles of respective techniques in the schematic, normalized to the mode at 1000 cm^{-1}.

PS, P2VP, and of the block copolymer. The exhibited modes are summarized in Table 1. The inset for Figure 3.2(a) shows the schematic micelle with PS and P2VP blocks indicated. As a result, the Raman spectra of PS-*b*-P2VP diblock copolymer consists of modes emerging from both polymers, as identified in Figure 3.1. As the molecules possess structural similarities, the Raman spectra of PS and P2VP share some common modes at similar waveshifts. For instance, both share the methylene twist modes at 1330 cm^{-1} and 1380 cm^{-1}, and the ring stretch around 1560 cm^{-1}. [53, 54] Moreover, there is a pyridine ring stretch from P2VP and methylene deformation from PS that are coincident around 1450cm^{-1}. Yet there are a few distinct modes of each, due to the ring structure difference between benzene and vinyl pyridine. For instance, the 1000cm^{-1} symmetric ring breathing mode $\nu(1)$ (assigned with the Wilson's numbering system) in PS appears strongly while the 989 cm^{-1} mode for

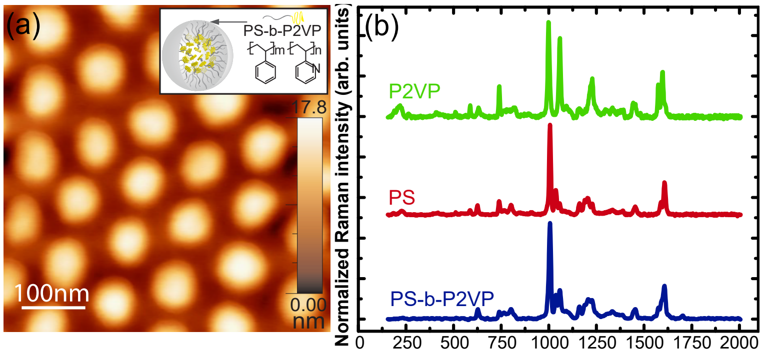

(c) Table 1: Table of expected Raman peaks for PS, HP2VP, PS-b-P2VP

PS, cm^{-1}	HP2VP, cm^{-1}	PS-b-P2VP, cm^{-1}	Assignment
619	625	620	In-plane bend of the ring
739	733	734	
760;798	815	793	CC stretch between ring and backbone
	989		C-H out of plane bend
1000		1000	Symmetric ring breathing
1032;1054;1152;1184	1054;1086;1152	1033;1054;1195	CH in-plane bend
1206;1228	1217	1217	CC stretch between ring and backbone
	1293		
1326	1326	1326	Methylene twist
1380	1380	1380	
	1434	1440	Pyridine ring stretch
1445		1444	Methylene deformation
1576	1565;1586	1567	Pyridine ring stretch
1597		1600	Ring stretch

Figure 3.2: (a) AFM topography of a monolayer PS-*b*-P2VP micelles spin-coated on Si. Inset: schematic of a PS-*b*-P2VP reverse micelle. (b) Offset normalized Raman spectra of PS, P2VP and PS-*b*-P2VP suspended in oxylene and drop-casted on KBr, measured by normal upright Raman.(c) Table of Raman modes observed for PS, P2VP and PS-*b*-P2VP.

C-H out of plane bend is suppressed. [53, 54] Similarly, the CC stretch between ring and backbone mode appears at 1217 cm^{-1} for P2VP, suppressing the PS peaks at 1206 cm^{-1} and 1228 cm^{-1}. Another mode appears at 1600 cm^{-1}, which could be attributed to a shifted P2VP pyridine ring switch. As the micelles exhibit a mixture of these modes, the individual peaks can be used as the fingerprint for the copolymer blocks. The $\nu(1)$ mode at 1000 cm^{-1} for PS is the strongest mode, so it is in general used as the characteristic peak for the identification of the polymer. Due to this ability to distinguish between different components and their distinct modes, PS-*b*-P2VP served as an ideal template to examine the effective enhancement obtained via different Raman techniques.

The wide variety of possible mechanisms that could contribute to the enhancement observed with uc-TARS are illustrated in Fig 3.3(b-f); namely, surface plasmon resonance, interference-based enhancement, increased laser path, polarization based enhancement and higher order optical effects. Each mechanism was chosen by considering different phenomena possibly occurring at each step of the experiment. Comparisons are made with techniques that share these mechanisms to understand the enhancement offered by uc-TARS by discussing the Raman peaks acquired for PS-*b*-P2VP micelles using each technique. Figure 3.3(a) illustrate the spectra acquired using the corresponding techniques which use the mechanisms proposed to contribute to uc-TARS. All spectra are normalized against the 1000cm $^{-1}$ peak of PS to eliminate any effects due to differences resulting from the Raman system utilized. Moreover, for each technique, the thickness of the smallest film that could be characterized using the respective technique is indicated to illustrate the required interaction volume for each.

Though the tip is not in proximity to the micelle monolayer, thereby negating any near-field interactions, we consider the plasmonic enhancement effect as shown in Figure 3.3(b) of the gold plasmonic moiety on the AFM tip as this is the typical enhancement mechanism for tip-enhanced approaches. Surface-enhanced Raman spectroscopy similarly benefits from enhancement arising from a thin layer of a plasmonic metal on the substrate [82, 114], so SERS can be compared to uc-TARS to determine the role of plasmonic resonance on the spectra. Typically, two mechanisms can contribute to the enhancement observed in SERS: the localized SPR of the plasmonic species on the substrate, and charge transfer effects due to adsorption of the

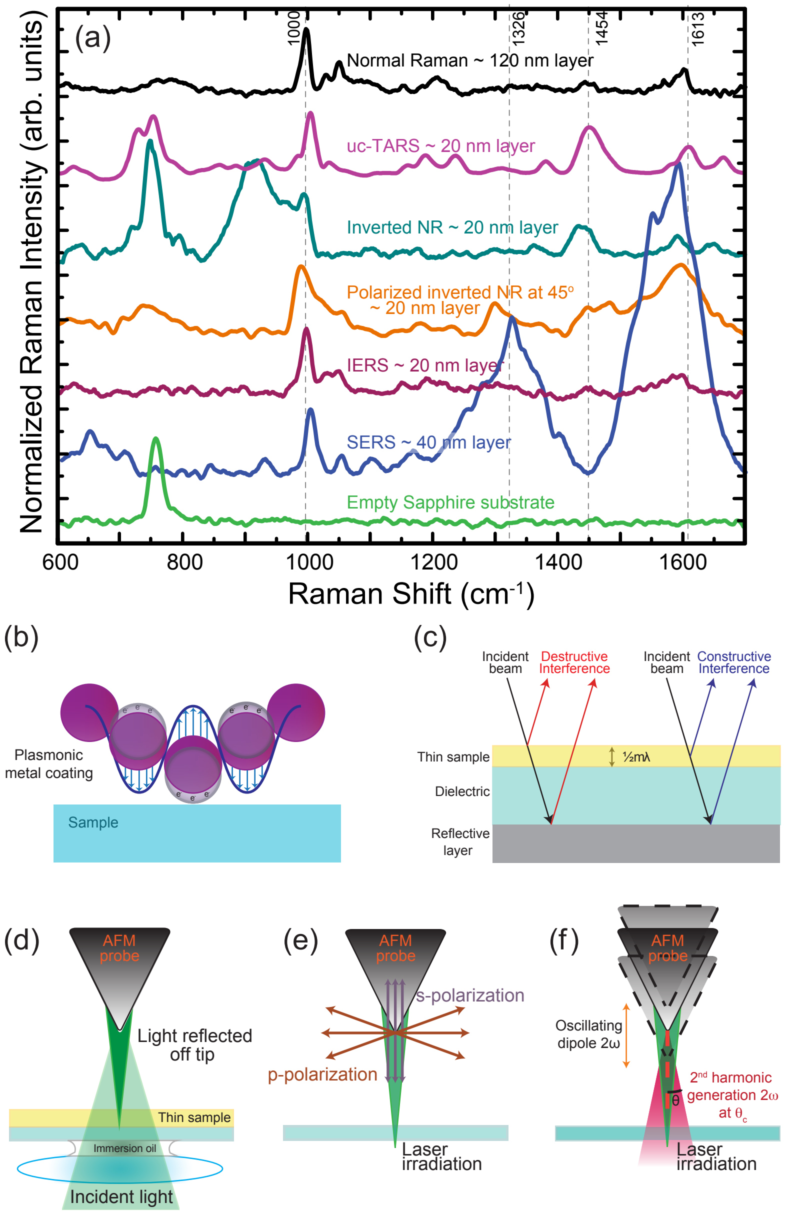

Figure 3.3: Possible Raman enhancing mechanisms of TERS. (a) Raman spectra of micelles by normal Raman (black), uc-TARS (purple), Inverted Normal Raman (green), polarized Raman (orange), IERS (maroon), and normal Raman of the empty Sapphire substrate (light green), normalized to the mode at 1000 cm^{-1}. (b) Enhancement of localized electric field due to surface plasmon generation from metal tip coating. (c) Interference-enhanced Raman scattering due to the reflective back coating of sample substrate. (d) Far-field focusing enhancement due to tip. (e) Depolarization of laser due to the tip. (f) 2nd harmonic generation effect or hyper Raman effect.

molecule onto the plasmonic film. [101, 115] The former results from the electromagnetic theory of SERS while the latter is a chemical enhancement, and de-convoluting the effect of each is a topic of active research. [116, 117]

The SERS spectra in Figure 3.3(a) contains the characteristic peaks at 1000 cm^{-1} and other expected Raman modes. SERS still required at least two layers to fully resolve the polymer peaks, with a thickness of 40 nm (see Figure SI-2(b) and Table 3.2). However, as this was achieved from substantially less polymeric material compared to normal Raman, the visibility of the characteristic peak at 1000 cm^{-1} shows the volume enhancement effect from the plasmonic Ag film as has been observed previously for these block co-polymer systems [53, 54]. Moreover, certain modes are favourably enhanced in SERS on Ag, for example, the peaks at 1324 cm^{-1} and 1585 cm^{-1} which evolve from the P2VP modes of $\gamma(\mathrm{CH_2})$, the methylene twisting mode and $\nu(13)$, the C-C stretching mode between the pyridine ring and the backbone. These modes are characteristic of complexation of the polymer and the plasmonic metal. [43, 53] Enhancement of the pyridine stretching modes are observed in both uc-TARS and SERS; however, SERS shows different relative intensities, which can be summarized in terms of enhancement factors displayed in Table 3.2. There is a clear enhancement of the complexation related modes at 1324 and 1585 cm^{-1} compared to normal Raman, but no significant enhancement of the mode at 1454 cm^{-1} or the features around 1200-1300 cm^{-1}. The SERS modes also appear to be shifted to lower wavenumbers, which is attributed to the adsorption of the 2VP block on Ag. [73, 101] This chemical interaction causes the diblock copolymer micelles to unravel, leading to an increase in intensity of pyridine related modes [54]. Hong et al [54] previously attributed the emergence of such peaks to micellar destruction due to the strong interaction between pyridine and Ag. Figure SI-4 in the supplemental shows the spectra of P2VP complexated with a Au salt, showing the characteristic peaks at 1324 and 1585 cm^{-1}. Though this is useful in confirming the presence of 2VP moeities, it actually limits the use of SERS for reverse micelle systems used for nanoparticle templating, as it is no longer a non-destructive approach. As seen in Figure SI-2 (f), the presence of a glass slide and the sapphire substrate between the AFM tip and the polymer micelles limit the interaction of the tip with the target molecule, ruling out a chemical interaction based enhancement for uc-TARS. As a result, the enhancement of the modes at 1613 cm^{-1} is relatively modest (∼1.37x), much closer to the ratios reflected by normal Raman than SERS(∼10.6x), confirming that uc-TARS is not benefitting from the selective enhancement offered by the presence of a plasmonic metal as in SERS. Moreover, the ring stretching mode at 1454 cm^{-1} is enhanced ∼5.12x versus 0.5x for SERS. The visible modes at 1250 cm^{-1} in uc-TARS cannot be accounted for by SPR, as they are not present in SERS.

Due to the sample geometry, with a highly reflective tip situated behind a dielectric film (in this case sapphire), another possible mechanism for enhancement arises due to interference as shown in Figure 3.3(c). Interference-enhanced Raman spectroscopy requires a smooth reflective back coating covered with a transparent dielectric of controlled thickness to offer an enhancement of up to 30 times [106]. The dielectric thickness is critical for the incident and scattered light to exhibit self-interference. Theoretically, the combined thickness of the dielectric substrate should be around $\frac{(2m+1)\lambda}{4}$. [106] The thickness of the dielectric layer will result in π-phase shifts as the incident ray is reflected from the bottom with higher refractive index. Destructive

Table 3.2: Table of relative enhancements obtained from the spectra for each technique, including the P2VP ring stretch at 1613 cm^{-1}, and methylene deformation at 1454 cm^{-1} with the PS ring breathing at 1000 cm^{-1}

Technique	Pyridine ring stretch/ PS ring breathing	Enhancement vs NR	Methylene Deformation/ PS ring breathing	Enhancement vs NR	Thickness of polymer film (nm)	Enhancement at PS ring breathing
uc-TARS	0.49	1.37	0.78	5.12	20	3000
SERS	3.78	10.6	0.07	0.48	40	10
Inverted Raman	0.42	1.18	0.48	3.16	20	260
IERS	0.34	0.96	0.16	1.05	20	14
Inverted Raman @60	1.88	5.28	0.83	5.48	20	130
Inverted Raman @45	1.34	3.74	0.57	3.69	20	70
Normal Raman	0.36	1	0.15	1	120	1

interference occurs on the reflected component of the incident ray while constructive interference occurs for the scattered ray. For a 514nm excitation laser, the thickness for IERS would be 125 nm. [104, 105] The total modification factor (F(d,λ_1, λ_2)) of IERS is the combination of the modification (f_1(d,λ_1)) due to the self-interference of the incident light (λ_1) and modification (f_2(d,λ_2)) from the self-interference of scattered and emitted light (λ_2). [106]

The spectra for IERS is shown in Figure 3.3(a), where the characteristic 1000 cm^{-1} is prominent and the other expected modes between 1200 and 1600 are observed. As shown in the supporting information Figure SI-2(d), IERS signals result from the arrangement of a monolayer of micelles on specially grown ITO films on gold. As this was detected using the normal Raman system, enhancement from interference effects are significant, allowing characterization of material well below the normal Raman detection limit (∼20nm vs 120nm). The spectrum is directly comparable to the normal Raman spectra observed for thick layers of the polymer. As IERS is a purely optical effect, all modes are enhanced equally. Therefore, the IERS results in enhancement in terms of the volume as seen in Table 3.2 but has no selectivity of modes. It is possible that the interference has some effect on uc-TARS spectra; however, the thickness of the glass slide used in uc-TARS was larger than the 125 nm required for IERS. Therefore, even though the requirement for a highly reflective back layer was fulfilled, constructive interference should not be observed, and it is likely only making a small contribution.

Another aspect of uc-TARS that could lead to enhancement in the resulting spectra is an increased laser path length due to the instrumental configuration. uc-TARS was carried out with bottom illumination so an inverted microscope with an oil-immersion objective was used as seen schematically in Figure 3.3(d). As the the glass slide carrying the sample was in contact with the oil, a higher numerical aperture could be used, allowing for better focus of the Raman laser on the sample. [88] Additionally, compared to normal Raman, the laser path is doubled in the inverted set-up. This would be exaggerated even further with the tip engaged, through reflection off the tip surface (see supplemental Figure SI-2 (f)) . Any effects emerging due to far field focusing or path length increases would also be visible in the inverted Raman without the tip engaged. To examine such effects, inverted Raman spectroscopy without the tip was performed on a monolayer of polymer micelles.

As seen in Figure 3.3 (a), the spectrum for inverted Raman resembles the spectra for thick layers of PS-*b*-P2VP under upright normal Raman. The characteristic 1000 cm^{-1} is present with expected peaks visible in the 1300 cm^{-1}- 1500 cm^{-1} region. The intensity ratio exhibited by 1454 cm^{-1} and the 1613 cm^{-1} the inverted normal Raman is spectra are similar to the uc-TARS spectra (see Table 3.2), but differ from that observed in normal Raman for thick micelles. However, the peaks at around 1200 cm^{-1} are absent from the spectra, and an intense peak at 900 cm^{-1}, most likely from the immersion oil, appears.

Interestingly, the spectra acquired from the inverted Raman had a very low signal-to-noise ratio compared to normal Raman, and was able to resolve a peak below 800 cm^{-1}, attributed to sapphire. Comparing supplemental Figure SI-2 (e) and (f), we can see that the laser path is significantly smaller in inverted Raman compared to uc-TARS. The AFM tip also enables a sharper focus of light while reflecting off it on to the material of interest, acting similar to a parabolic mirror. [118] As such, in inverted Raman, a noisier spectra is observed with only a single peak of sapphire at 750 cm^{-1}. uc-TARS, on the other hand, likely benefitting from far field focussing and path length increase was capable of resolving twin peaks of sapphire (724 cm^{-1} and 750 cm^{-1}) [113]. The inverted Raman of the empty Sapphire disk exhibits the peak around 750cm^{-1} as can be seen in Figure 3.3 (a).

The improved optics of the set-up and the increased path length from inverted Raman do lead to enhancement of the spectrum, resolving the characteristic strong peaks of a monolayer of the diblock copolymer, and the fine features of the substrate, confirming its role in the observed uc-TARS signal.

Typically, the polarization of light has an effect in tip enhanced spectroscopy, as far-field effects are dependent on the LSPR induced modulation of light due to the plasmonic metal coating the tip, with the greater LSPR effect on polarization in the axis of the plasmonic structure. [83] This amplifies the intensity of certain polarizations of light in the axis of the tip over others, thereby effectively partially polarizing the light reflected off the tip. This has been determined to be highly dependant on the LSPR response of the plasmonic structure which is in turn dependant on the geometry of the structure, and for rod like structures (for example, the tip) it is greater along the longer axis. [119]. Additionally, anisotropic thin films of gold polarize incident light [120] and therefore, it may be possible that the gold on the AFM tip contributes to the polarization of the reflected light off the tip. Typically, as near-field effects are desirable in TERS, it comes down to the competition between the LSPR generated and the gap between the material and the tip (typically ¿20 nm) and the far-field polarization effects from the interaction of the incident light and the LSPR. The former forms the basis of the TERS signal and the latter is treated as the background noise. However, since the the near-field effects have been avoided in uc-TARS, this far-field effect could be considered a mechanism of the increase in signal for uc-TARS of modes that are aligned with the intensified polarization of light. This polarization of light off the tip can be emulated and tested by polarizing the incident light in inverted Raman at different angles using a Glenn-Taylor prism, to assess the role of polarization of light in the uc-TARS spectra.

To determine the role of the polarization of incident light off the AFM tip (as seen in Figure 3.3 (e)) in the uc-TARS spectra, the polarizer on the inverted Raman spectrometer was adjusted to different angles with the tip withdrawn (shown schematically in supplemental Figure SI-2 (c)). The spectra acquired using 45° light is presented in Figure 3.3 (a) as this showed selectivity for P2VP with visible PS peaks. Since the polarized Raman was essentially inverted Raman with a polarizer, the differences arising between the spectra from the two techniques can be attributed to polarization effects.

In the polarized Raman spectra, the characteristic peaks are visible with a favourable enhancement towards 2VP peaks. The mode at 1454 cm^{-1}, due to methylene deformation, 1613 cm^{-1}, due to the ring stretching mode of P2VP and the methylene twist modes around 1300 cm^{-1} are all enhanced relative to normal Raman. Intensity of ring stretch Raman modes of PVP have been observed, in literature, to fluctuate with respect to polarization and the alignment of the nematic phase (parallel alignment of molecules) when arranged in a liquid crystal. [121] Clearly, the P2VP modes benefit from polarizations at angles where PS peaks are less selected.

This selective enhancement was further investigated over a range of polarizations. Figure 3.4 summarizes the effect on the 1000 cm^{-1} peak, which is the strongest peak observed for PS. The spectra were normalized by the P2VP modes observed around 1600 cm^{-1} emerging from the ring stretch. Without any polarization (inverted Raman), at 0° polarization (Figure 3.3 (a)), the signal from PS is the strongest, with $\sim$2.8x greater intensity than the P2VP ring stretch mode. As the light is polarized, the peak at 1000 cm^{-1} decreases in intensity relative to the P2VP mode, and eventually disappears after 135° polarized light. At this same polarization, the 2VP peaks around 1600cm^{-1} exhibit their strongest intensity, $\sim$ 15x greater than that observed at 0°. Moreover, the 1000 cm^{-1} also appears to be shifted to lower wavenumbers with increasing polarization, approaching the expected mode for P2VP due to the C-H out of plane bend at around 990cm^{-1}. [53] This is further evidence of P2VP modes being favoured, as typically these P2VP peaks are not visible in the diblock copolymer, which is dominated by the PS signal. The broadening of the 1000 cm^{-1} peak also suggests enhancement of P2VP modes over PS modes, since the P2VP peaks emerges around 990 cm^{-1}, but is not typically visible under normal Raman compared to the PS peak. Unlike in SERS, there is no possibility that this broadening can result from micelle unraveling.

The ratio of P2VP modes and PS modes that is closest to that observed by uc-TARS is observed for 45° polarization for the ring stretching mode (1613 cm^{-1}) and at 60° for the methylene deformation (1454 cm^{-1}). However, no polarization angle measured was able to fully match the peaks observed in uc-TARS. Polarization also seems to selectively select against the sapphire modes, as they are significantly lower in the polarized Raman spectra compared to those observed in inverted Raman.

Conventionally, polarization is often neglected in conventional TERS, as it does not contribute to the signal emerging from the near-field effects [96], rather forming the background signal. In uc-TARS, however, without the effect of the near field LSPR-enhancement, the polarization of light off the AFM tip can be observed as an enhancement mechanism, mildly favouring the P2VP associated Raman modes. Though the polarization can provide an explanation for the selectivity emerging from uc-TARS for P2VP modes, the polarized Raman does not show the same relative peak intensities as uc-TARS, for any one polarization angle, as is observed in Table 3.2. This could result from the fact that the light polarized by the polarizer was 100% and the light polarized off the AFM tip would be much less.

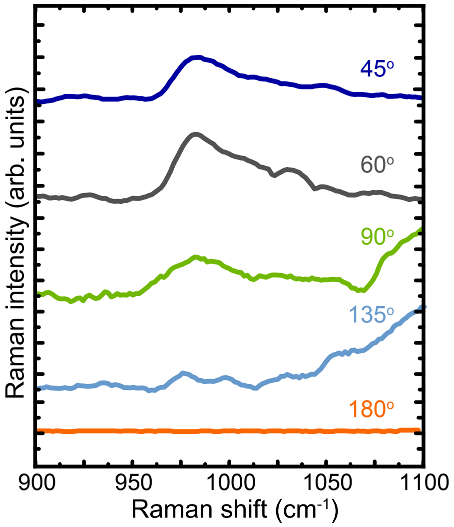

Figure 3.4: Inverted Raman of a monolayer of PS-*b*-P2VP reverse micelles under different polarization conditions, focused on the peak at 1000 cm^{-1} typically associated with the PS component of the diblock copolymer.

Figure 3.3(f) shows the 2nd harmonic generation and the hyper Raman effect due to the strong electric field at the sample. These effects emerge from the oscillation of the tip, which leads to the changes in electric field, giving rise to a polarizability gradient [83, 103]. The hyper Raman effect is difficult to isolate, typically emerging from the sample conditions [103]; however, due to the polarizability gradient, it can lead to a relaxation of the Raman selection rules, with non-active Raman modes expected to appear due to non-linear scattering. Since no such artifacts can be identified in the uc-TARS, hyper Raman and other higher order optical effects are unlikely as possible mechanisms for uc-TARS. Additionally, the presence of the glass slide and sapphire disk (as seen in Figure SI-2 (f)) between the polymer and the AFM tip should prevent any hyper Raman effect resulting from the electric field between the tip and the polymer.

Table 3.2 summarizes the enhancements observed in the various techniques in terms of the volume required to achieve a Raman spectrum, the intensity enhancement of the PS ring breathing mode observed at 1000 cm^{-1}, the ratio of the PS ring breathing mode and the P2VP ring stretching mode observed at 1613 cm^{-1}, and the ratio with the 1454 cm^{-1} pyridine ring stretch mode, with respect to the ratios obtained from a normal Raman spectrum of a thick sample of PS-b-P2VP micelles. All of the methods require much less volume of material to observe a Raman spectrum from the diblock copolymer micelles, with IERS, inverted Raman, polarized Raman and uc-TARS all able to show significant features from a monolayer. Every technique resulted in almost an order of magnitude increase in the signal intensity at the PS ring breathing mode, when corrected for the sample thickness. IERS did not shown any of the enhanced selectivity for P2VP modes that was observed in uc-TARS. SERS did display significant enhancement of P2VP peaks over PS peaks, with only a relatively modest enhancement of the PS mode; however, this was a result of the chemical interaction of the micelles with the Ag surface, resulting in complexation and unraveling of the micelles. Polarization does offer enhanced selectivity of the P2VP modes, including the ones observed in uc-TARS. However, the ratio of peak intensities could not be matched to that observed in uc-TARS for a fixed polarization angle. The closest selectivity and signal enhancement to that observed for uc-TARS for the 1454 cm^{-1} modes was observed for inverted Raman; however, the substrate and immersion oil peaks were enhanced much greater than the polymer peaks, limiting its use for practical measurements.

In light of all the techniques investigated, the uc-TARS spectra can be described in terms of enhancement stemming from increased laser path, improved far-field focus due to the tip, and the depolarization of the light off the AFM tip. The role of the increased laser path and the additional tightening of the focus due to the incorporation of an AFM tip explains the resolution of the sapphire twin peaks below 800 cm^{-1}, and the enhancement of the characteristic polymer peaks at 1000 cm^{-1} and between 1300 cm^{-1} and 1500 cm^{-1}. The role of polarization is more subtle but can be an explanation of the selectivity of uc-TARS for certain P2VP modes, specifically 1454 cm^{-1} and 1613 cm^{-1}, and the splitting of the broad peak around 1217 cm^{-1} into two individual peaks for PS and P2VP. However, the existence of the strong PS peak at 1000 cm^{-1} in the uc-TARS spectra indicates that the polarization is not at the optimal angle for maximum enhancement of the P2VP peaks. It appears that the increased laser path and far field effects are the dominant mechanism of enhancement, with benefits for selective enhancement from polarization.

3.1.4 Conclusion

We have demonstrated a modified Raman technique incorporating an AFM tip that provides significant signal enhancement, without requiring near field enhancement that the inclusion of an AFM probe typically provides. Instead, an interplay of mechanisms allowed for enhancement of signal from very small volumes of materials over large areas of interest. By using PS-*b*-P2VP micelles and comparing the spectra acquired to that from other enhanced Raman techniques, a better understanding was developed of the mechanisms likely contributing to this unconventional tip assisted Raman spectroscopy (uc-TARS). uc-TARS benefits from an increased laser path, improved far-field focusing due to the tip, with contributions from polarization off the gold coated AFM tip. Therefore, we have here identified a technique to probe molecular bond information of a monolayer of material that is not limited to a small scan area by going beyond the near-field optics governing conventional TERS. This opens up avenues of interest in non-destructive characterization mapping of nanaostructures on a surface and opportunities for in-situ characterizations.

Supporting Information

Supporting Information is available from Royal Society of Chemistry online or from the author. This hyperlink will take you to the Supporting Information

3.2 Resonance enhanced Raman modes of polymer due to proximity of certain precursor salts

3.2.1 Introduction

Pyridine, with nitrogen replacing a methine group =CH− in the benzene ring, has garnered interest on account of its structure and properties. As the nitrogen lone pair is not delocalized with the aromatic bonds, pyridine is basic and can donate the lone pair to Lewis acids to form adducts [122–126]. As a result, pyridine acts as a monodentate ligand for a variety of transition metal ions and also, the lone pair exerts an indirect influence on the environment of the benzene-like ring [122]. This has lead to the use of bipyridine, terpyridine and other poly-pyridine systems as multidentate ligands for various molecular complexes.

Pyridine and its polymeric forms are insoluble in some organic solvents such as toluene or xylenes; coupling them with soluble polymers can allow for their use in templating of nanostructures by providing active sites for trapping metal salts [6,8,11, 43,127]. This is particularly useful in the case of pyridine-based copolymers, such as poly(styrene)-b-poly(2-vinyl pyridine), which form varying self-assembled structures (lamillae, planar or micellar) depending on the solvent, concentration and molecular weight of the blocks [6,7,128–130]. The uniformity of the polymer self-assembly can be tuned making PS-b-P2VP an important polymer in the field of diblock copolymer lithography and self-assembled monolayers [8,20,131]. One of the most useful PS-b-P2VP phases is spherical reverse micelles formed in non-polar solvents, with the hydrophobic poly(styrene) chains on the outside forming the protective corona and the hydrophilic poly(2-vinyl pyridine) forming the core. In this manner, the spherical micelles can be used as nanoreactors to make ordered nanoparticle dispersions of controllable size and phases by segregating the precursor salts in to the cores of the micelles. These micelle cores can also be utilized as nanobeakers for localized multi-salt reactions [34]. It has been used for the synthesis of nanostructures of metals, metal oxides, dielectrics and perovskites for applications as diverse as photovoltaics, catalysis, chemical or optical sensing, energy storage, or photonics. [8, 12, 17, 19, 32, 34–36, 43, 108, 132–141]. In addition to the polymer, solvent and precursors, the surface energy of the substrate and deposition method of choice also affect the size and periodicity of the self-assembled structures. [16, 142, 143] All the variables come together to allow tailor-made monolayers of different materials.

To produce specific designer nanomaterials for target applications, it is necessary to have an understanding of all the mechanisms involved in nanoparticle synthesis. The first step towards establishing an understanding is to have an ability to characterize the particles and the polymer reliably at every stage of the synthesis process.

To that end, there are a plethora of techniques in the toolbox, ranging from vibrational spectroscopy to electron spectroscopy and force microscopy to electron microscopy. A key method is Raman spectroscopy, which probes the structural information, phase and molecular interactions of a material through inelastic light scattering off chemical bonds. It can be used to identify fingerprint patterns for identification of Raman-visible metal oxides and polymers, and can be used to resolve small quantities of material down to monolayers [17, 43, 44]. For the case of PS-b-P2VP and $FeCl_3$, changes in the Raman and FTIR spectra of neat polymer after Fe-salt introduction have been reported, indicating ligation of the salt with polymer and hence 'loading' of the salt into the micelle [17, 43, 144]. These vibrational peaks can, therefore, be used as a screening tool to confirm the interaction of salt and polymer, and the segregation of the salt inside the micellar structure.

In order to use Raman to confirm the successful loading of polymer, we must understand the mechanism behind the changing spectral features. Vibrational modes of the polymer can be influenced by either structural changes in the polymer due to the interaction with the metal salt [145–147] or by charge transfer between the metal and polymer [148–150]. To distinguish between the two, it is important to correlate potential complexes that can be formed formed and the resultant expected changes in the vibrational spectra, using ligand field theory as a basis to determine the number of metal-ligand interactions.

Depending on the coordination geometry of the ligand and the transition metal, the splitting of the d-orbital of the metal can take different forms due to the overlap of ligand and metal orbitals. For instance, in an octahedrally coordinated sphere, $d_{x^2y^2}$ and d_{z^2} orbitals (e_g) are raised in energy while the remaining 3 d orbitals (T_{2g}) are slightly lowered, while in a tetrahedrally coordinated sphere the opposite holds true. The decrease in energy of the electronic configuration in the ligand field is commonly known as the crystal field stabilization energy (CFSE) and is generally higher for octahedral complexes of most transition metals, making them more stable. CFSE is dependant on the coordination geometry, number of d-electrons in the transition metal, and the strength of the ligand [151, 152]. The spectrochemical series lists ligands based on their strength as follows [151,152]:

$$\mathrm{I^-} < \mathrm{Br^-} < \mathrm{Cl^-} < \mathrm{OH^-} < \text{pyridine} < \text{bipyridine} < \mathrm{CN^-}$$

The magnitude of the d-band splitting is also dependent on the strength of the ligand, with higher splitting observed for stronger ligating species [151, 152].

Pyridine is an intermediate level ligand being a strong σ-donor thanks to its nitrogen lone pair and a π-acceptor with its delocalized $\pi*$-orbital. Stronger-field ligands would lead to a greater splitting of the d-orbitals and result in low-spin complexes with paired electrons preferentially occupying the lower energy states. Pyridine-based polymers like Poly(2-vinyl pyridine) act as polydentate ligands and exhibit strong binding strength to metal salts when compared to monodentate or bidentate ligands. The postions of donor atoms in a polydentate ligand (macrocycle) are fixed, allowing less conformational freedom, this reduces entropic effects on its binding energy, thereby making the complex more stable. [153, 154] This is referred to as the macrocyclic chelation effect [153,154] and is the reason behind preferential ligation between metal and pyridine-based polymers, in the presence of metal halide salts. In the case of PS-b-P2VP diblock copolymer and halide based salts, this is most likely a critical mechanism for encouraging infiltration into the micelle.

The changes observed in the vibrational spectra for complex ligand formation appear to selectively enhance some polymer modes over others, in an effect reminiscent of enhanced Raman methods such as surface or tip enhanced Raman spectroscopy (SERS/TERS) [44]. SERS, in particular, emerges as an interplay of two main mechanisms: electromagnetic enhancement due to plasmonic resonance and chemical enhancement due to the formation of charge transfer bands [44, 148, 155, 156]. This second resonance based enhancement is considered the main mechanism of enhancement emerging from metal oxides or semiconducting surfaces [148,149,155,156], where plasmonic effects are not present. Charge-transfer occurs between the surface and the overlayer due to vibronic coupling of the electronic structures. These so-called

Herzberg-Teller contributions to SERS display enhancement of vibrational modes emerging from surface charge transfer while conserving the normal Raman selection rules [148, 149, 155, 157].

In resonance Raman spectroscopy, the excitation wavelength falls within the electronic absorption band of the material being probed. This is in contrast with normal raman where the excitation wavelength is out of the region of absorbance of the material. This results in the excitation of only localized vibrations within the absorbing group as the excitation wavelength approaches the absorbance band. This results in a selective enhancement of only some groups related to the absorbing material. [73, 112, 158, 159] Resonance raman can be employed for organic coordination compounds of transition metals, where enhancement is observed from mixing of excited state of the material (e) with an intermediate state (s), given that the two states are closely located. This can be summarized in terms of charge-transfer effects (Herzberg-Teller contributions). [148, 149, 155, 157, 159]. This also allows for the appearance of overtones and combination bands under resonance conditions which typically cannot be seen. [159]

In this study, we examine the typical shape of 'loaded' PS-b-P2VP micelles measured with Raman spectroscopy in terms of possible mechanisms, and possible resultant complexes to explain why it is observable for some metal salts such as Fe and not others such as Zn. The mixing of states and allowed metal-ligand and ligand-metal charge transfer bands appears to lead to a resonance-based enhancement of P2VP modes in proximity to precursor metal salt. The availability of charge transfer bands close to the excitation wavelength seems to play a significant role, and can be used as a route to examine other salts as potential precursors for reverse micelle templating.

3.2.2 Experimental Methods

Reverse micelles were prepared using polystyrene-*block*-poly(2 vinyl pyridine) (PS-*b*-P2VP, Polymer Source) diblock copolymers of weights Mn: 75000-b-66500. The polymer was dissolved in o-xylene in concentrations of 3mg/ml. The solutions were magnetically stirred for at least 24 hours before sample preparation.

Precursor salts were added to prepared polymer solutions in amounts calculated with respect to 2VP units. Loading ratios of 1:1 (M:2VP) were used unless indicated otherwise. $HAuCl_4 \cdot 3\,H_2O$ ($\approx$ 99.9 %), $AlCl_3$ (anhydrous, $\approx$ 99.99 %), $FeCl_3$ (anhydrous, $\approx$ 99.99 %), $ZnCl_2$ (anhydrous, $\approx$ 99.995 %), and $CuCl_2$ (anhydrous, $\approx$ 99.995 %) were acquired from Sigma Aldrich and all handling of precursors was performed under N_2 environment inside a glovebox.

For polymer removal, the deposited films were exposed to O_2 plasma (29.6W, 950mTorr, Harrick PlasmaCleaner) for 45 min.

Raman samples were prepared using drop-casting of 4μl of the solution for thick layers on freshly-cleaved KBr crystals and spin-coating of 4μl of the solution at 2000 rpm on aluminum foil for monolayers. Multilayers were achieved by spin coating multiple times. A Renishaw InVia spectrometer was used for all measurements equipped with a 514 nm laser. The laser power was set to 10mW and an objective of 20x (NA=0.40) and 1800l per mm grating was used. The baseline of all spectra was subtracted using Origin and the spectra were smoothed using the Savitzky-Golay function. For fitting, Lorentzian lineshape profiles were used on baseline subtracted data between 900 cm^{-1} and 1750 cm^{-1}. Polarized Raman was performed using an NT-MDT AFM-Raman spectrometer. All measurements were bottom illuminated with a 514 nm laser. The objective involved was an oil-immersion 20x (NA=0.60) lens. A glass slide was placed on the lens after applying the immersion oil, the sapphire disk was in turn placed on the glass slide, with the polymer facing the lens. A second glass slide was secured on top to allow fastening of the sample. The polarization was controlled using a Glenn-Taylor prism in the laser path.

Fourier Transform Infrared Spectrum were acquired using Attenuated Total Reflectance (ATR) on a Bruker vertex 70 using the standard mid-IR laser by drop-casting the solution on the diamond-ATR crystal. The output spectra was subtracted against the background spectra acquired without the sample.

Raman spectra were simulated using Wiley Know-it-all [160] for idealized molecular fragments.

Atomic force microscopy (AFM) characterization were carried out using an Asylum MFP-3D instrument in the alternating current mode under ambient environment on spin coated reverse micelles on Si wafers. The AFM images were processed by WSxM. [51]

3.2.3 Results and Discussion

Previously, we have reported on the enhancement of polymer modes observed with Fe-loaded PS-b-P2VP as a method of monitoring the successful loading of polymer and as a tracking mechanism for polymer removal and growth of nanoparticles. [17,43,161] Using Raman spectroscopy, we have been able to track the entire synthesis process from neat polymer to fully formed nanoparticles [17, 43]. Using this knowledge, we have successfully tailored the synthesis process to produce iron nanoparticles of different phases (hematite, maghemite and magnetite) and dispersion [17, 42, 43].

Specific 2VP ring modes in FTIR spectroscopy have also been reported in literature to suggest the coordination of $FeCl_3$ with the nitrogen on 2VP, where the free pyridine ring is expected to red-shift from 1590 to 1619 cm^{-1} upon coordination, with a pyridine mode around 1570 cm^{-1} which remains unchanged [144]. Figure 3.5 (a) show the results from FTIR of drop-casted samples of neat and loaded polymer which conform exactly to the expected shift reported by Sageshima et al [144]. The same materials under Raman show significant enhancement in a region between 950 and 1750 cm^{-1}, where the major peaks of the PS and the P2VP block appear as listed in Table 3.3, suggesting that these features are also related to the formation of a complex between the 2VP and $FeCl_3$, as in Figure 3.5 (b).

Considering the ligating properties of pyridine groups, this interaction should form between the lone pair containing nitrogen and the metal. Therefore, we first consider the interaction of salt (M^{n+}) and pyridine molecules, with the P2VP core acting as a multidentate ligand for polymer-salt complexes. Two distinct interaction groups can be considered for simplification: the interaction of M^{n+} with the nitrogens on neighbouring 2VP units on the same backbone and the interaction of M^{n+} with the nitrogens on 2VP units on separate chains, as shown in the toy schematic in Figure 3.5(c). A distinct difference for the two cases would be a distortion of the back bone in the former and increased stiffness of the inter-chain interactions in the latter. These effects would lead to an change in bond lengths of the effected groups. An increase in bond length would lead to a shift to higher frequencies and therefore, higher vibrational shifts. [162] The specific functional groups that might be affected by such an interaction are given in Figure 3.5 (e). The Raman spectra in Figure 3.5 (d) shows the simulated Raman spectra in the region of interest of the molecule showed in the inset as acquired from Wiley Know-it-all compared against the pristine PS-b-P2VP micelle Raman spectrum.

In an attempt to confirm the modes emerging from individual functional groups, we can compare the simulated modes with assigned experimental modes of the polymer. The particular groups of interest as shown in Figure 3.5 (e) are labelled red in the Fe-bipy schematic shown. The modes for the $-\mathrm{CHR}_3$ and $\mathrm{R}-\mathrm{CH}_2-\mathrm{R}$ groups emerge from the backbone. They are expected around 1400-1470 cm^{-1} and 1370-1390 cm^{-1} for antisymmetric and symmetric deformations for $-\mathrm{CHR}_3$ and 1440-1480 cm^{-1} for bending deformation for $\mathrm{R}-\mathrm{CH}_2-\mathrm{R}$. These modes are identified and assigned as $\nu(13)$, $\gamma(\mathrm{CH2})$ and $\delta(\mathrm{CH2})$ in Table 3.3. For the $\mathrm{Ph}-\mathrm{R}$ groups, a number of ring modes are expected with stretching and a combination of bending-stretching modes are expected between 1430-1620 cm^{-1}. CH bending modes emerging from in-plane H bending are also expected between 990-1180 cm^{-1}. These modes are identified and assigned as $\nu(8\mathrm{a})$, $\nu(8\mathrm{b})$, $\nu(19\mathrm{a})$, $\nu(19\mathrm{b})$, $\nu(9\mathrm{a})$, $\nu(15)$, $\nu(18\mathrm{b})$, $\nu(18\mathrm{a})$ and $\nu(1)$. Since the styrene and vinyl-pyridine contain a lot of the same groups, the simulated modes cannot be used to distinguish between the two blocks. Similarly, the simulation is based on database calling for each group, specific modes with loaded polymer could not be simulated using Know-It-All. Therefore, these simulated modes can be used to identify the groups in proximity to the transition metal and discuss the selectivity of enhancement in terms of specific functional groups.

Looking at the Raman spectra with respect to the addition of precursor salt shows the evolution of the loading peaks with increasing salt addition, as can be viewed in Figure 3.6 (a). With the neat polymer, typical PS-b-P2VP modes are observable as listed in Table 3.3.

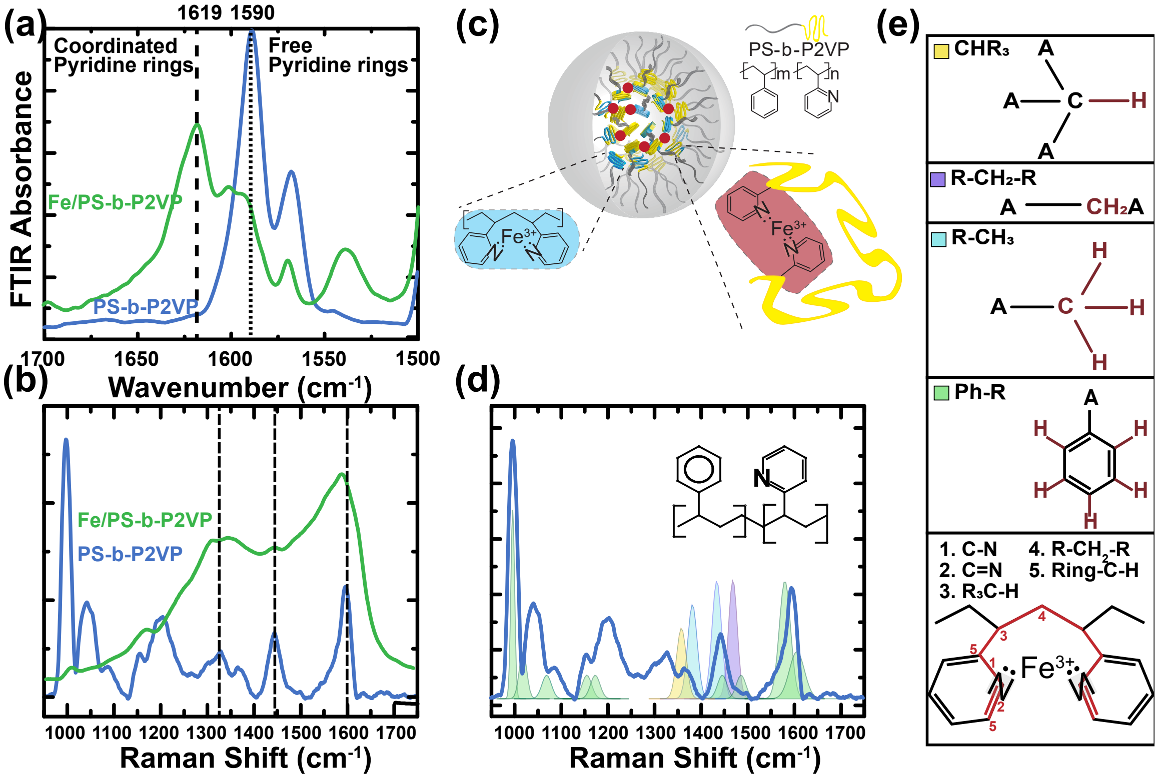

Figure 3.5: (a) FTIR and (b) Raman spectra of neat PS-b-P2VP (blue) and $FeCl_3$-loaded PS-b-P2VP (green) with the peaks expected for free and coordinated pyridine rings indicated. (c) Toy schematic of loaded micelles showing possible Fe-salt coordination with 2VP monomers on the same chain and on different chains. (d) Simulated Raman modes for the functional groups in (e). The inset in (d) shows the structure of the molecule for which the spectra was simulated. (e) The particular groups from the diblock copolymer unimer that would be affected by metal ligation by the lone pair.

Table 3.3: Expected Raman mode of PS-b-P2VP copolymer [53, 54, 163]

Wilson's Notation	Raman Shift (cm^{-1})	Polymer Block	Mode
ν(8a)	1612	PS	
ν(8a)	1602	P2VP	Ring stretching mode
ν(8b)	1583	P2VP	
ν(19a)	1482	P2VP	
δ(CH2)	1456	PS/P2VP backbone	methylene deformation
ν(19b)	1443	P2VP	Ring stretching mode
γ(CH2)	1332	PS/P2VP backbone	twisting modes
ν(13)	1224	PS/P2VP backbone	C-C stretching (ring and backbone)
ν(9a)	1196	PS	
ν(15)	1170	PS	
ν(15)	1160	P2VP	CH in-plane bending
ν(18b)	1064	P2VP	
ν(18a)	1040	PS	
ν(1)	1012	PS	totally symmetric ring breathing
ν(1)	1005	P2VP	

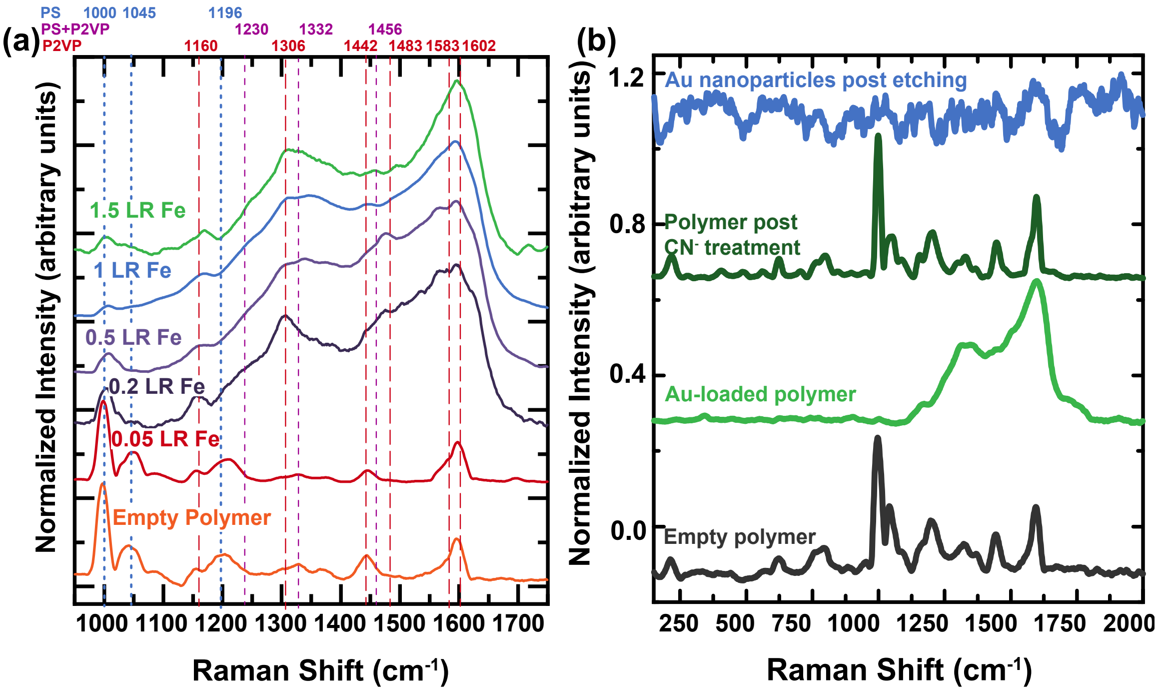

Figure 3.6: (a) Raman spectra of neat polymer and $FeCl_3$-loaded polymer with respect to [$FeCl_3$]:[2VP] ratio (b) Raman spectra of neat, $HAuCl_4$-loaded polymer, Au nanoparticles after polymer removal and recovered polymer after cyanide assisted salt removal.

As the amount of salt increases, peaks assigned to P2VP ring stretching modes (ν(19b), ν(19a), ν(8b) and ν(8a)) increase in intensity while peaks assigned to PS (ν(1), ν(9a), and ν(18a)) or total symmetric modes of P2VP (ν(1)) decrease in intensity. A shoulder peak can be observed around 1150 cm^{-1} which can be attributed to the CH-in plane bending in the PS ring and the P2VP ring, but considering the enhancement of other P2VP modes, it is safe to assume that the visible shoulder is also P2VP related. Similarly, another shared mode that appears to be enhanced can be attributed to the twisting modes of the polymer backbone (γ(CH2)) centered around 1320 cm^{-1}. With this mode, it is assumed that the enhancement is emerging from the P2VP backbone as opposed to the PS backbone.

We have confirmed that the interaction is a ligation type with a metal salt ion, as the enhancement of the P2VP mode is dependant on the presence of the metal salt and is reversible if the salt is removed. This is evident in Figure 3.6(b) which shows the Raman spectra of the polymer loaded with $HAuCl_4$, which shows similar enhancement in the region of the Fe-P2VP interaction. As CN^- forms strong colored complexes with $HAuCl_4$ and is a stronger ligand than pyridine, treatment of the loaded polymer should leach the ions but leave metallic compounds behind. After KCN treatment the Raman spectrum is identical to neat polymer, confirming the successful removal of the loaded salt. By contrast, as Au metal and oxides are not Raman active, etching the loaded polymer with oxygen plasma results in a featureless spectrum from gold nanoparticles.

We have observed that these loading peaks constitute a true enhancement of the polymer signal. As shown in Figure 3.7, the neat polymer spectra under normal Raman spectroscopy is not visible for samples thinner than 6 spin-coated layers ($\sim$

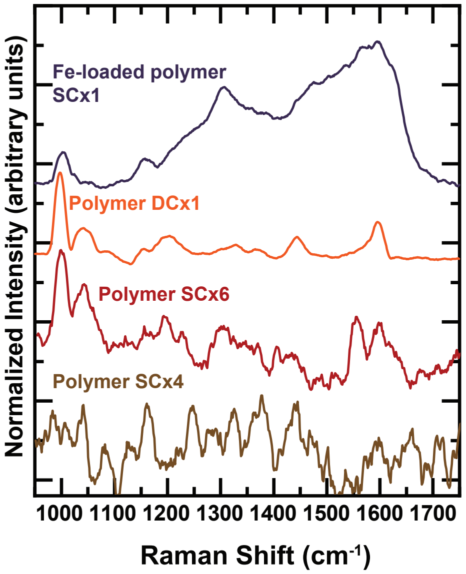

Figure 3.7: Raman spectra of varying volumes of neat polymer and a monolayer of Fe-loaded polymer.

100-120nm), requiring multiple depositions or even drop-casting to resolve the spectral features. As a result, spin-coated monolayers ($\sim$ 20nm) of neat micelles are invisible to normal Raman [44]. By contrast, a single monolayer of spin-coated $FeCl_3$-loaded micelles are easily visible [17]. Therefore, the enhancement offered by the loading of polymer is two-fold. Firstly, there is a greater signal from a smaller amount of material and secondly, only certain modes benefit from this enhancement.

This effect is reminiscent of enhanced Raman techniques, such as surface enhanced Raman spectroscopy (SERS), where selective enhancement occurs due to a combination of plasmonic resonance and of chemical resonance through charge transfer bands [44, 148, 149]. Though enhancement of Raman modes are unlikely to result from plasmonic effects in salt-loaded micelles, chemical enhancement may play a role in metal salt and polymer interactions in the absence of plasmonic generation. Charge-transfer would be expected to occur between the metal and ligand states due to vibronic coupling of the highest occupied and lowest unoccupied molecular orbitals (HOMO and LUMO) of the metal and the excited and ground states of the ligand. These so-called Herzberg-Teller contributions or resonance Raman enhancement of vibrational modes would be expected to emerge from metal-ligand and ligand-metal charge transfer while conserving the normal Raman selection rules [148,149,155,157].

For the $FeCl_3$-2VP complex formed, σ bond due to the electron lone pair of the Nitrogen and the delocalized $\pi*$ orbital from the ring overlap with the E_g and T_{2g} of the metal. [122] This supplies the charge transfer band for the resonance-enhanced excitation of the ring and backbone modes of the polymer in proximity to the salt. Since, the Raman modes of interest observed between 900 and 1750 cm^{-1} are clearly polymer modes, we can identify functional groups of the polymer that overlap closest with the coordination of the metal. These functional groups contributing to the overlapping states are also indicated in the schematic in Figure 3.5 (b).

Expanding this concept to other salts, it can be seen that there are some salts for which this enhancement is observed but others for which it is not. Transition metal salts, including $CuCl_2$ [164], $AlCl_3$ [165], $HAuCl_4$ [166], and $ZnCl_2$ [167], have been used to form complexes with the nitrogen on the pyridine ring due to the same interactions observed with $FeCl_3$. [122, 124, 126, 168] Figure 3.8 shows the Raman spectra of polymer micelles loaded with different salts and AFM images of their corresponding nanoparticles after polymer removal. The characteristic loading peaks are clearly visible in the Raman spectra of $HAuCl_4$-loaded, $FeCl_3$-loaded, $CuCl_2$-loaded and $AlCl_3$-loaded but absent for $ZnCl_2$-loaded polymer, even though all salts show nanoparticle formation. The modes for $ZnCl_2$-loaded polymer match the relative intensities of neat polymer. However some shifts in the spectral features around 1050

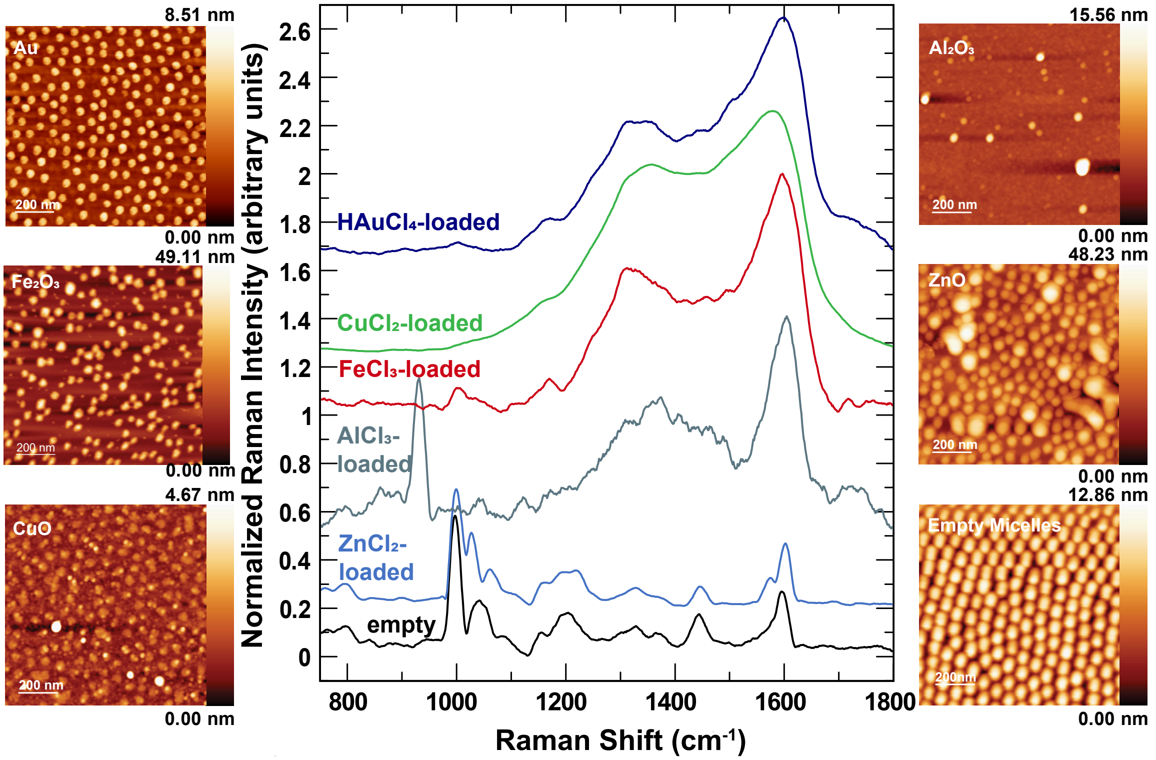

Figure 3.8: Raman spectra of neat polymer and salt-loaded polymer and AFM images of nanoparticles after polymer removal.

cm^{-1} and 1590 cm^{-1} are visible. These can be attributed to the ring stretching and breathing modes of P2VP and shifts in the Raman spectra could indicate changes in the bond vibrations due to a complex formation with $ZnCl_2$. With the other salts, changes in intensity are drastically different from the neat polymer, and while the enhanced peaks acquire a similar 'shape', the relative intensities and shifts in modes are different for different salts.

These features can be deconvoluted into the potential polymer modes identified for enhancement in Figure 3.5 (e) to compare the differences between different salt interactions. Figure 3.9 shows the fitted Raman spectra and peak centers for neat polymer and loaded polymers with assignment of the various modes given in the enclosed table. As with the case of $FeCl_3$-loaded polymer, the peaks observable with $HAuCl_4$, $CuCl_2$ and $AlCl_3$ loaded polymers can be assigned to 2VP modes while the modes from the PS fraction are absent. The signal to noise ratio for the $AlCl_3$-loaded spectra is considerably lower compared to the other salts and it shows an additional peak around 950cm^{-1}. As the nanoparticle layer also showed a low density of nanoparticles suggesting incomplete loading of micelles, this decreased intensities is likely related to the loading density of the polymer, as observed in Figure 3.6 for low $FeCl_3$-loading ratios. This suggests that better loading of $AlCl_3$ would lead to better loading peaks, as a planned follow-up experiment.

Of note is that the peaks observable in the loaded spectra have slightly shifted centers compared to the neat polymer with the ring stretching modes, $\nu(19)$ and $\nu(8)$, and the backbone twisting mode, $\gamma(CH_2)$, moving to higher Raman shifts. This is consistently true for all salts except $AlCl_3$ which shows a shift to lower shift for the backbone mode, $\gamma(CH2)$, at 1302 cm^{-1}. Raman spectra are sensitive to changes in bond length, and a decrease in the shift suggests a decrease in the bond length of the backbone for $AlCl_3$. It is also possible that the polymer mode is visible due to the low loading density of the $AlCl_3$ samples as discussed previously.

The loading of precursor salt results in stiffening of the P2VP micelle core due to the formation of the salt/P2VP complex and the resulting stearic repulsion between adjacent P2VP chains and 2VP units on the same chain. Quantitative nanomechanical mapping of loaded micelles [12, 169] shows increased Young's modulus of the micelle interior compared to unloaded micelles. In absence of the resonance enhanced peaks, as with $ZnCl_2$-loaded micelles, the intensity of Raman polymer modes show similar intensities to the neat polymer with some additional peaks and shifts. These additional peaks can be attributed to C-C stretching between the ring and the backbone while shifts are observed in the peaks for ring stretching and breathing modes. These shifts and additional peaks may tentatively be considered characteristic of loading and the stiffening of the micellar core in the absence of the enhancement of 2VP modes, subject to confirmation with other salts.

In normal Raman, the scattered intensity (I) follows a dependance on ν^4,

$$I \propto (\nu_0 + \nu_k)^4$$

where ν_0 is the excitation frequency and ν_k is the frequency of kth vibrational mode and the plus indicates Stokes radiation. With resonance Raman, this dependance becomes complex as the excitation wavelength approaches the frequency of transition from the ground state to a coupled excited state [158]. This enhancement of intensity is specific to normal modes that are efficiently coupled to excited states. [158] The restriction of enhancement localizes to only those modes that are coupled effectively. In the case of loaded polymer, this behaviour can be used to explain the observed enhancement of P2VP modes over PS modes. Under these conditions, the enhancement would be dependant on coupled excited and ground states of the metal and 2VP and the availability of charge transfer states which are close to the frequency of the excitation wavelength. For enhancement to be observed then, there should be available charge transfer states close to the excitation wavelength of the spectra, which in this case was 514.5 nm, which can be examined using the absorption behaviour of the salts.

The absorption spectra of $FeCl_3$ complexes show a maxima at 365 nm, which has been identified as a charge transfer band, and weaker peaks up till 728 nm, which

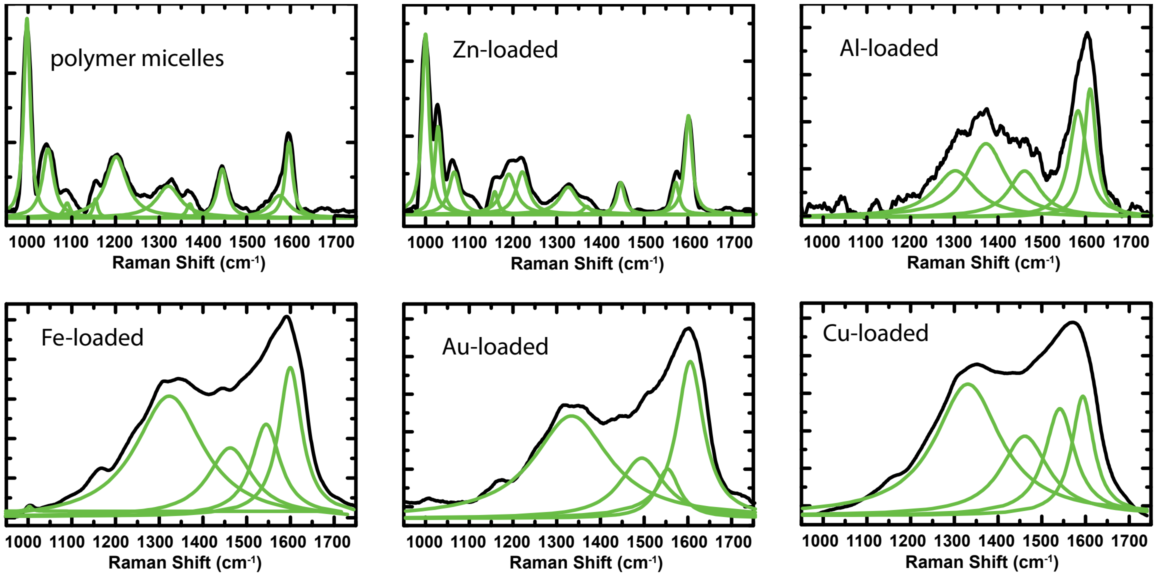

Cu	Zn	Al	Au	Fe	Polymer			
Raman Shift						Mode		
	999			1005	997	v(1)	PS+ P2VP	totally symmetric ring breathing
	1028				1045	v(18a)	PS	
	1065				1089	v(18b)	P2VP	
	1158				1153	v(15)	P2VP+PS	CH in-plane bending
	1190				1201	v(9a)	PS	
	1221							
1335	1326	1302	1330	1325	1320	γ(CH2)	Backbone	twisting modes
	1368	1372			1370		Backbone	
	1446				1444	v(19b) / v(19a)	P2VP	
1467		1460	1491	1464				Ring stretching mode
1548	1572	1583	1550	1546	1575	v(8b)	P2VP	
1602	1601	1610	1602	1602	1596	v(8a)	P2VP	

Figure 3.9: Fitted Raman spectra of pristine and salt-loaded polymer micelles and the table of peak centers with assignment for each spectra.

have been attributed to d-d transitions [170]. $CuCl_2$ forms octahedral complexes with non-sterically hindered aromatics like pyridine but results in square-planar arrangement with sterically hindered aromatics like 2-methylpyridine due to Jahn-Teller effects for stability. A distorted octahedral (square planar) complex is expected from $CuCl_{2/}P_2VP$, which results in further splitting of the respective T_{2g} and the E_g states. Therefore, for $CuCl_2$/2VP complexes, a complicated electronic spectra has been reported as extending from the UV into the IR, with the strongest peak around 365 nm and extending up to 865 nm. Peaks were reported at 605, 830, 970 and 1750 nm. [164]. Au(III) complexes exhibit a square planar geometry and, in particular complexes with pyridine derivatives, show absorption bands around 400 nm-440 nm, emerging from Ligand-to-Metal charge transfer bands. [166, 171].

$AlCl_3$, though it is not a transition metal, acts as a Lewis acid and therefore can form adducts with lone pair donating groups. Aluminum complexes form a similar group of complexes as Fe^{3+} and can occupy octahedral and tetrahedral geometries, including anionic and cationic species with chlorides [165]. Though no specific studies on $AlCl_3$ interactions with P2VP exist, charge transfer effect in $AlCl_3$-based aromatic complexes has shown absorptions, ranging from UV to mid-visible ranges depending on the strength of interaction with the ligand, with stronger interactions leading to absorbance of longer wavelengths [172].

On the other hand, $ZnCl_2$ is not a transition metal as it has a filled d-shell restricting the role of the d-orbitals in d-π orbital overlap for charge transfer [173]. However, it typically shows similar coordination behaviour with ligands as that observed with the transition metals. Due to its filled d-shell, zinc chloride does not show absorption bands when forming complexes with aromatic compounds at room temperatures, but does so at elevated temperatures where it forms colored compounds. [174]. The color signifies electronic transitions in the visible region. Though it may be possible to observe similar resonance enhanced features for such zinc compounds, those temperatures are not accessible for the salt-loaded compounds, as they are higher than the critical transition temperature for PS-b-P2VP, therefore it was not possible to confirm their presence.

Considering that only $HAuCl_4$, $FeCl_3$, $CuCl_2$ and $AlCl_3$ complexes exhibit absorption within the range favourable for resonance enhancement of the P2VP modes, these are the salts for which enhancement due to salt loading are observed in visible range Raman excitation. Further support for this proposed mechanism can be collected by expanding to other salts such as cobalt chloride, manganese chloride or platinum chloride, all of which show charge transfer bands and electronic transitions which exist in the visible part of the electromagnetic spectrum. An interesting case to investigate would be for metals salts which do not show any visible absorbances similar to $ZnCl_2$. In this case, nickel chloride would be a candidate, where it should show resonance only when excited in the UV as suggested by its absorption spectra [168]. This suggests further studies of using other excitation wavelengths for Raman of loading behaviour in such salts could be used to confirm this behaviour.

3.2.4 Conclusion

Reverse micelle deposition is a solution based technique which allows us to self-assemble monolayers of templated nanoparticles. There are two approaches that can be used to confirm the infiltration of the salt into the micelle. First, nanostructures can be observed after polymer removal under AFM, which is time consuming and provides no other information about the synthesis process. On the other hand, Raman spectroscopy provides a fingerprint in the characterization of neat and loaded micelles due to the existence of enhanced 'loading' peaks with some salts. Raman is relatively fast in-situ approach to probing the successful loading of the polymer, while also giving insight into the interaction between the salt and the polymer by peak convolution. In this article, we have discussed the mechanism of selective enhancement of P2VP modes over PS modes in salt-loaded PS-b-P2VP micelles in terms of resonance Raman spectroscopy. The mixing of states and allowed metal-ligand and ligand-metal charge transfer bands lead to a resonance-based enhancement of P2VP modes in proximity to precursor metal salt in the absence of plasmons. The vibronic coupling and charge transfer effect allow for the observation of thin films down to monolayers and it can be utilized as a screening mechanism for effective loading as the enhancement scales with loading ratio. For salts which exhibit visible absorption charge transfer bands upon complexation with pyridine ligands, it is possible to use visible excitation to stimulate loading peaks using resonance Raman effects. If there is no visible absorption, it may be possible to use other excitation wavelengths to examine the process of complexation. Correlating absorption with Raman may be a way forward to in-situ spectroscopy during nanoparticle fabrication which is not possible by other methods. We have also described a method of removing the loaded salt from the polymer to revert to its pristine state using strong ligands like CN^-.

Chapter 4

Monolayer of ordered Iron Oxide nanoparticles

4.1 Publication: Role of hydration and micellar shielding in tuning the structure of single crystalline iron oxide nanoparticles for designer applications

Declaration

Role of hydration and micellar shielding in tuning the structure of single crystalline iron oxide nanoparticles for designer applications (Nano Select 2021, 2, 2419)

Authors: Ramis Arbi, Amr Ibrahim, Liora Goldring-Vandergeest, Kunyu Liang,

Greg Hanta, Lok Shu Hui, Ayse Turak

This manuscript has been published in **Wiley Nano Select** on **12th May 2021** on the cited page and volume numbers and is available at the following link

https://doi.org/10.1002/nano.202100085

4.1.1 Introduction

Iron oxide nanoparticles have attracted considerable attention for both fundamental and practical reasons, as they are low cost, eco-friendly and easy to prepare. The naturally occurring crystal phases, α-Fe_2O_3, γ-Fe_2O_3, and Fe_3O_4, have been widely used in diverse applications, as each has unique biochemical, magnetic, and catalytic effects.

α-Fe_2O_3, the most stable iron oxide, has found application in gas sensors, photoelectrodes, photocatalysts, and batteries [35, 175–179] due to its high resistance to corrosion, selective absorption, useful bandgap, and low cost. γ-Fe_2O_3, the second most common Fe_2O_3 polymorph has been exploited in storage media, biomedical sensors, drug delivery systems, magnetic resonance imaging, and water-splitting electrocatalysis [35, 180–184] due to its biocompatibility, biochemical properties and unique magnetic features. Iron oxide nanoparticles are in general interesting for their magnetic response, which can be attributed to the γ-Fe_2O_2 and Fe_3O_4 spinel phases. Diverse applications take advantage of the different physicochemical attributes of the different polymorphs. Being able to tune the crystal structures from one pure monophase to another would allow the specific tailoring of the nanoparticles for desired applications.

Due to their closely related crystal structures and stoichiometries, phase transformations between the various iron oxide polymorphs are possible during synthesis and application [176, 185–193]. This has prompted investigation into the formation mechanisms of the polymorphic phases and the transitions between them. Different factors including particle size, synthesis process, level of hydration and temperature have been seen to influence the transition [179]. γ-Fe_2O_3, particularly, is in an intrinsically metastable state, with the inverse spinel structure tending to convert into the more thermodyamically stable hexagonal α-Fe_2O_3 phase [194–196]. As the transition from γ to α is dependent on whether the particle has enough energy to overcome the activation barrier, there is a critical size and temperature below which γ dominates [190, 197–199]. Yet, the level of hydration has also been seen to drastically affect the synthesis process to preferentially favour the formation of one phase over another [190,198]. With α-Fe_2O_3 being a a weakly ferrimagnetic material, it is necessary to limit its formation to achieve nanoparticles with significant magnetic response independent of size [43]. Unlike the transformation between α and γ phases, the transformation between Fe_3O_4 and γ-Fe_2O_3 are compositional without any structural change, with arbitrarily distributed cation vacancies forming at octohedral sites [55]; hence temperature can play a significant role in nanoparticle phase stability. At high temperatures, even Fe_3O_4 nanoparticles may oxidize directly to α-Fe_2O_3 [55]. Such phase instability can result in changing electronic response over time, which is known to affect the effectiveness of iron oxide based electrocatalysts [193]. Insight into the mechanisms of formation and phase transition are therefore highly desirable to control nanoparticle synthesis to target favourable properties.

Various methods have been employed for the synthesis of stable monodispersed nanoparticles. This involves the use of different bottom-up approaches such as co-precipitation [200–203], sol-gel synthesis [204,205], chemical reduction [206], bio/green-synthesis [207], epitaxial growth [208, 209], vapor deposition [210–212] and diblock copolymer lithography [12, 31, 43]. Each technique has its merits in terms of the types of materials synthesized, ease of growth and feasibility in terms of resources used. Passive self-assembly techniques have an upper-hand in this regard, allowing control of the final structures and compositions through manipulation of the process parameters, since no active control has is required throughout the process. This is a benefit for deposition as specialized surfaces are not required, as is often the case in lithography techniques or top-down approaches.

We have recently shown that it is possible to produce highly monodisperse, pure γ-Fe_2O_3 nanoparticles with a narrow size distribution and controllable particle size, using a diblock copolymer reverse micelle template [43]. The self-assembly of macromolecules to aid in the formation of nanopatterns is a rapidly growing area, as a route to functionalize surfaces with tunable surface wettabillity [64, 65], overlayer adhesion [66], catalytic activity [67] or work function [30, 108, 109]. The complex interplay of various parameters, including stirring times, precursor loading ratios, solvents, co-polymer molecular weights, or the ratio of blocks, results in a wide tunability of particle size, polydispersity and crystal structures [12]. Moreover, these nanoparticles can be transfer-printed on to substrates that may be sensitive to direct processing [42].

In this contribution, we use the chemical fingerprints from Raman spectroscopy to explore the impact of modifying the growth conditions and post-deposition treatments on the formation of iron oxide nanoparticles. The shielding environment of the micelles was seen to prevent the formation of a hydrated phase that can directly convert to the thermodynamically stable α-Fe_2O_3 at low temperatures. As a result, the micelle environment is able to stabilize the highly desirable magnetic spinel phases. Our approach allow us to challenge the current concept that the α- to γ- phase transition is necessarily driven by particle size, as we are able to produce multiple coexisting phases while maintaining a fixed particle size. Based on these findings, we are able to effectively tune the nanoparticle crystal structure in a spectrum from 100% inverse spinel phases (γ-Fe_2O_3, Fe_3O_4) to 100% hexagonal phase (α-Fe_2O_3) simply by manipulating the processing parameters. This can be used to tailor designer nanoparticles with fixed size and tunable composition for applications that exploit the specific properties of different polymorphs.

4.1.2 Results and discussion

Effect of type of polymer on iron oxide phases formation

Raman is a vibrational spectroscopy technique which can be used to investigate crystal structures and molecular vibrations using inelastic scattering [213]. The crystal structures of Fe_xO_y polymorphs, and hence the the vibrational modes and Raman spectra of α, β, ϵ and γ of Fe_2O_3, Fe_3O_4 and $FeCl_3$ have been observed to be distinct from each other [46,47,74,213–216] as outlined in supporting information **Table SI-1**†.

Using group theory, the active Raman modes of a system can be predicted. γ-Fe_2O_3 with the *P4₁32* space group has five active Raman modes (A_{1g}, E_{1g} and 3 x

T_{2g}), mathematically describing their atomic vibrations against their principle rotational axis and inverse structures. Though γ-Fe_2O_3 and Fe_3O_4 belong to the same space group, the observed Raman modes at similar wavenumber have a different atomic origin, making them easily distin- guishable [46,217]. α-Fe_2O_3 ($R\bar{3}c$) has five E_g modes, though two are typically resolvable only below 100K [218], and two A_{1g} modes.

Recently, we used the Raman signatures of the precursors, the co-polymers and the various iron oxide polymorphs to describe the formation process of γ-Fe_2O_3 during synthesis using polystyrene-*block*-poly(2vinyl pyridine) (PS-*b*-P2VP) reverse micelles [43]. We found that when $FeCl_3$ interacts with the P2VP block inside the micelles, it induces two additional Raman modes, attributed to the stearic hinderance of Fe-2VP complexation around 1306 cm^{-1} and 1591 cm^{-1} [43]. This complexation is essential to encourage the infiltration of the precursor salts into the micelle environment.

However, complexation itself does not seem sufficient to form a particular oxide polymorph. To examine this effect, we used PS-*b*-P2VP copolymers with different molecular weights (MW) to template iron oxide nanoparticles. **Figure 4.1** shows the Raman spectra of nanoparticles produced using micelles of lower and higher MW under identical post-etching treatment, with Lorentzian peak fitting to show the existing phases (see supporting information **Figure SI-1**.)†

Figure 4.1 (a) shows the iron oxide nanoparticles immediately after etching with no heat treatment applied. For the upper spectrum, nanoparticles produced using the PS-*b*-P2VP with the higher MW show the broad peak around 700 cm^{-1} which can be deconvoluted with two Lorenzian peaks at 671 cm^{-1} and 721 cm^{-1} which are the A_{1g} stretching mode of tetrahedral units of Fe_3O_4 and γ-Fe_2O_3 respectively [46,189,219].

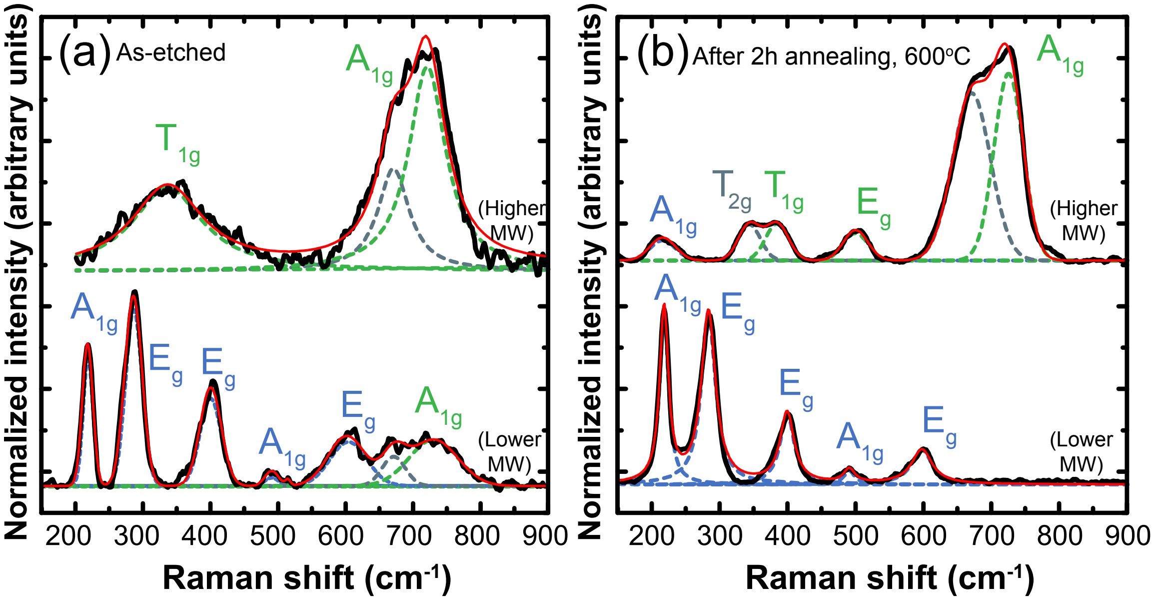

Figure 4.1: Normalized Raman spectra of the iron oxide nanoparticles (a) after etching under O_2 plasma, and (b) after annealing at 600°C for 2h in N_2 with Lorentzian peak fitting for nanoparticles formed using PS-*b*-P2VP diblock co-polymer of (upper) higher and (lower) lower molecular weights.

The peak centred around 350 cm^{-1} could be assigned as the translatory T_{2g} of Fe_3O_4 (330 cm^{-1}) and the T_{1g} of γ-Fe_2O_3 (340 cm^{-1}) [46, 189, 217, 220]. As no other features are observed, using higher MW PS-*b*-P2VP results in the formation of nanoparticles of a purely spinel phase.

On the contrary, the Raman spectra acquired from nanoparticles produced using the lower MW PS-*b*-P2VP in Figure 4.1 (a) show five additional peaks characteristic of α-Fe_2O_3. Three can be assigned to symmetric double-degenerate E_g modes [218, 220, 221] – 292cm^{-1} (vibrations due to Fe atoms), 409cm^{-1} (vibrations of O ions with respect to the Fe ions in the plane perpendicular to the c-axis of the hexagonal unit cell) and 610cm^{-1}. The other peaks at 223cm^{-1} and 497cm^{-1} could be assigned to the A_{1g} stretching modes of α-Fe_2O_3 due to the vibrations of Fe ions moving along the c-axis of the hexagonal unit cell and O ions moving along the c-axis of the hexagonal unit cell respectively [218, 221].

After annealing at 600°C for 2 hours under N_2 environment, for the lower MW co-polymer template, the A_{1g} peaks of Fe_3O_4 and γ-Fe_2O_3 disappear, leaving only the five distinct peaks, suggesting purely hexagonal phase of α-Fe_2O_3 [217, 218, 220]. The formation of crystalline iron oxides was also confirmed by x-ray diffraction, x-ray photoelectron spectroscopy, electron energy loss spectrscopy, transmission electron microscopy, and selective area diffraction measurements (see supporting information **Figure SI-3**†).

With the higher MW co-polymer template, annealing leads to the peaks associated with spinel phases becoming more intense and sharply defined, with the emergence of a peak at 509 cm^{-1} for the E_g mode of γ-Fe_2O_3. This suggests increased crystallinity of γ-Fe_2O_3. Such high temperature annealing has been proven to increase the crystallinity of reverse micelle templated γ-Fe_2O_3 nanoparticles [43]. However, an additional peak is also seen which can be assigned to the A_{1g} peaks of α-Fe_2O_3 at 225 cm^{-1}. [217, 218, 220]. Liang et al. [43] observed prolonged high temperature annealing resulted in the formation of α-Fe_2O_3, and also observed that even 2 hours annealing at 600°C lead to a loss of magnetic susceptibility [43], supporting the existence of a mixed phase. (See supporting information Section SI-7)

The nanoparticles obtained from the higher MW PS-*b*-P2VP result in a higher yield of the spinel phases with a uniform size, periodic distribution on the surface, and lower variability in the particle diameters compared to the lower MW PS-*b*-P2VP (see supporting information **Figure SI-4**†). Additionally, it is observed that a pure α-Fe_2O_3 phase is achievable using the polymer with the lower MW, and pure spinel phase is achievable using the polymer with higher MW. Though Ayyub et al. [199] had observed size-induced transitions in nanocrystalline Fe_2O_3, with particles bigger than 30nm dominantly being α-Fe_2O_3 and those smaller dominantly γ-Fe_2O_3, we observed this behaviour for particles of the same average particle size (~30nm), see supporting information Figure SI-4)†. In fact, the γ-Fe_2O_3 particles were larger than the α-Fe_2O_3 ones on average (36nm vs 27 nm), and this particle size was unaffected by annealing. As a result, we can confirm that this difference does not arise from particle size effects. Therefore, there is a clear influence of the type of polymer on the resulting phases of Fe_xO_y observed.

To understand how the polymer can affect the structure of the nanoparticles, we examined the differences in the micellar geometries formed and the infiltration of the precursor. **Figure 4.2** shows the impact of loading the two PS-*b*-P2VP polymers, as well as a homopolymer HP2VP loaded with $FeCl_3$ precursors.

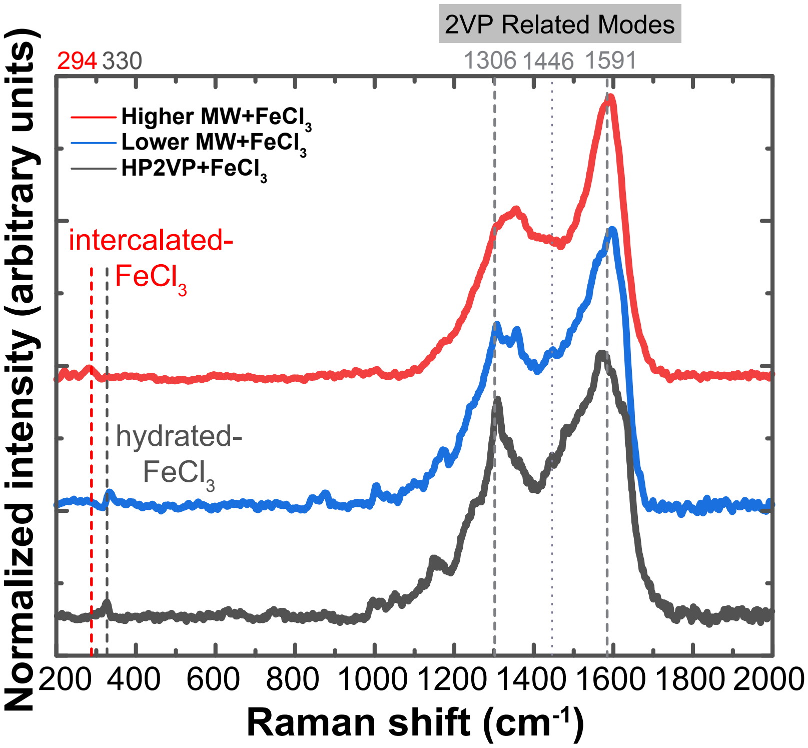

Figure 4.2: Raman spectra of the FeCl$_3$ loaded in the two PS-*b*-P2VP copolymers & homopolymer HP2VP, showing the expected salt-2VP complexation peaks at higher wavenumbers in all cases. Both the lower molecular weight co-polymer and the homopolymer show a peak at low wavenumbers consistent with the hydrated iron chloride salt.

The process of iron oxide nanoparticle formation from a precursor salt loaded diblock copolymer micelle was recently described by us in Liang et al [43]. We identified four Raman modes of $FeCl_3$ loaded micelles which are characteristic of the complexation of $FeCl_3$ and 2-vinylpyridine (P2VP) [43]. These include the three pyridine related stretch modes, around 1306 cm^{-1}, 1440 cm^{-1}, and 1591 cm^{-1}, which are enhanced due to the interaction of the electron lone pair of nitrogen on the pyridine rings with the Fe. As can be seen in Figure 4.2, both co-polymers and the homopolymer spectra show these features, suggesting that $FeCl_3$ is complexated with the P2VP as expected. The third signature observed by Liang et al. was a peak around 290 cm^{-1}, which can be assigned to the A_{1g} of $FeCl_3$, shifted as a result of intercalation with P2VP [43, 222, 223].

Though the higher MW PS-*b*-P2VP shows the expected A_{1g} peak for intercalated $FeCl_3$ at 294 cm^{-1}, lower MW PS-*b*-P2VP shows a peak at 330 cm^{-1} which is consistent with the A_{1g} of hydrated $FeCl_3$ [216, 224]. A similar behaviour was observed for the homopolymer loaded with $FeCl_3$, as seen in Figure 4.2. In that case, the $FeCl_3$ salts complexated on the homopolymer HP2VP chain are exposed to water adsorbed on the KBr substrate during sample preparation. As $FeCl_3$ is highly hygroscopic, it is able to immediately form a hydrated phase. This was also observed when $FeCl_3$ without any polymer is deposited directly from o-xylene on the KBr surface (see supporting information **Figure SI-5**)†. Moreover, when homopolymer loaded $FeCl_3$ or pure $FeCl_3$ is plasma etched, characteristic peaks for the α-Fe_2O_3 phase can be observed (see supporting information Figure SI-5†).

Nanoparticles formed using $FeCl_3$ solutions with different procedures without micelles have also been shown to result in intermediate iron hydroxides which ripen into α-Fe_2O_3 [225]. Generally, adsorption and incorporation of water or hydroxyls is critical for stable α-Fe_2O_3 formation as particle size decreases (the hydroxyl mechanism) [190,198]. As the polymer complexated $FeCl_3$ which exhibit the hydrated phase (the polymer with the lower MW and HP2VP) result in a predominantly α-Fe_2O_3 phase, the formation of a hydrated phase during incorporation with P2VP seems to be a requirement for the formation of α-Fe_2O_3 at low temperatures from micelle templates. This is similar to that observed by Cui et al [226] for composite systems, where dried polymer xerogel composite results in γ-Fe_2O_3, where wet xerogel resulted in α-Fe_2O_3. For micelle templating, the polymer with the higher MW offers a protective environment for the $FeCl_3$ from water which both the polymer with the lower MW and HP2VP lack.

An analysis of the structure and characteristics of the two micelles without any salt loading allows us to develop a model of the different behaviour of the salt with the different micelles. As shown in **Table** 4.1, the two polymers have similar ratios of P2VP to PS blocks, with the lower MW polymer having a slightly greater abundance of P2VP units. As the $FeCl_3$ complexates with the 2-vinylpyridine, this suggests that the lower MW copolymer has more abundant sites for interaction.

Typically, in micellar formation, there is a correlation between the micelle size and the MW, as the molecular weight of each portion of a diblock copolymer is closely related to the block length. Generally, in diblock copolymer systems, longer chains are expected to result in a larger micellar size [5,10,227,228]. However, as can be seen in Table 4.1 that is not the case for these PS-*b*-P2VP systems. The average micelle diameters, as measured by SEM, were substantially larger for the lower MW micelles (see supporting information **Figure SI-6**)†. The trend holds when we compare the

SEM results to the lateral size observed in the AFM topography micrographs seen in **Figure 4.3**(a) and (b) (line profiles through one representative micelle shown in Figure 4.3(e) and (f)). However, the height of the micelle as measured in the AFM did not increase with lateral size, being similar for both.

Table 4.1: Comparison of micelle characteristics between lower molecular weight and higher molecular weight diblock copolymers.

Polymer characteristics	Higher MW	Lower MW
P2VP:PS ratio	0.89	1.29
M_n PS (g/mol)	75,000	28,000
M_n P2VP (g/mol)	66,500	36,000
M_n PS:P2VP (g/mol)	141,500	64,000
Micellar diameter (nm)[1]	41.12 ± 3.64	94.57 ± 4.01
Core diameter (nm)[1]	30.86 ± 4.10	74.66 ± 3.92
Corona thickness (nm)[1]	5.13 ± 2.74	9.96 ± 2.80
Micelle centre height (nm)[1]	9.54 ± 1.12	8.12 ± 0.95
Micelle core Young's Modulus (GPa)[1]	2.24 ± 0.05	0.17 ± 0.07
Hydrodynamic diameter (nm)	90.1 ± 0.78	159.8 ± 0.64
Polymer fraction of core (ϕ_{P2VP})	1.05	0.26

[1] average value determined by 100 measurements of different particles deposited on Si

Iodine staining was used to determine the inner core radius, as iodine is known to preferentially stain pyridine over polystyrene, due to the complexation of iodine and pyridine [229]. Using the difference in the measured micelle and core diameters, the thickness of the PS corona can also be estimated to get an idea of the size and shape of the resultant micelles. This analysis indicates that the higher MW copolymer has a smaller denser core compared to the lower MW one, which is twice the size despite the much shorter polymer chains.

Quantitative nanomechanical mapping (QNM) was employed using the AFM in tapping mode to understand the mechanical differences between the two polymers. QNM allows the measurement of the Young's modulus variation on a surface, and has been successfully applied to examining the properties of soft materials [230–232].

Figure 4.3 illustrates the AFM topography and QNM modulus variation, with the height and Young's modulus line profiles of a representative micelle in the bottom row. The line profile through the empty micelle for the higher MW copolymer indicates that its core is less stiff than the corona region, which is characteristic of empty micelles [12,232]. This lowering of the modulus through the core likely results from the anisotropic nature of polystyrene in the diblock copolymer. The diblock copolymers are aligned horizontally when the tip first interacts with the micelle and vertically as the tip interacts with the core; as the polystyrene has a higher Young's modulus when aligned laterally in a lamellar formation than vertically as in a polymer brush, the modulus is reduced through the core [232]. In the case of the lower MW polymer, though the Young's modulus in the corona region is similar to that of the higher MW polymer, it goes to zero at the centre with respect to the silicon substrate. This results in a "coffee bean" type structure observed in Figure 4.3 (d) on the Young's modulus map.

This effect, coupled with the small height as measured by AFM compared to the large micelle diameter, suggests that the lower MW micelles have collapsed on to the substrate when deposited. This behaviour provides a viable reason for why the lower MW polymer micelle is not able to shield the $FeCl_3$ precursor from hydration.

In the typical process of nanoparticle formation using micellar templates, micelles will form spontaneously in selective solvents when there are enough diblock copolymer unimers to be above the critical micelle concentration. In non-polar solvents such as

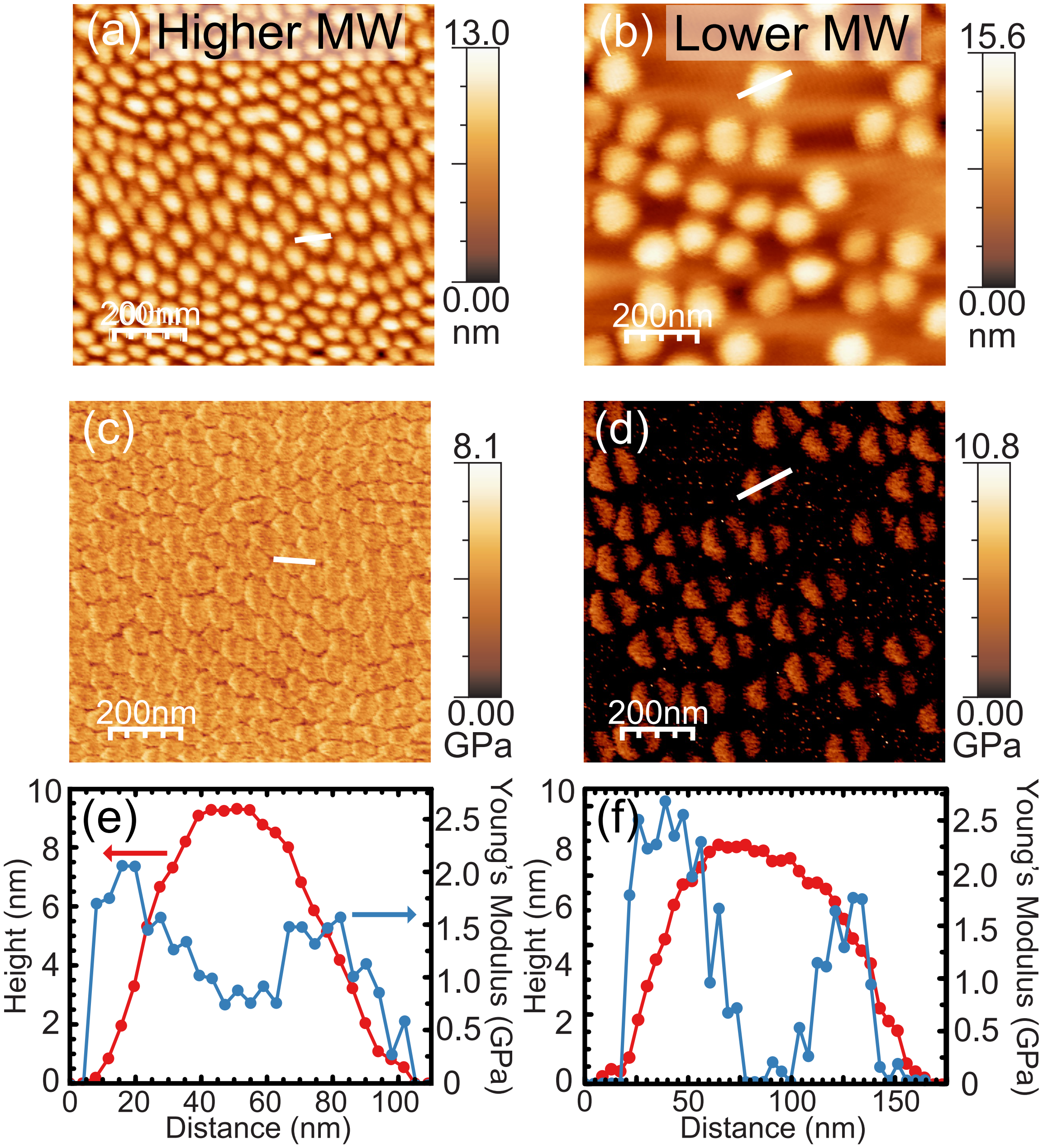

Figure 4.3: Quantitative nanomechanical mapping of the polymer micelles showing simultaneously collected topography and the corresponding elastic modulus (a) AFM topography of the higher molecular weight micelles (b) AFM topography of the lower molecular micelles (c) Young's modulus micrograph of higher molecular weight micelles (d) Young's modulus micrograph of lower molecular micelles (e) Line profiles for the higher molecular micelles (f) Line profiles for the lower molecular micelles

o-xylene or toluene which selectively dissolves polystyrene, PS-*b*-P2VP forms reverse micelles as shown schematically in **Figure 4.4**, where the hydrophillic P2VP block forms the micelle core surrounded by a hydrophobic corona of PS.

The spherical structure consists of loosely associated unimers, which are very dynamic with unimers regularly exchanging between the micelle and the solvent [3, 4, 233]. Above the critical micelle concentration, the unimers coalesce into a micelle, triggered in a non-polar solvent by entrapped water molecules [234]. The size and shape of the micelles in solution is driven by the molecular weight of the polymer chains, their interaction with the surrounding solvent, and the amount of entrapped water/solvent. Typically for strongly segregated copolymers such as PS-*b*-P2VP, the micelle cores are not expected to show significant swelling with solvent or entrapped water, and the polymer fraction of the core should be $\phi_{P2VP} \approx 1$ [228]. The hydrodynamic diameters, as determined by DLS, are given in Table 4.1. Again, the lower MW micelle has a measured diameter nearly twice that of the higher MW micelle. In both cases, the diameter is larger than that for the deposited particles measured in SEM, as expected, since the polystyrene corona has elongated into the solvent. Using the stained core diameter, we can estimate how densely packed the P2VP component is inside the core, using the assumption of a rigid spherical micelle [228] (see supporting information section SI5.1)†. In the case of the higher MW micelle, the expected dry core behaviour holds and the longer chains are packed together to form a tight P2VP core, as observed in the schematic Figure 4.4. On the other hand, for the lower MW micelle, there is significant swelling of the core, with only 26% consisting of P2VP chains, and the micelle balloons around solvent or entrapped water.

In both cases, the dynamic nature of the micelles allows the $FeCl_3$ to penetrate

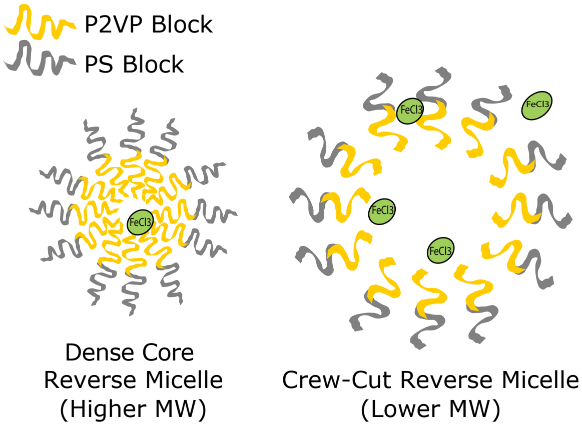

Figure 4.4: Schematic of $FeCl_3$ loaded micelles comprising the two polymers

through the corona due to the osmotic pressure of the non-polar solvent. Driven by the incompatible polarity between non-polar solvent and the polar metal salt, the precursor ions diffuse into the micellar cores. Once inside, the $FeCl_3$ then interacts with the P2VP chains. The loading ratio for the micelles is defined as the number of Fe^{3+} ions divided by the number of 2VP molecular units in PS-*b*-P2VP. In order to produce nanoparticles of ∼30nm in diameter, the higher MW micelle requires a much higher loading ratio than the lower MW micelle (1.5 vs 0.2 respectively, see supporting information Figure SI-4)[†] even though there are more available P2VP units for complexation. This suggests that it is relatively difficult for the precursor salt to penetrate inside the dense micelles, requiring 1.5 ions of Fe^{3+} per unit of P2VP in the solvent to infiltrate enough salt to form particles. However, once inside the salt is protected by both the PS and the P2VP unimers, which do not collapse when the solvent evaporates after deposition. This protects the $FeCl_3$ from water in the environment; upon plasma etching, due to the low temperature and the lack of a hydrated salt, the γ-Fe_2O_3 phase is able to form.

On the other hand, the large balloon-like micelles of the lower MW micelle allow easy infiltration of the salt while in the solution, requiring only 0.2 Fe^{3+} ions per P2VP unit to produce ∼30nm particles. This suggests that a large amount of salt is able to penetrate inside the micelle, some of which interacts the P2VP. However, either the existing pool of water inside the micelle or water molecules encountered when the micelle is deposited and collapses converts the Fe^{3+} precursor into a hydrated form. Due to the presence of this hydrate, it is extremely easy to form the α-Fe_2O_3 phase independent of particle size.

Dependent on which polymorph is desired, either polymer may prove useful. The higher MW dense core micelles to achieve γ-Fe_2O_3 and lower MW crew cut micelles to produce large α-Fe_2O_3 with minimal precursor and processing.

Effect of post-etching conditions on iron oxide phases

Upon deposition, the two micelle types already result in different phases of Fe_2O_3. Post-deposition annealing can also be used to systematically tune the structure, and enhance the crystallinity. High temperature annealing leads to a greater yield of the hexagonal phase, which is expected as α-Fe_2O_3 is thermodynamically more stable at higher temperatures [197, 199, 235]. **Figure 4.5** clearly confirms that irrespective of the polymer used initially, it is possible to achieve similar amounts of α and γ phases with annealing. As the lower MW micelle already started with a high level of α-Fe_2O_3, only a short annealing time at 600°C is required; for the higher MW micelle, however, the spinel phase is stabilized and it requires significantly more annealing time to achieve the α form.

The transition from γ to α is dependant on whether the particle has enough energy to overcome the activation energy barrier. In general, the smaller the nanoparticles

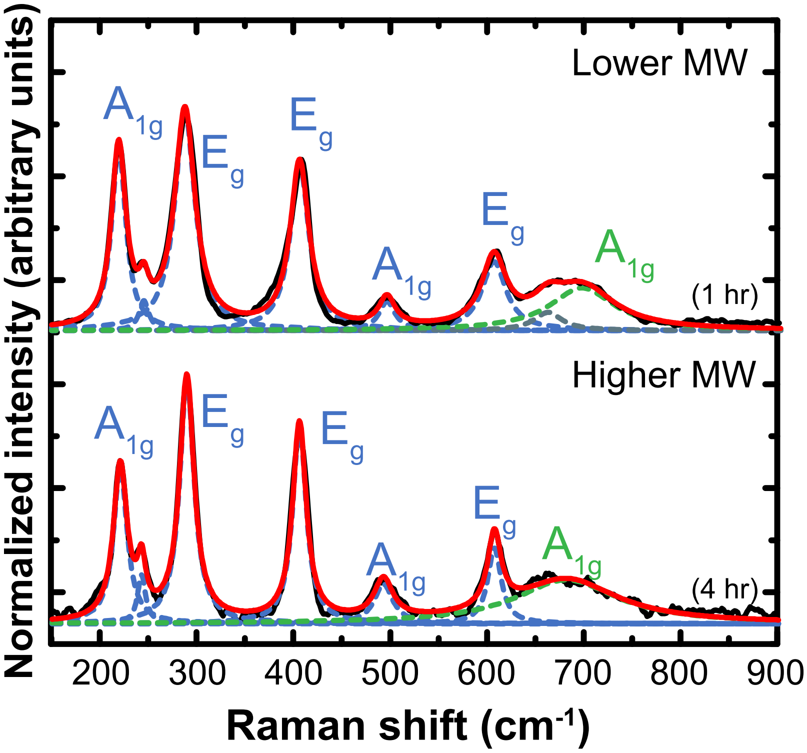

Figure 4.5: Raman spectra of the nanoparticles formed using the co-polymer with the lower molecular weight and higher molecular weight annealed at 600°C for different times to achieve the same percentage of α-Fe_2O_3.

of γ-Fe_2O_3, the lower the transition temperature [179]. For these nanoparticles, the transition temperature is expected around 500 °C or lower. Various strategies, including doping [177,213,236,237], nanocomposites [175,192], core-shell particles [175,238], and ligand functionalization [179, 191] have been adopted to reduce the excess free energy of the nanoparticles, increasing the phase transition temperatures.

As can be seen in **Figure 4.6**, we are able to achieve a stable spinel phase dominated by γ-Fe_2O_3 upto 700°C for nanoparticles without any stabilizing agents or confining composites. The γ to α transition is structural, requiring restacking of the oxygen layers from an FCC lattice to a HCP one and rearrangement of the Fe cations with the rigid O layers shifting into a new configuration [55, 194]. Commonly, this is accomplished by increasing the particle size, with ultrafine γ-Fe_2O_3 nanoparticles converting into large plates of α [194]. We do not observe any change in particle size with annealing, even upon conversion to the α-Fe_2O_3 phase. As the nanoparticles are in a restricted degree of agglomeration [179], due to the physical separation resulting from the micelle template, and there is no hydrate during formation, the phase transformation is heavily suppressed.

Additionally, interesting trends are also observed regarding the effect of heat treatment on the spinel phase, which is found to be a mixture of Fe_3O_4 and γ-Fe_2O_3. Unlike the transformation between α and γ phases, the transformation between Fe_3O_4 and γ-Fe_2O_3 are compositional without any structural change, with arbitrarily distributed cation vacancies forming at octohedral sites [55]. As can be observed from Figure 4.6 where all three conditions provided less than 5% α-Fe_2O_3, the amount of γ-Fe_2O_3, with respect to Fe_3O_4, increases with increasing annealing temperatures. Under standard oxidation conditions, the transformation is driven by Fe diffusion to the surface. At low temperatures, there is less energy for Fe diffusion even after long annealing times and the Fe_3O_4 does not undergo conversion. At high temperatures, the γ-Fe_2O_3 phase dominates.

Typically, Fe_3O_4 nanoparticles should oxidize directly to α-Fe_2O_3 around 600 °C [55]. In this case, again the restricted degree of agglomeration stabilizes both of the spinel phases, preventing such transformation. This tunability of the spinel phase offers another opportunity to control the nanoparticle properties.

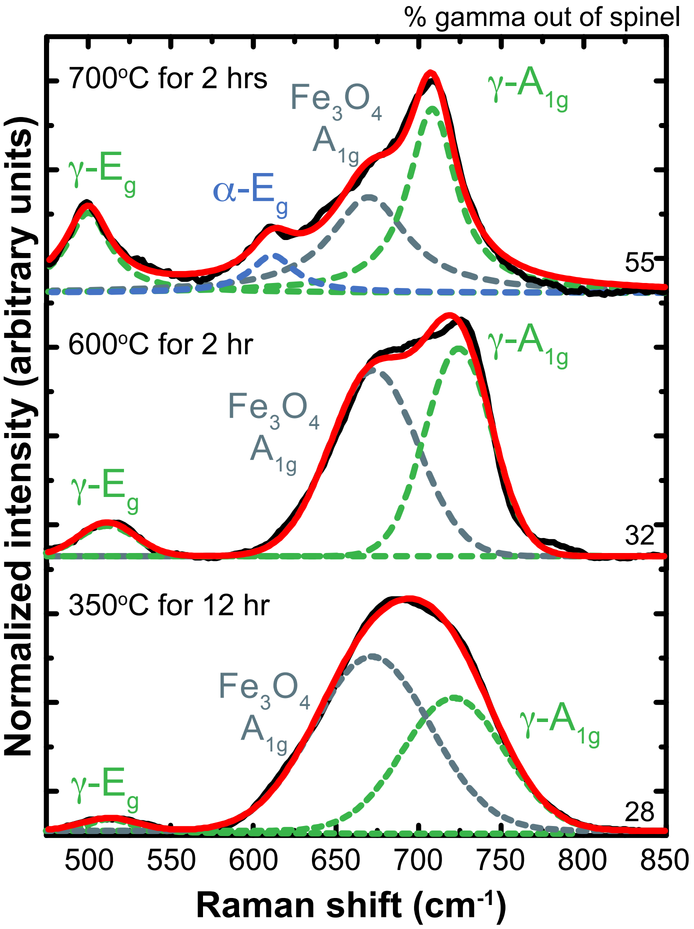

Figure 4.6: Raman spectra of the nanoparticles formed using the polymer with the higher molecular weight annealed at (i) 700°C for 2 hours, (ii) 600°C for 2 hours, and (iii) 350°C for 12 hours under N_2

Tunable Nanoparticle Phases with Raman Spectroscopy used for Semi-Quantitative phase analysis

Through a combination of changing the polymer molecular weight and post-deposition annealing conditions, we are able to modify the relative abundance of the spinel to hexagonal phases from a pure monophase to mixed phases of varying composition back to a pure monophase with the same basic recipe for particle formation. **Figure**

4.7 (a) shows the Raman spectra of nanoparticles produced using PS-*b*-P2VP with higher and lower MW with different post-deposition annealing treatments from (i) to (x). The assignments of visible modes for each phase are provided in **Table 4.2**, with the respective conditions summarized in **Table SI-4** in the supporting information.†

Table 4.2: Table of observed Raman peaks in Figure 4.7

Observed Raman shift (cm^{-1})	Related spectra in Figure 4.7	Assignment	References
214-219	(i), (ii), (iii), (iv), (v), (vi), (viii)	A_{1g} of α-Fe_2O_3	[189, 218]
243	(ii), (iii) , (iv), (vi), (vii)	E_g of α-Fe_2O_3	[189, 218]
277-288	(i), (ii), (iii), (iv), (v), (vi)	E_g of α-Fe_2O_3	[189, 218]
345-385	(vii), (viii), (ix), (x)	T_{2g} of γ-Fe_2O_3	[220]
400-409	(i), (ii) , (iii), (iv), (v), (vi)	E_g of α-Fe_2O_3	[218, 220]
497	(i), (ii) , (iii), (iv), (v)	A_{1g} of α-Fe_2O_3	[218, 220]
495-500	(vii), (viii), (ix)	E_g of γ-Fe_2O_3	[217, 220]
610	(i), (ii) , (iii), (iv), (v), (vi), (vii)	E_g of α-Fe_2O_3	[218, 220]
677	(ii), (iii), (iv), (v), (vi), (vii), (viii), (ix), (x)	A_{1g} of Fe_3O_4	[239]
725	(iii), (iv), (v), (vi), (vii), (viii), (ix), (x)	A_{1g} of γ-Fe_2O_3	[74, 189, 219]

For pure monophase of hexagonal α-Fe_2O_3 nanoparticles, five distinct peaks can be observed, as shown in Figure 4.7(a) (i) where three E_g modes of α-Fe_2O_3 [218,220,221] are visible at 292cm^{-1}, 409cm^{-1} and 610cm^{-1} . The other peaks at 223cm^{-1} and 497cm^{-1} could be assigned to the A_{1g} stretching modes of α-Fe_2O_3 due to the vibrations of Fe and O ions, respectively [218, 221]. On the other hand, for purely spinel phase materials, three characteristics peaks are observed, as in Figure 4.7(x). The broad peak around 700 cm^{-1} can be deconvoluted to give A_{1g} of Fe_3O_4 at 672 cm^{-1}, and the A_{1g} γ-Fe_2O_3 at 721 cm^{-1} . The peak around 335 cm^{-1} can be attributed to either the T_{1g} of γ-Fe_2O_3 (340 cm^{-1}) or the T_{2g} of Fe_3O_4 (330 cm^{-1}) [217]. This suggests that these nanoparticles are purely spinel phase materials.

As the processing parameters are modified, the features associated with γ-Fe_2O_3

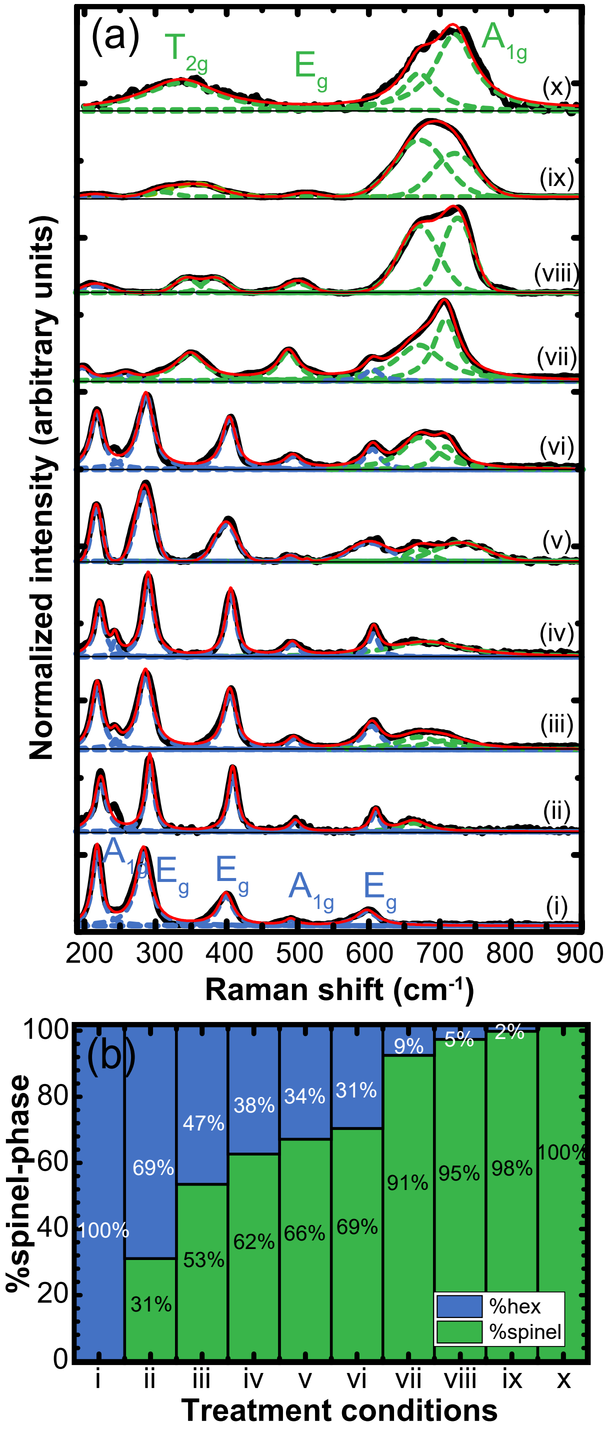

Figure 4.7: (a) Normalized Raman spectra of the iron oxide nanoparticles under various annealing conditions with Lorentzian peaks fitting. (b) Percentage spinel and hexagonal phases determined from the Raman spectra for each treatment condition

and Fe_3O_4 can be enhanced and those with α-Fe_2O_3 diminished, as seen in Figure 4.7 (ii)-(ix). In Figure 4.7(a) (ii)-(x), a feature at around 700cm^{-1} is observed that can be attributed to the spinel phases (A_{1g} of γ-Fe_2O_3 and Fe_3O_4). Though this mode could also be due to the IR active longitudinal optical E_u mode activated by disorder [190, 214, 220], particularly in Figure 4.7(ii), the other changes to the spectrum strongly suggest the emergence of spinel phases with changing conditions, particularly the emergence of a peak at 509cm^{-1} that could be assigned to the E_g mode of γ-Fe_2O_3 for Figure 4.7(a) (vii-ix), which represents the symmetric bands of O with respect to Fe. A shoulder mode at 243cm^{-1} that can be assigned to another E_g of the α-Fe_2O_3 phase also appears in some of the spectra, suggesting that the conditions for each sample set are likely to be slightly different.

As features from both the spinel and hexagonal phases are present in the same spectrum, we can use the intensity area ratio of the A_{1g} peak (~550-800cm^{-1}) of spinel phases (γ-Fe_2O_3 and Fe_3O_4) against the A_{1g} of the hexagonal α-Fe_2O_3 (~150-300cm^{-1}) to make a semi-quantitative estimate of the percentage of each phase, following a modified approach similar to that by Bersani et al. [214] and Choupra et al. [189] (see supporting information Figure SI-1.)†

The area intensity ratio of spinel to hexagonal phase was given by $\Sigma = \frac{I_{A_{1g\ spinel}}}{I_{A_{1g\ hex}}}$.

The percentage of spinel phase was given by % spinel$= 100 * \frac{\Sigma}{\Sigma + 1}$.

As Raman is more sensitive to the α-Fe_2O_3 phase [189, 218, 220], this is probably an underestimation of the amount of spinel present in the samples. Though the Raman analysis was not directly correlated to XRD data (see supporting information Figure SI-2)†, it has been seen to be a useful technique for semi-quantitative analysis of the relative abundance of the three polymorphs in a sample [43, 189, 214]. Figure

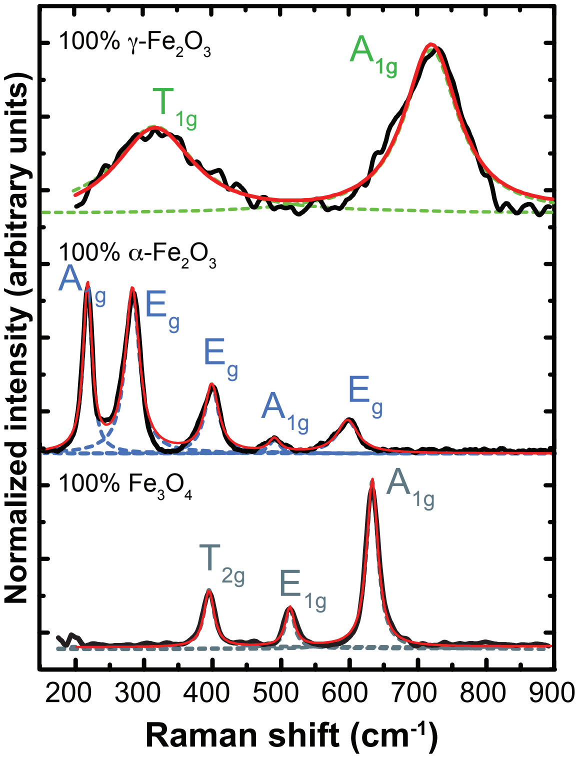

Figure 4.8: Normalized Raman spectra of the iron oxide nanoparticles under various growth conditions with Lorentzian peak fitting. (a) pure γ-Fe_2O_3 formed using higher molecular weight co-polymers (b) pure α-Fe_2O_3 formed using lower molecular weight co-polymers with annealing (c) pure Fe_3O_4 formed using hydrated $FeCl_2$ salts with higher molecular weight co-polymers.

4.7(b) shows the relative weight of spinel (γ-Fe_2O_3 and Fe_3O_4) compared to hexagonal (α-Fe_2O_3) iron oxide.

Through a combination of changing the polymer molecular weight and post-deposition annealing conditions, we are able to modify the relative abundance of the spinel to hexagonal phases from a pure monophase to mixed phases of varying composition back to a pure monophase with the same basic recipe for particle formation. It is even possible using hydrated salts directly to produce pure Fe_3O_4 nanoparticles of similar size, bypassing the γ-Fe_2O_3 formation entirely. **Figure 4.8** shows the pure monophase nanoparticles of all three oxide polymorphs achieved from reverse micelle templating. Taking advantage of the tunability and control over the structure has allowed us to produce nanoparticle arrays suitable for a variety of applications (see supporting information **Figure SI-7**)†. By tuning the annealing conditions, it was possible to achieve coercivity and saturation magnetization values for small nanoparticles (∼6nm) that are usually only obtainable from larger particles (¿25 nm) purely by increasing the percentage of the spinel phase [43]. Synthesized nanoparticles optimized for use in organic solar cells were transfer-printed using graphene onto P3HT:PCBM to control the injection of charge carriers [42]. The high temperature stability of micelle templated nanoparticles was exploited to form a γ-Fe_2O_3 nanoparticle/α-Fe_2O_3 heterojunction electrocatalyst to improve charge separation, yielding higher water splitting efficiency [35].

A deep understanding of the formation and conversion processes allows the reverse micelle templating approach to be effectively utilized to tailor nanoparticles for specific applications. Different applications require properties differing in terms of phase, size and dispersion of the iron oxide nanoparticles. By varying the type of polymer, different properties can be controlled. For instance, α-Fe_2O_3 was predominantly formed using the crew-cut micelles, however the lower MW polymer led to monolayers of reduced order, which can be advantageous in optical scattering applications; on the other hand, magnetic iron oxide phases were dominant while using the dense-core micelles, which yielded nanoparticles of a narrow size-distribution in an ordered array suitable for magnetic optoelectronics. It is important to note thatα-Fe_2O_3 could be formed using dense-core micelles but required additional thermal treatment post-growth, while the crew-cut micelles had a shorter easier route to α-Fe_2O_3 and required a smaller amount of precursor to fully saturate. This contribution can therefore be taken as a roadmap to obtain desired properties by varying parameters to achieve nanoparticles according to the application required.

4.1.3 Conclusion

In this study, we report the manipulation of PS-*b*-P2VP reverse micelle templating to form iron oxide nanoparticles with tunable structure. By modifying both the micelle templates before synthesis and the post-deposition annealing conditions, we can achieve nanoparticles with composition ranging from purely spinel to purely hexagonal phases, independent of particle size. Broadly, reverse micelles formed from diblock copolymers with a higher molecular weight resulted in predominately γ-Fe_2O_3, as the dense dry core shields the infiltrated iron chloride precursor from hydration. On the other hand, the core of the lower molecular weight micelle is highly swollen in solution, and the micelle collapses upon deposition, resulting in predominately α-Fe_2O_3. Dependent on which polymorph is desired, either lower or higher molecular weight polymer offers a facile route to high phase purity. Annealing under various conditions allows formation of phases with mixed composition, with both hexagonal and spinel phases of varying ratios. Raman spectroscopy and QNM analysis allows a full picture of the formation and transformation processes that occur within the reverse micelle templates. By controlling the conditions, it is possible from the same basic process to produce designer iron oxide nanoparticles suitable to applications that exploit the specific properties of the different polymorphs.

4.1.4 Experimental Section

Two polystyrene-*block*-poly(2vinyl pyridine) powders (PS-*b*-P2VP, Polymer Source) of different molecular weight and PS-P2VP ratios were used in this experiment: $\mathrm{M_n}$: 75000-*b*-66500, labeled as higher MW; $\mathrm{M_n}$: 28000-*b*-36000, labeled as lower MW. The polymers were dissolved in o-xylene to produce solutions above the critical micellar concentration, typically above 3 mg/ml [240]. The solutions were magnetically stirred for 24 hours to allow the formation of reverse micelles. Following that, the precursor salt (anhydrous $FeCl_3$, sublimed grade, $\sim$ 99.9%; Sigma Aldrich) was added to the solutions at loading ratios of either 0.2 or 1.5 (the ratio between Fe and units of 2VP of the copolymer). The solution was stirred for a further 24 hours to ensure infiltration of the micelles, followed by centrifuging for 15 min to remove the excess salt. To form the iron oxide nanoparticles, the solution was spin coated or drop casted onto clean substrates and then treated under oxygen plasma (29.6W, 950mTorr, Harrick Plasma Cleaner) to remove the polymeric micelles and convert $FeCl_3$ to iron oxide.

Raman spectroscopy was performed by a Renishaw inVia spectrometer at 514nm laser excitation on drop casted (4μl thrice) samples on freshly cleaved KBr substrates and spin coated (4μl once) samples on Al foil samples. The laser power was set to 1mW and an objective of 20x and 1800 l per mm grating was used. To generate adequate signals for the spectra acquisition, the laser was focused at regions with visible residue ("coffee stain" area on the drop-casted sample, edges of the substrate on the spin-coated samples) where more materials were aggregated. The baseline of the spectra was created and then subtracted to highlight the peaks of interest. In addition, the spectra were smoothed by Savitzky-Golay function in Origin and normalized in the region from 150cm^{-1} to 900cm^{-1}. The spectrum features were deconvoluted using Lorentzian line shape profiles to highlight the iron oxide characteristic peaks.

Quantitative nanomechanical mapping (QNM) atomic force microscopy (AFM) was performed using a Bruker Bioscope Catalyst with an RTESPA probe with spring constant of 26N/m and resonant frequency at 300kHz. To confirm the mechanical properties of the micelles, hardness and Young's modulus maps were generated using the QNM AFM mode provided by the Bruker Nanoscope software. AFM micrographs were analyzed using WSxM 5.0 . The elastic modulus was determined by taking a line profile through 100 micelles by matching the coordinates in the topography channel to the elastic modulus channel. The elastic modulus for each micelle was determined by taking the average of value at the center points of the line profile, correlated to the centre of the micelle in the topography channel. The number of points averaged to determine the modulus varied due to a range in the size of micelles measured. However, typically 10 points were taken. The modulus measurements for each micelle were fit using a Gaussian approximation to calculate the average modulus value and error for each treatment.

To determine the micelle or nanoparticle sizes after deposition, scanning electron microscope (SEM) and AFM measurements were performed. SEM micrographs were obtained with a FEI VERSA 3D using an accelerating voltage of 5kV and a probe current of 12pA. Atomic force microscopy (AFM) micrographs were collected using an Asylum MFP-3D instrument (Oxford Instruments Asylum Research) in the alternating current (AC) mode under ambient environment. AFM probes (Asylum

Research) with spring constant of 26N/m and resonant frequency at 300kHz was engaged in tapping mode for topography scans. To determine the inner core diameter of the micelles, a thin layer of micelles was deposited on porous carbon thin film TEM grids using dip-coating, which allowed direct TEM/STEM characterization of the individual micelles. In order to selectively stain the P2VP cores, the TEM grids coated with micelles were then exposed to I_2 vapor ($\sim$ 99.8%, Sigma-Aldrich) for 3 hours at room temperature, by placing iodine crystals and TEM grids in a sealed glass container [241]. JEOL 2010F TEM imaging was operated at 200kV accelerating voltage with the field emission gun (FEG) source. The hydrodynamic diameter (d_h) was measured with a Zetasizer Nano ZSP (Malvern Instruments) by dynamic light scattering (DLS) of the micelles in toluene as reference solvent (3 mg mL^{-1}). For each measurement 6 runs were performed.

Analysis of the deposited micelle or nanoparticle sizes on TEM, SEM or AFM micrographs used ImageJ. An effective radius of a circular micelle was extracted for each particle. In general, a hundred measurements on different particles within a 2μm x 2μm area were sampled to determine the average radius and error from a histogram of the radii distribution.

All SEM, AFM and QNM samples were prepared by dynamically spin-coating 4μl of solution on to a 1x1 cm^2 Si substrate inside a glovebox at 2000rpm for 45s (Specialty Coating Inc. G3P spin coater).

Supporting Information

Supporting Information is available from the Wiley Online Library or from the author. This hyperlink will take you to the Supporting Information

4.2 Enhanced Photoelectrochemical Water Splitting Efficiency of Hematite (α-Fe_2O_3)-Based Photoelectrode by the Introduction of Maghemite (γ-Fe_2O_3) Nanoparticles

Declaration

Enhanced photoelectrochemical water splitting efficiency of hematite (α-Fe_2O_3)-Based photoelectrode by the introduction of maghemite (γ-Fe_2O_3) nanoparticles (Journal of Photochemistry and Photobiology A: Chemistry, Volume 410, 2021, 113179, ISSN 1010-6030,)

Authors: Tsuyoshi Tokubuchi, Ramis Imran Arbi, Pan Zhenhua, Kenji Katayama, Ayse Turak, Woon Yong Sohn

This manuscript has been published in **Elsevier *Journal of Photochemistry and Photobiology A: Chemistry*** on **1st April 2021** in the cited volume and is available at the following link

https://doi.org/10.1016/j.jphotochem.2021.113179

I am a co-author in this article where reverse micelle templated γ-Fe_2O_3 monolayers were applied on the FTO-hematite interface of a water-splitting photoelectrode for improved charge extraction which was observed to be dependant on the order of the nanoparticle array. I was responsible for the growth, deposition and characterization of the nanoparticles used for this study. Moreover, I was also responsible for confirming the presence of γ-Fe_2O_3 after the solvo-thermal deposition of hematite using Raman spectroscopy, for which a variety of substrates were analyzed before settling on MgO for a featureless background. This involved analysis, fitting and assignment of all the Raman spectra. I also performed the AFM and SEM imaging of the nanoparticle arrays and analyzed the order of dispersion using a Mathematica spatial statistics package, Dislocate. All parts of the manuscript involving the characterization of nanoparticle arrays were written by me. Moreover, I prepared the γ-Fe_2O_3 decorated FTO substrates prior to hematite deposition which was done by our co-authors at Chuo University. The electrical characterization of the devices was also performed at Chuo University.

I have included this article in this thesis because of my role in the fabrication of the nanoparticle decorated electrode. This article illustrates the importance of control over a monolayer of nanoparticles for improved performance and so it is in theme with the rest of the thesis as it involves an application of diblock copolymer templated nanoparticles and the dependance of their performance on the template. This aligns itself with the idea of using designer nanoparticles of tunable phase and dispersion for improved efficiency of opto-electronic devices. This application is one of the many potential avenues that are available using reverse micelle deposition.

4.2.1 Introduction

In 2016, the member countries of United Nations (UN) set the Sustainable Development Goals (SDGs) and one of them was to ensure access to affordable, reliable, sustainable and modern energy for all to prohibit the serious environmental pollution caused by burning of fossil fuels and their complete exhaustion.

In order to achieve this goal, there are many attempts for the development of new alternative energy sources and one of them is to use sunlight for the production of hydrogen gas by splitting water. This idea has been realized since Fujishima and Honda succeeded in demonstrating the light-induced water splitting by building a photo-electrochemical (PEC) cell consisting of a TiO_2 photo-anode and a Pt counter electrode for the first time. [242]

Apart from TiO_2, several kinds of semiconductor materials have been developed to be utilized for the photo-electrode in the PEC cell. [243–254] Especially, hematite (α-Fe_2O_3), one of mineral forms of iron oxide, has been regarded as one of the best materials for the purpose due to its high earth abundance, high photo-stability and low price. [244–254] However, it is imperative that its PEC performance, caused by multiple limiting factors such as poor conductivity [255], short electron-hole lifetime [256–258] and poor charge carrier transfer/transport efficiency [259] [260–262] among others, must be improved for its implementation.

In order to make up for the weak aspects of hematite, various treatments have been applied including surface coating with an overlayer [254], adding a dopant [263] [264] [265], and forming a heterojunction with other semiconductor material [249] [266] [267]. Particularly, it has been regarded that a heterojunction, a heterostructure designed by coupling with a second semiconductor, is one of the best methods to enhance the PEC performance by separating the photoexcited holes and electrons into each layer. [249] [266] [267] For example, WO3/α-Fe_2O_3 films have been studied by many groups as photo-anodes in PEC cells and reported that their water splitting efficiencies are higher than those of bare WO_3 or α-Fe_2O_3, which could be attributed to the high charge separation efficiency. [249] However, it has been also well known that, because of the lattice mismatches of the two different semiconductor materials, the defect states located at the interface between two layers could be generated and act as the recombination centre, which limit efficiency. [268]

One of ways to reduce the interface states is to employ a phase-junction, formed by polymorphs of the semiconductor. In 2008, Can Li and co-workers demonstrated that an anatase/rutile phase-junction of TiO_2 directly contributed to the photo-catalytic activity. [269] In addition, it was reported that the phase junction configuration of TiO_2 could also act as the photo-anode in PEC cell and improve the water splitting efficiency. [270] However, there is a limit to the use to TiO_2 in PEC applications due to its wide band gap (3.2 eV), meaning that it is necessary to employ an alternative material to replace the TiO_2 electrode.

Therefore, to develop a new phase-junction-based photo-anode absorbing visible light, in this study, we fabricated the phase-junction configuration of α/γ-Fe_2O_3. In order to build this configuration, we had to take into account the phase transition temperature of γ-Fe_2O_3. By considering the appropriate alignment of the energy bands of each iron oxide phase and water splitting efficiency, the α-Fe_2O_3 layer must be located at the surface of the film and γ-Fe_2O_3 must be inserted in between the conducting substrate and the α-Fe_2O_3 layer. It means that γ-Fe_2O_3 must be prepared on the conducting layer first and the α-Fe_2O_3 layer must cover this. However, because the phase transition temperature from γ-Fe_2O_3 to α-Fe_2O_3 is lower (450 °C) [271] than the temperature at which α-Fe_2O_3 can be stabilized and shows high efficiency (¿600 °C), it was necessary to suppress the phase transformation of γ-Fe_2O_3 to build this configuration. Thus, in order to attain the goal, we prepared the micelle templated γ-Fe_2O_3 nanoparticles and inserted them under the α-Fe_2O_3 layer in which the phase of γ-Fe_2O_3 could be kept even after the annealing process at 600 °C for 2 h. [43] The phase transformation from γ-Fe_2O_3 to α-Fe_2O_3 requires the restacking of the oxygen layers and the replacement of Fe cations, which could be accomplished by the increase in the particle size. [272] With this method used in the present study, the change of the particle size was suppressed due to the physical separation from the micelle template. With the aid of this method, we successfully confirmed using Raman spectroscopy that γ-Fe_2O_3 still remained after the second annealing process conducted at 650 °C for 30 min and demonstrated the phase-junction configuration of α/γ-Fe_2O_3 was generated, showing a drastic enhancement of the PEC performance. This resulted from the high charge separation efficiency, revealed by investigating the photo-excited charge carrier dynamics using a time-resolved spectroscopic technique and an electro-impedance spectroscopy measurement.

The schematic illustration of the phase-junction configuration and the expected charge carrier dynamics is shown in Fig. 4.9.

4.2.2 Experimental Methods

The hematite layer was deposited by a solution derived method that was described in former studies [253] [263] as illustrated in Fig. 4.10b. Briefly, β-FeOOH was grown on fluorine-doped tin oxide (FTO) substrate (7 Ω/sq, SOLARONIX) in solution consisting of 0.15 M iron (III) chloride hexahydrate ($FeCl_3 \cdot 6\,H_2O$, 99.9 %, Wako) and 1 M sodium nitrate (NaNO3, 99.9 %, Wako), which was conducted at 100 °C for 1 h. After rinsing, in order to convert β-FeOOH into hematite (α-Fe_2O_3), the prepared sample was sintered in an electric furnace at 650 °C for 30 min in Ar gas.

The γ-Fe_2O_3 nanoparticles were synthesized by reverse micelle deposition using the diblock copolymer, polystyrene-b-poly-2-vinylpyridine (Polymer source) as described

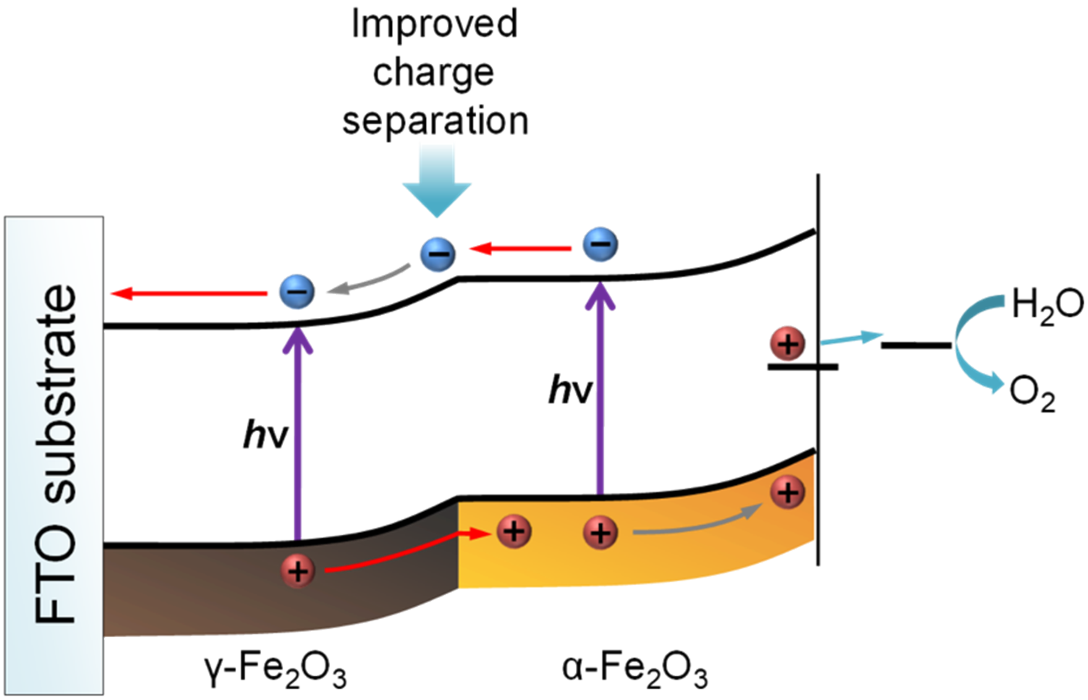

Figure 4.9: Scheme of the charge separation in the phase junction configuration of α/γ-Fe_2O_3
)

previously. [43] (See Fig. 4.10a) In short, $FeCl_3$ was loaded into 3 mg/mL PS-b-P2VP colloidal solution in o-xylene. The solution was then spin-coated onto the FTO substrates and oxygen plasma etched to remove the polymer, leaving behind an array of γ-Fe_2O_3 nanoparticles.

The samples for Raman analysis were prepared by spin-coating a layer of $FeCl_3$-loaded micelles on an MgO single crystal, and, similarly with the FTO samples, using oxygen plasma to form an array of γ-Fe_2O_3. [43]

The as-prepared films with and without the maghemite (γ-Fe_2O_3) particles are denoted as α-Fe_2O_3/γ-Fe_2O_3 and α-Fe_2O_3, respectively. In addition, in the case of α-Fe_2O_3/γ-Fe_2O_3, it was classified into two types, ordered and disordered, based on how they are arranged. The ordering of the monolayer of nanoparticles was controlled by varying the loading ratio of the Fe-salt with the 2 V P units on the di-block copolymer.

The surface morphologies of each sample were examined by scanning electron microscopy (SEM, HITACHI, S-4300). Analysis of the degree of ordering of the nanoparticle films was performed using the disLocate package in Mathematica to extract nearest neighbor spacing, pair correlation function, entropic force map, and order parameters. A detailed description of the package and its capabilities is described elsewhere. [273]

X-ray diffraction (XRD, RIGAKU, Ultima IV) and Raman spectra (Renishaw inVia) were also recorded for the characterization. Raman use 514 nm laser excitation with 1 mW power and 1800 L per mm grating. The spectrum features were deconvoluted using Lorentzian line shape profiles to highlight the characteristic iron oxide peaks. The current densities as a function of the applied bias voltage were measured in KOH aqueous solution (pH = 13.61) with a three-electrode configuration under simulated AM 1.5 G (100 mW/cm^2) illumination by a solar simulator. The as-prepared films were used as the working electrode and a platinum wire and a Ag/AgCl electrode were employed as the counter and reference electrodes, respectively. All the applied potential values (vs. Ag/AgCl), reported in this work, were converted into the corresponding values (vs. RHE) using the Nernst equation:

$$V_{RHE} = V_{Ag/AgCl} + 0.059pH + V^0_{Ag/AgCl}$$

Where $V^0_{Ag/AgCl}$ is the standard potential of the Ag/AgCl reference electrode in sat. KCl (197 mV).

In order to investigate the photo-excited charge carrier kinetics, a heterodyne transient grating (HD-TG) technique which is one of the time-resolved spectroscopic techniques and sensitive to the dipole change at the solid/liquid interface was employed. [258] [274] [275] The third harmonic output of a Nd:YAG (YAG) laser (355 nm, 10 Hz, pulse width: 5 ns) and a semiconductor laser (638 nm) were used as pump and probe lasers, respectively. The grating space used in the present work was 70 μm. The target was excited by the pump irradiation, generating the transient grating on the sample, and the response was measured via the diffraction of the probe light. The signal was detected by a photodiode (Thorlabs, DET110, rise time: 14 ns) and amplified by a voltage amplifier (Femto, DHPVA). To eliminate the scattered pump light entering the detector, a filter for cutting 355 nm and a long pass filter (¿550 nm) were also placed in front of the entrance of the detector. It was monitored and recorded by an oscilloscope (Agilent, DSO8104A, 4GSa/s). In order to measure the HD-TG responses under the bias voltage condition, we built a PEC cell consisting of three electrodes; the hematite film as a working electrode, a Pt counter electrode, and

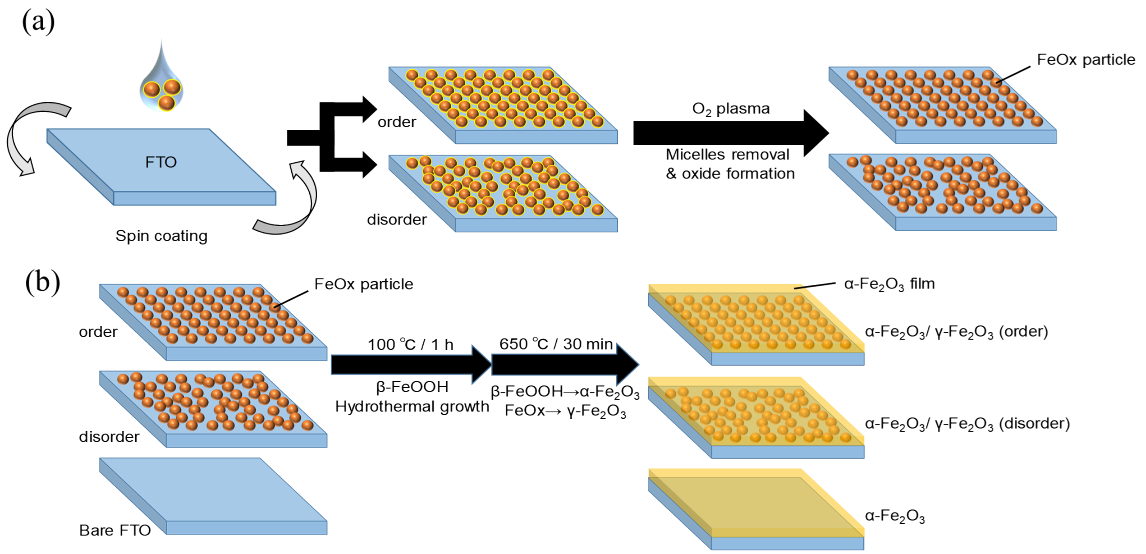

Figure 4.10: Schematic experimental procedure of (a) dispersion of FeOx particle on FTO and (b) hematite deposition

a reference electrode. They were placed into a quartz cell (3/Q/40, Starna Scientific) filled with an electrolyte solution (KOH, pH = 13.61). A potentiostat (HA-151B, Hokuto Denko) was employed to apply a bias voltage.

4.2.3 Results and Discussion

To fabricate the α-Fe_2O_3/γ-Fe_2O_3 film, at first, we prepared the nanoparticles of γ-Fe_2O_3 on the FTO substrate by spin-coating the reverse-micelles. In order to investigate the effect of the ordering of the maghemite particles on the overall PEC performance, we prepared two different types of the samples, ordered and disordered ones, by changing the conditions during deposition. [12] The alignment and ordering of the particles on the FTO substrates by SEM images are shown in Figure S1 in Supplementary Information (SI). Figure S1 in SI shows the top view SEM images which can be classified in relation to their arrangement on the surface. Analysis of the spatial alignment of the ordered and disordered maghemite (γ-Fe$_2$O$_3$) particles shows that the maghemite particles are well aligned in the ordered one, while those in the disordered one are not aligned and aggregated. [12]

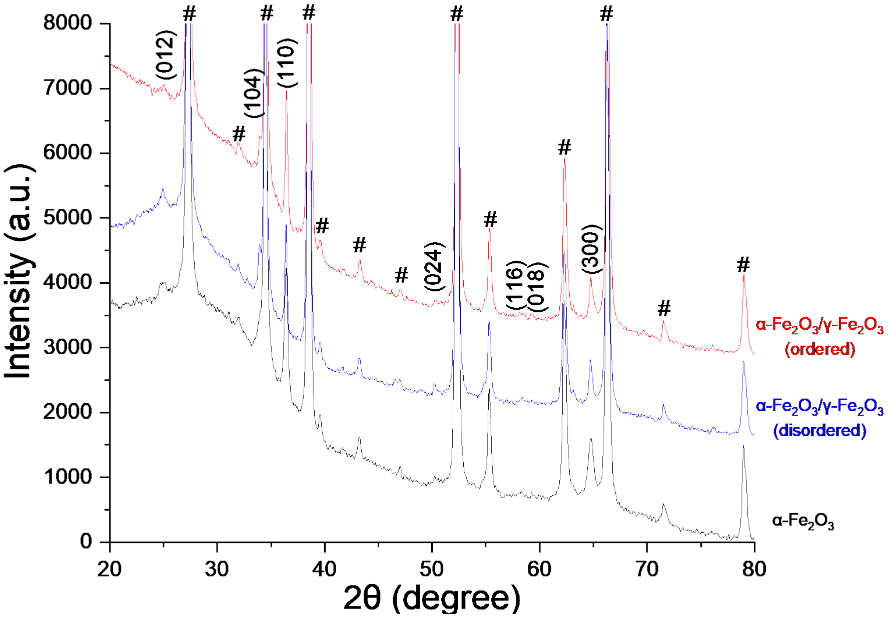

Figure 4.11: X-ray diffraction patterns of α-Fe$_2$O$_3$(black), α-Fe$_2$O$_3$/γ-Fe$_2$O$_3$(disordered)(blue) and α-Fe$_2$O$_3$/γ-Fe$_2$O$_3$(red) films. The hash key indicates the SnO$_2$ of the fluorine-doped tin oxide substrate (ICSD No. 92,55)

To characterize the crystalline structures of the prepared films, the XRD spectra of the α-Fe$_2$O$_3$, α-Fe$_2$O$_3$/γ-Fe$_2$O$_3$(disordered) and α-Fe$_2$O$_3$/γ-Fe$_2$O$_3$ (ordered) films were measured and are presented in Fig. 4.11. All the observed diffraction peaks in the XRD spectra could be assigned to the reference patterns of hematite (ICSD No. 71194) and SnO$_2$ in the FTO substrate (ICSD No. 92552), meaning that α-Fe$_2$O$_3$ was successfully fabricated in all the cases. On the other hand, in both XRD spectra of the α-Fe$_2$O$_3$/γ-Fe$_2$O$_3$ samples (ordered and disordered), we could not find any diffraction peaks originating from maghemite (γ-Fe$_2$O$_3$) due to its small amount in the films.

In order to investigate light absorption properties of the as-prepared samples, UV–vis absorption spectra of bare (α-Fe_2O_3) and α-Fe_2O_3/ γ-Fe_2O_3(ordered) were measured and presented in Figure S2 in SI. As can be seen in the figure, the effect of inserting the maghemite particles on the absorption property of hematite was not observed due to the small amount of the particles.

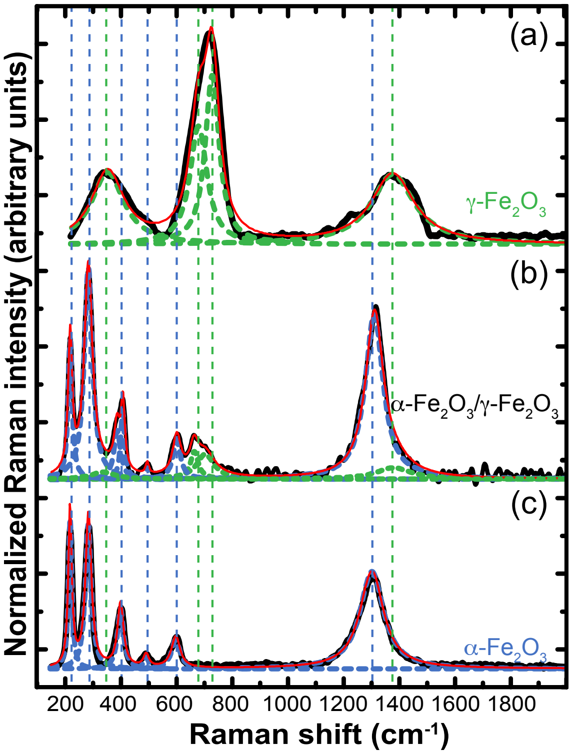

Figure 4.12: Raman spectra of (a) maghemite (γ-Fe_2O_3), (b) α-Fe_2O_3/γ-Fe_2O_3 and (c) hematite (α-Fe_2O_3) with fitting curves.

To confirm the existence of maghemite (γ-Fe_2O_3) before and after the treatment for preparing the α-Fe_2O_3/γ-Fe_2O_3 film, the Raman spectra of the film with the α/γ phase-junction were measured and are presented in Fig. 4.12b. These nanoparticles are known to be stable up to 700 °C (see Figure S3 in SI), which means that this

Table 4.3: List of the observed Raman shifts and the assignments of (a) the mixture of maghemite (γ-Fe_2O_3) and magnetite (Fe_3O_4), (b) α-Fe_2O_3/γ-Fe_2O_3 and (c) hematite (α-Fe_2O_3)

	Observed Raman Shift (cm-1)	Assignment	Ref
(a) 100% gamma/spinel	350	T_{2g} of γ-Fe_2O_3	[276]
	676	A_{1g} of Fe_3O_4	[277]
	727	A_{1g} of γ-Fe_2O_3	[278] [279]
	1377	2Eu of γ-Fe_2O_3	[278] [280]
(b) After deposition on 100% gamma	218	A_{1g} of α-Fe_2O_3	[278] [281]
	283	Eg of α-Fe_2O_3	[278] [281]
	335	T_{2g} of γ-Fe_2O_3	[276]
	386	Eg of α-Fe_2O_3	[276] [279]
	407	Eg of α-Fe_2O_3	[276]
	495	A_{1g} of α-Fe_2O_3	[276] [282]
	600	Eg of α-Fe_2O_3	[276]
	662	A_{1g} of Fe_3O_4	[277]
	701	A_{1g} of γ-Fe_2O_3	[278] [279]
	1310	2Eu of α-Fe_2O_3	[278] [280]
	1380	2Eu of γ-Fe_2O_3	[278] [280]
(c)100% alpha	218	A_{1g} of α-Fe_2O_3	[278] [281]
	283	Eg of α-Fe_2O_3	[278] [281]
	399	Eg of α-Fe_2O_3	[276] [281]
	491	A_{1g} of α-Fe_2O_3	[276] [282]
	597	Eg of α-Fe_2O_3	[276] [281]
	1301	2Eu of α-Fe_2O_3	[278] [280]

method could be employed to suppress the phase transformation of γ-Fe$_2$O$_3$ as expected. In addition, for comparison, the maghemite (γ-Fe$_2$O$_3$) nanoparticles before phasejunction growth and a bare hematite film (α-Fe$_2$O$_3$) are shown in Fig. 4.12a and Fig. 4.12c, respectively. Due to the difference in the crystal structure of γ and α-Fe$_2$O$_3$, each has characteristic Raman features that can be used to identify them. The Raman shifts and their assignments are listed in Table 4.3. Note that the γ-Fe$_2$O$_3$ nanoparticles contain a small amount of Fe$_3$O$_4$, which can also be resolved in the spectra. As can be seen in Fig. 4.12b, all of the expected A$_{1g}$ and Eg peaks, of α-Fe$_2$O$_3$ at 218 cm^{-1} , 283 cm^{-1} , 399 cm^{-1} , 495 cm^{-1} , 600 cm-1 are clearly visible corresponding almost exactly with those of hematite in Fig. 4.12c. Additionally, peaks from the A$_{1g}$ of the spinel phases (γ-Fe$_2$O$_3$ and Fe$_3$O$_4$) at 701 and 662 cm^{-1} are also clearly visible. The T$_{2g}$ of γ-Fe$_2$O$_3$ can also be observed with peak deconvolution at 335 cm^{-1}. The appearance of the peaks corresponding to those of pure hematite (Fig. 4.12c) and those of the nanoparticles before phase-junction formation (Fig. 4.12a) confirms the coexistence of hematite and maghemite in the α-Fe$_2$O$_3$/γ-Fe$_2$O$_3$ films.

Moreover, we were able to confirm that there was an interface generated between the α and γ phases. There is a systematic blue shift of 20 cm^{-1} in the peak positions of the maghemite from before (Fig. 4.12a) to after deposition of the hematite (Fig. 4.12b). Additionally, the peak located around 1320 cm^{-1}, which is shown in the spectrum in Fig. 4.12(b) can be deconvoluted into the 2Eu of α-Fe$_2$O$_3$ and 2A$_{1g}$ of γ-Fe$_2$O$_3$ which both show shifted positions. These can be attributed to interactions between the hematite and maghemite, suggesting an interface between the two phases was formed.

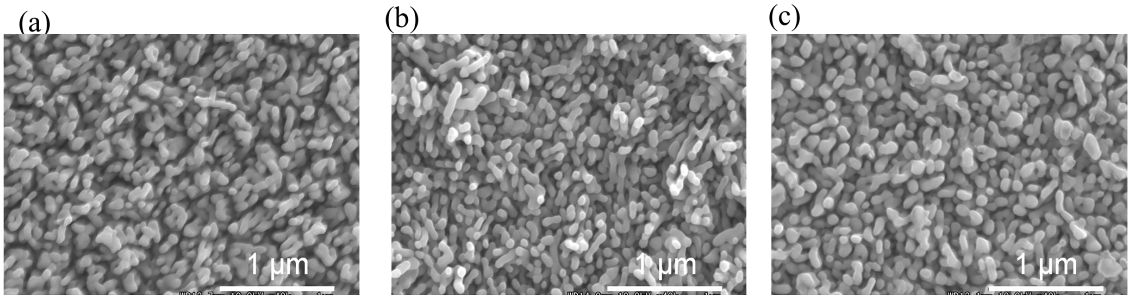

Figure 4.13: SEM images of the as-prepared (a)α-Fe_2O_3, (b) α-Fe_2O_3/γ-Fe_2O_3(disordered) and (c) α-Fe_2O_3/γ-Fe_2O_3(ordered) films

To observe the morphologies of the as-prepared films of α-Fe_2O_3, α-Fe_2O_3/γ-Fe_2O_3(disordered) and α-Fe_2O_3/γ-Fe_2O_3(ordered), the SEM images were taken and are shown in Fig. 4.13a, b and c, respectively. As can be seen in Fig. 4.13, these samples exhibited similar aggregated nanorod shapes. In other words, regardless of the introduction of the maghemite particles, the rod shapes of hematite were similar to each other. In addition, in order to investigate the effect of inserting the maghemite (γ-Fe_2O_3) particles on the thickness of the hematite (α-Fe_2O_3) film, the cross-section view of each film were also examined by SEM and presented in Figures S4 in SI. As can be seen in the figures, the thicknesses of the as-prepared films were also similar to each other, meaning that the effect of the maghemite particles under the hematite layer on the thickness was negligible.

The PEC performances of the as-prepared samples were evaluated by observing the current densities as a function of the applied bias voltage and are presented in Fig. 4.14. The dark current was also measured without light irradiation to confirm the currents observed in this study were photo-generated ones. The photocurrent densities at 1.23 VRHE were 0.74 mA/cm^2 (α-Fe_2O_3/γ-Fe_2O_3(ordered)), 0.33 mA/cm^2 (α-Fe_2O_3/ γ-Fe_2O_3(disordered)) and 0.14 mA/cm^2 (α-Fe_2O_3), respectively. This result clearly

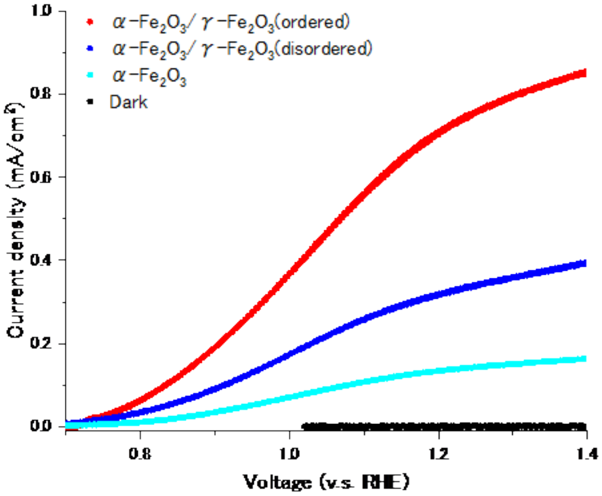

Figure 4.14: Photocurrent density-potential (I-V) curves of α-Fe_2O_3(light blue), α-Fe_2O_3/γ-Fe_2O_3(disordered)(blue), α-Fe_2O_3/γ-Fe_2O_3(ordered)(red) and dark current(black)

shows that, regardless of the alignment of the maghemite (γ-Fe_2O_3) particles, the existence of the maghemite (γ-Fe_2O_3) particles in between the hematite (α-Fe_2O_3) layer and the FTO substrate enhanced the PEC performance, which would be attributed to the improvement of the charge separation efficiency. In addition, it could be also noticed that the alignment of the maghemite (γ-Fe_2O_3) particles influenced the performance. Even though it is still unclear why the current density of the ordered sample was higher than that of the disordered one, we could speculate that the aggregations in the disordered sample could act as recombination centre, resulting in decrease in the efficiency.

In order to verify the stability of the α-Fe_2O_3/γ-Fe_2O_3(ordered) film, we measured the photocurrent density-potential (I–V) curves of the asprepared sample of the ordered α/γ-Fe_2O_3 film for 10 times and revealed that the performance did not decrease under the multiple as presented in Figure S5 in SI, showing the stability of the as-prepared samples.

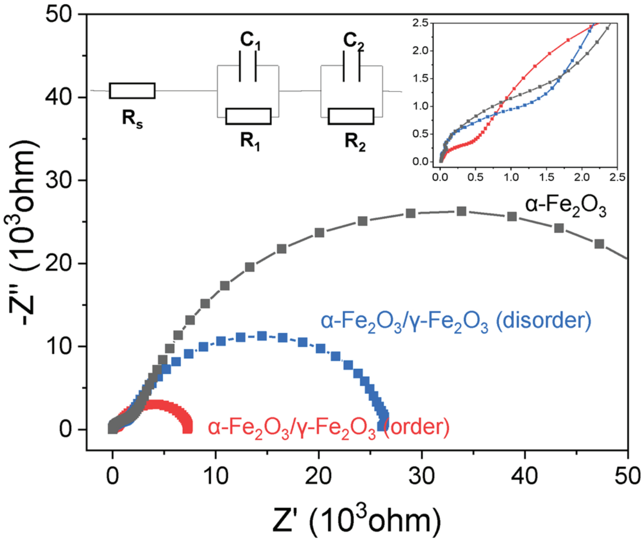

Figure 4.15: Nyquist plots of α-Fe_2O_3, α-Fe_2O_3/γ-Fe_2O_3(disordered) and α-Fe_2O_3/γ-Fe_2O_3(ordered) photoanodes. The inset figures show the Nyquist plots in a lower scale and the equivalent circuit. The Nyquist plots were obtained under simulated solar light (AM 1.5 G) illumination at 0.83 V vs. RHE.

To confirm the operating mechanism of a α/γ-Fe_2O_3 phase junction, the electro-impedance spectroscopy of α-Fe_2O_3, α-Fe_2O_3/γ-Fe_2O_3(disordered) and α-Fe_2O_3/γ-Fe_2O_3(ordered) in a PEC condition are compared in Fig. 4.15. Two semicircles can be distinguished from the Nyquist plots of each sample. The semicircles in the high frequency range and in the low frequency range are attributed to the bulk of semiconductor for electron migration to the back contact and the semiconductor/electrolyte interface for hole transfer, respectively. The Nyquist plots were fitted by an equivalent circuit (inset figure in Fig. 4.15) where Rs, R1, and R2 represent the overall series resistance of the circuit, the charge transfer resistance in the semiconductor and charge transfer resistance across semiconductor/electrolyte interface, respectively. The fitted data of Rs, R1 and R2 are summarized in Table S1 in SI. Both R1 and R2 decreased in the order of α-Fe_2O_3, α-Fe_2O_3/γ-Fe_2O_3(disordered) and α-Fe_2O_3/γ-Fe_2O_3(ordered), indicating that the phase junction effectively facilitated the electron migration across the semiconductor to the back contact and the hole transfer across the semiconductor/electrolyte interface. In our study, the surface kinetics for O_2 evolution was not adjusted, so the facilitated hole transfer across the semiconductor/ electrolyte interface was attributed to a more effective charge separation in the semiconductor. These results match well with our model proposed in Fig. 4.9.

In order to figure out the origin of the performance enhancement more in detail, resulting from the existence of the maghemite (γ-Fe_2O_3) particles, we investigated the photo-excited charge carrier dynamics of the as-prepared hematite films under bias condition (1.0 V vs RHE), ranging from microsecond to second, using the HD-TG method, one of the time-resolved spectroscopic techniques, [258] [259] [262] [263] [274] [275] and the observed responses are shown in Figure S7 in SI. The time constants extracted from the responses are listed in Table S2 in SI. In this time scale, we could observe only one main component in both responses, which has been assigned to the recombination arising from the surface trapped holes. [260] [261] As can be seen in the responses, the decay of the response of the bare hematite (α-Fe_2O_3) film is faster than that of the α-Fe_2O_3/γ-Fe_2O_3 film. In addition, the time constants in Table S1, extracted from each response, shows that the recombination of the surface trapped holes in the α-Fe_2O_3/γ-Fe_2O_3 film is two times slower than that of the α-Fe_2O_3 one, which could be attributed to the retardation of the recombination of the trapped holes at the surface of α-Fe_2O_3, caused by inserting the γ-Fe_2O_3 particles, meaning the photo-excited electrons generated in α-Fe_2O_3 layer were well transferred into the γ-Fe_2O_3 and separated from the surface trapped holes in α-Fe_2O_3 as depicted in Fig.

4.9. It implies that inserting the maghemite (γ-Fe_2O_3) particles played a crucial role in the enhancement of the charge separation efficiency, which is beneficial for the water splitting. The detail of the photo-excited charge carrier dynamics in the α-Fe_2O_3/γ-Fe_2O_3 film will be reported in the near future.

According to the former studies, the band positions of α and γ-Fe_2O_3 are similar to each other. [283] [284] Thus, after constructing the junction between two phases, it is very difficult to predict the band alignment. Unfortunately, because of the small amount of the maghemite particles in this study, it is also very difficult to verify the band alignment. However, based on the results of the time resolved spectroscopy and the electro-impedance spectroscopy, we tentatively propose the type II band alignment for this configuration.

4.2.4 Conclusion

We were able to successfully develop the highly efficient hematite (α-Fe_2O_3) based photo-anode by designing the phase junction configuration with maghemite (γ-Fe_2O_3). We clearly revealed that the enhancement by inserting the maghemite (γ-Fe_2O_3) particles resulted from the well-separated charge carriers between two phases, which was determined by the recombination rate of the surface trapped holes and the decrease in the charge transfer resistances in α/γ-Fe_2O_3 phase junction. We believe that the phase junction configuration, leading to the drastic enhancement of the PEC performance, could be utilized in other semiconductor materials and pave a road for developing new type photo-electrodes for water splitting.

Supporting Information

Supporting Information is available from the Science Direct or from the author.

This hyperlink will take you to the Supporting Information

Chapter 5

Self-assembelled exotic nanoparticles

5.1 Templated redox-active Tin Oxide and Gold nanostructures: A modern approach to Purple of Cassius

5.1.1 Introduction

For over 300 years, a gold-based enamel called 'Purple of Cassius' has been used in colored glasses and ceramics with an instance of the recipe recorded in 1685 by Andreas Cassius [285,286]. From the ruby-purple color in various glassware to varnished earthenware, this material in fact predates Cassius's records. Modern studies of these glasses have shown that the color emerges from nanostructures of gold arrested in glass supports and the original recipe which uses gold salts and tin salts describes a redox reaction which results in reduction of gold and oxidation of tin [285–287]. This age-old recipe describes a spontaneous route for the synthesis of SnO_2-Au composites using two main precursors in a two-step process which can be summarized as follows:

$$3\,SnCl_2 + 2\,HAuCl_4 + 6\,H_2O \longrightarrow 3\,SnO_2 + 2\,Au + 14\,HCl$$

Tin oxide is a stable, wide-bandgap n-type semiconductor that has been actively researched for such applications as transparent conducting oxides, gas sensors, oxidation catalysts or charge transport layers in organic photovoltaics [31, 288–292]. It is particularly interesting because of its high carrier mobility, high visible transmission and oxygen vacancy-dependant conductivity. The adsorption of the negative oxygen species results in a negative surface charge leading to upwards band bending of the n-type SnO_2, leading to a reduced conductivity [288, 292, 293]. Therefore, in reducing gas conditions such as with CO, the oxygen species are used up leading to an increase in conductivity. Conversely, in an oxygen rich environment, further oxygen absorption leads to a decrease in conductivity, allowing it to be used effectively as a sensing material in both oxidizing and reducing conditions [288, 294]. Moreover, SnO_2 nanoparticles have been reported to exhibit oxygen vacancy dependant ferromagnetism [295–297] making them interesting candidates for photonics applications. Optical properties such as refractive indices of circularly polarized light can be controlled using localized magnetic fields giving rise to magnetic circular dichroism [298–304]. For photonics purposes, this can allow for lower signal interference loss due to extinction of back-propagated light in waveguides, potentially allowing them to act as optical isolators.

Combining noble metals like Au, Ag and Pt with SnO_2 to form heterojunctions can reduce the Schottky barrier height allowing for a better conductivity response; as well incorporating the oxidized species of these metals can also act as active sites for oxidative catalysis. This makes composite structures more sensitive for sensing and catalysis [292, 305–309]. The addition of plasmonic coatings can also modify the optical properties, broadening their applicability.

Composites of Au and SnO_2 in particular have been interesting for a variety of reasons, mainly for their catalytic or enhanced gas sensing properties [306, 307, 310–312]. Thin film composite structures have been constructed with Au and SnO_2 for CO gas sensing that exhibited higher sensitivity at lower operating temperatures compared to pristine SnO_2 sensors [310, 311]. These enhanced properties have been attributed to the electronic interface of Au and SnO_2 and the porosity and permeability of the active layer. Additionally, Au, being a better oxygen dissociation catalyst, allows for greater adsorption of oxygen on to the SnO_2 surface where it diffuses to surface vacancies and ionizes. This forms the active sites for target gases (for example CO or ethanol), which react with the adsorbed oxygen. Electronically, the ionization of oxygen on the surface leads to electron depletion which is then returned on oxidation with the target gas. This forms the mechanism of chemo-resistive gas sensors for which SnO_2-Au nanostructures are a candidate. [307, 310–314]

PS-b-P2VP has been used in the past to produce arrays of SnO_2 nanoparticles for increased hole injection in phosphorescent OLED devices [31, 315]. At the same time, there are multiple reports of $HAuCl_4$-loaded PS-b-P2VP to synthesize monolayers of gold [9, 18, 19, 316, 317]. We have also synthesized Au nanoparticles using the polymers and discussed it in terms of Raman as an indicator of loading of micelles with the salt [45]. We have also used the micelles as reactors to make nanoparticles with multiple precursors such as hybrid halide perovskites. [12, 34]

In this report, we use knowledge of the control offered by reverse micelle templating over nanoparticle synthesis to produce multi-component nanostructures; specifically, SnO_2 and Au composite nanoparticles. Using a variety of techniques, we have characterized the nanoparticles, in terms of morphology, arrangement and molecular structure.

5.1.2 Experimental Methods

Reverse micelles were prepared using polystyrene-*block*-poly(2 vinyl pyridine) (PS-*b*-P2VP, Polymer Source) diblock copolymers of weights Mn: 75000-b-66500. The polymer was dissolved in o-xylene in concentrations of 3mg/ml. The solutions were magnetically stirred for at least 24 hours before sample preparation.

The precursor salts, $SnCl_2$ (anhydrous, ≈ 99.99 %) and $HAuCl_4 \cdot 3\,H_2O$ (≈ 99.9 %), were bought from Sigma-Aldrich and stored and handled under N_2 environment inside a glovebox. For the loading of $SnCl_2$, loading ratios of M:2VP (the ratio between the salt ion and number of 2VP units in the solution) of 1:1 or 0.2:1 were used and indicated as such. The solution was allowed to magnetically spin for 48 hours before centrifuging at 6000 rpm for 15 min, the precipitate was discarded and the second precursor was added in volumes ranging from 2μl to 40μl. For the loading of $HAuCl_4$, it was dissolved in 2-butanol in the concentration of 0.5M and then added to the $SnCl_2$-loaded solution.

For polymer removal, the deposited films were exposed to O_2 plasma (29.6W, 950mTorr, Harrick PlasmaCleaner) for 45 min.

Raman samples were prepared using drop-casting of 4μl of the solution for thick layers on aluminum foil. A Renishaw InVia spectrometer was used for all measurements equipped with a 514 nm laser. The laser power was set to 10mW and an objective of 20x (NA=0.40) and 1800l per mm grating was used. The baseline of all spectra was subtracted using Origin and the spectra were smoothed using the Savitzky-Golay function.

Atomic force microscopy (AFM) characterization were carried out using an Asylum MFP-3D instrument in the alternating current mode under ambient environment on spin coated reverse micelles on Si wafers. The AFM images were processed by WSxM. [51] SEM micrographs were obtained with a FEI VERSA 3D using an accelerating voltage of 5kV and a probe current of 12pA. All SEM and AFM samples were prepared by spin-coating 4μl of the loaded solution on cleaned (1cm x 1cm) Silicon substrates.

Magnetization measurements were performed using a liquid Helium cooled Quantum Design Superconducting Quantum Interference Device (SQUID) between an applied field of 5000 Oe and -5000 Oe at 300K. The samples for SQUID were prepared on (40mm x 5mm) Silicon substrates but the solution was spin coated only in a 5mm x 5mm area in the center. The rest of the substrate was masked with Kapton tape during deposition.

X-Ray Photoelectron Spectroscopy (XPS) was performed using Al Kα source with a photon energy of 1486.6eV at a pass energy of 100.00 eV and 25.00 eV for wide range survey scans and high resolution individual core level scans. Sample preparation was the same as SEM and AFM samples and the spectra were analyzed using Thermo Avantage software. Smart background correction was used which is based on Shirley background method and the peaks were fitted with Gaussian-Lorentzian lineshapes.

All spectra were charge-corrected against the 99.4eV peak of Silicon 2p.

UV/Vis absorption measurements were performed using a Cary 6000i UV-Vis spectrometer, using a two-channel liquid cell attachment. Glass cuvettes with a path length of 10 mm were used for both the reference and sample channels, where the reference cuvette was filled with o-xylene and the sample cuvette with loaded polymer which was serially diluted to prevent detector saturation. The measurements were performed for a range of 200 nm to 800 nm under a white light source. Mie scattering simulations were performed using the Nanocomposix Mie scattering calculator tool [318].

Optical transmission on waveguides were performed using sensor chips which were fabricated using the Advanced Micro Foundry (AMF) silicon photonics fabrication process. The chips included 0.22 μm thick x 0.5 μm wide silicon strip waveguides on 2.0 μm of buried oxide on silicon substrates with a Distributed Bragg Reflector grating with sidewall corrugations of 60 nm with a period of 326 nm in a 500 nm wide Si waveguide. The length of the grating and the cavity was 0.5mm and 1.2 mm respectively. A schematic of the waveguide can be observed in Figure 5.6. The design and characterization of the chips have been described by Bonneville et al. [319].

5.1.3 Results and Discussions

Previously, we have reported the synthesis of reverse micelle assisted SnO_2 nanoparticles and their efficacy at increasing hole transport in blue phosphorescent organic light-emitting diodes. [31] We have also reported on the formation of reverse micelle templated Au nanoparticles of controllable size and dispersion and discussed the visibility of the resonance enhanced raman modes of $HAuCl_4$-loaded polymer. [45] In this paper we have merged our ability to make SnO_2 and Au nanoparticles to make self-assembled metal oxide/metal junction in reverse micelle assisted nanoparticles.

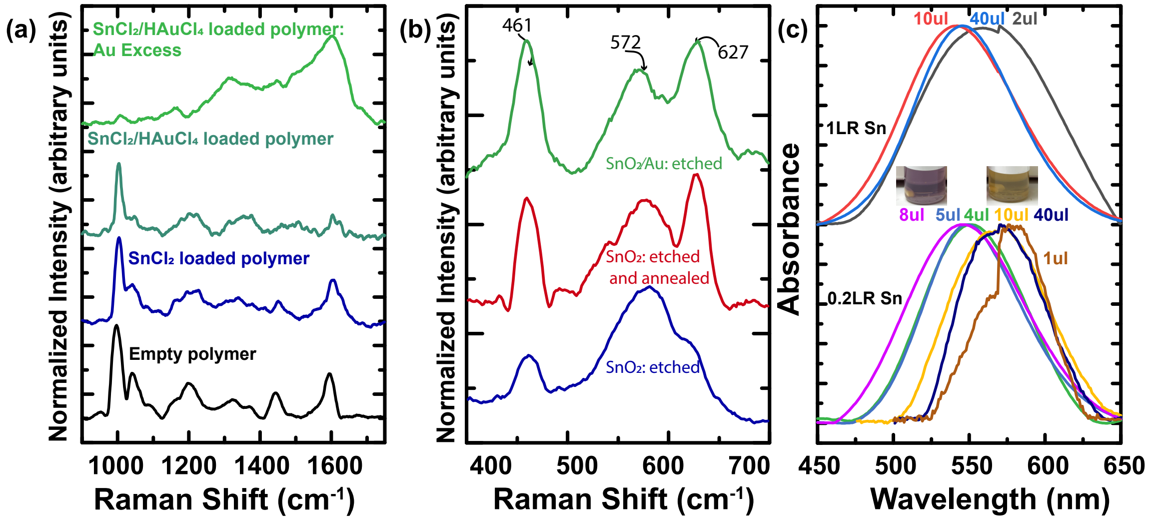

Figure 5.1: (a) Raman spectra of pristine, $SnCl_2$-loaded and $SnCl_2$/$HAuCl_4$-loaded micelles (b) Raman spectra of etched SnO_2, SnO_2/Au and annealed at 300°C under N_2 SnO_2 nanoparticles. (c) UV/Vis spectra of different ratios of SnO_2-Au nanoparticles in solution, showing the SPR peak for Au. The inset shows the solutions of 8ul 0.5M $HAuCl_4$ (purple, left) and 10 ul0.5M $HAuCl_4$

We have used spectroscopic techniques such as UV/visible absorption and Raman scattering for the confirmation of Au and SnO_2 species respectively. Raman spectroscopy is also sensitive to the loading of micelles with transition metal salts and, therefore, can be used to confirm the existence of $HAuCl_4$ in the polymer micelles, due to resonance-enhanced P2VP modes. [45] Figure 5.1 (a) shows the Raman spectra of empty polymer, $SnCl_2$-loaded polymer and $SnCl_{2/}$$HAuCl_4$-loaded polymer. The empty polymer and $SnCl_2$-loaded polymer modes are the same with characteristic modes visible between 1000-1650 cm^{-1}. Additionally, the same relative ratios are observed for the loaded polymer and the empty polymer with the $\nu(1)$ for the PS fraction as the most intense mode centered around 1000 cm^{-1}. The other modes in the region can be assigned to CH in-plane bending (ν(18a) at 1042 cm^{-1}, ν(15) at 1163 cm^{-1}, ν(9a) at 1201 cm^{-1}), backbone twisting modes (γ(CH$_2$) at 1336 cm^{-1}) and ring stretching modes(ν(19) at 1453 cm^{-1}, ν(8b) at 1551 cm^{-1}, ν(8a) at 1606 cm^{-1}). [45, 53]

For the $SnCl_2/HAuCl_4$-loaded polymer, the Raman spectra undergoes a drastic change with increasing amounts of $HAuCl_4$ added. For small amounts of $HAuCl_4$ ($\frac{[Sn^{2+}]}{[Au^{3+}]} < 1.5$), the Raman spectra is consistent with the spectra observed for $SnCl_2$ loaded polymer, with the relative ratios of peaks conserved and peak centers at the aforementioned assignments. Beyond a critical amount of $HAuCl_4$, P2VP modes between 1300 and 1600 cm^{-1} increase in intensity while other peaks disappear. These peaks arise from resonance enhancement of P2VP Raman modes that are coordinated with the transition metal ions, and as reported by Arbi et al in particular for $HAuCl_4$-loaded polymer without $SnCl_2$. [45] This appearance of the resonance enhanced modes of P2VP over other modes of the empty polymer indicates the formation of a complex between the 2VP units and ${AuCl_4}^{-1}$, which suggests the presence of residual ionic Au^{3+} species.

Raman spectroscopy can also be used to confirm the existence of SnO_2. Figure 5.1 (b) shows the Raman spectra of nanoparticles observed after removal of polymer from the loaded micelles. In the conventional formation of SnOx from reverse micelle templating, oxidation of SnOH (which forms from the reaction of $SnCl_2$ and ethanol) by the oxygen plasma leads to the formation of polycrystalline SnO_2 nanoparticles [31]. In Figure 5.1 (b), the A_{1g} and E_g for SnO_2 can be seen around 630 cm^{-1} and 461 cm^{-1} respectively. A broad feature is also observable around 572 cm^{-1} which has been attributed to grain size-dependent surface-phonon modes related to the A_{1g}

mode. [320–325] This broad mode has been attributed to oxygen vacancies on the surface, which reduces with enrichment of oxygen or due to increased volumetric contributions from the stoichiometric SnO_2. [326] With post-etching annealing at 300°C, the 572 cm^{-1} decreases in intensity, suggesting an increase in the grain size of SnO_2 nanostructures and reduction in oxygen vacancies. [305, 320, 324–326], which is supported by EDX measurements showing increased crystallinity of the annealed nanoparticles (see Figure SI-1). The spectra obtained from SnO_2 – Au nanoparticles is similar to the spectra obtained from annealed SnO_2 suggesting that the reaction of $SnCl_2$ and $HAuCl_4$ produces more crystalline stoichiometric SnO_2 nanostructures compared to just $SnCl_2$-loaded polymer.

UV/visible spectroscopy is a useful method for the characterization of Au nanostructures which typically show a surface plasmon resonance (SPR) mode between 500-750 nm [327–329], with its specific peak position dependant on structure, size, chemical environment and refractive index of surrounding media of the Au nanostructures [327–333]. Figure 5.1 (c) shows the absorption spectra of 2 $SnCl_2$ loading ratios with respect to the polymer ($0.2\frac{SnCl_2}{2VP}$ and $1\ \frac{SnCl_2}{2VP}$) with the addition of $HAuCl_4$ precursor to the polymer solution. There are two main observations of interest here. Firstly, the presence of metallic Au nanostructures is confirmed by the presence of an absorbance peak between 500-600 nm and secondly, shifts in the SPR peak maxima can be observed with respect to the volume of $HAuCl_4$ added and the loading ratio of $SnCl_2$. The first observation is useful in confirming the successful reduction of $HAuCl_4$ and therefore, the spontaneous redox reaction between the precursors. An absorbance peak was not observed for $HAuCl_4$-loaded micelles, as in that case polymer removal is required for reduction to metallic Au.

The second observation shows complex behaviour where an absorbance shift to lower wavelength is seen up to a threshold amount of salt addition after which the SPR peak maxima moves in the opposite direction. The trend is the same for both the loading ratios, but interestingly the magnitude of the shift and the threshold amount of $HAuCl_4$ is different for the two loading ratios. For 0.2 loading ratio of $SnCl_2$, with addition of 1 μl of $HAuCl_4$ (0.5M), we observe a peak centered around 570 nm, which blue-shifts to 551 nm for 4ul and 548 nm for 5ul and 545 nm for 8ul. Further addition of $HAuCl_4$ leads to red-shifts to 569 nm with 10ul and 40ul of the precursor. For 1 loading ratio of $SnCl_2$, with the addition of 2ul, a peak can be observed centered around 560 nm, which blue-shifts to 541 nm for 10ul and subsequently, red-shifts to 546 nm for 40ul of $HAuCl_4$ (0.5M) added.

To understand the shifts better, we will discuss the blue-shift and the red-shift separately. According to Mie scattering calculations shown in Figure 5.2, nanoparticles with SnO_2 using a bulk refractive index of 2.2, surrounded by a thin shell of Au would exhibit a blue-shift of the SPR absorbance peak with increasing thickness of the Au shell and constant core size, and a red-shift with increasing SnO_2 core particle sizes for a constant thickness [318]. In the case of pristine Au nanoparticles of similar sizes, increasing the particle size leads to small red-shifts in the absorbance peak centers. [318].

A red shift was observed for the solutions which showed the resonance enhanced Raman features indicating formation of a complex between $HAuCl_4$ and 2VP. This suggest that $HAuCl_4$ is in excess, with residual ionic Au^{3+} species which have not reacted with the $SnCl_2$ to form metallic gold. These solutions are visibly yellow to the naked eye similar to $HAuCl_4$-loaded polymer, despite the SPR absorbance peak

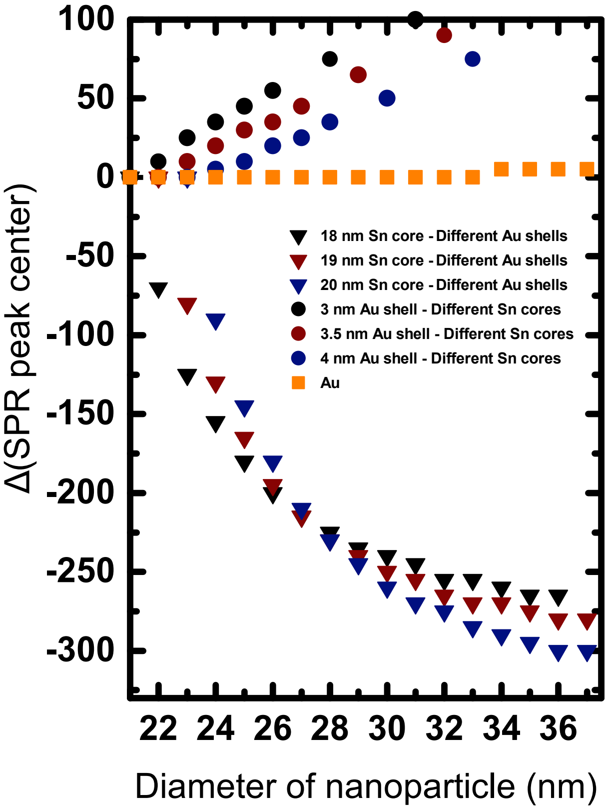

Figure 5.2: Change in the SPR absorbance peak for different sizes of pristine Au, Au core - SnO_2 shell and SnO_2 shell - Au core nanoparticles, simulated using Mie Scattering Theory [318]

observable using a UV/Vis spectrometer. The formation of the $HAuCl_4$/P2VP complex accounts for the color of the solution and possibly the red-shifts in the SPR peak of the Au nanoparticles. Another possibility is that the presence of metallic Au leads to further growth of the Au component, as seeded growth of larger Au nanoparticles by submerging metallic particles in an $HAuCl_4$ solution has been observed previously [334].

On the other hand, for the solutions where Au^{3+} is not in excess, and no enhanced resonance peaks were observed in the Raman spectra, there is a blue shift to lower wavelengths. These solutions are also visibly colored (red to pink) and transparent to the naked eye, which is the typical appearance of solutions containing mono-dispersed colloidal Au nanoparticles [318, 328]. This behaviour is consistent with SnO_2core-Aushell type structures of increasing size, suggesting that with greater amounts of $HAuCl_4$ added to the solution, larger and larger core-shell particles are being formed.

AFM can be used for the imaging of monolayers of nanoparticles and determining their heights after plasma etching of the polymer. Figure 5.3 shows the SnO_2 nanoparticles grown using PS-b-P2VP (loading ratio of 1) which shows a hexagonally packed array of nanoparticles that are $\approx$ 21.95 nm in diameter. This value increases to 26.84 nm with addition of 2ul $HAuCl_4$ (0.5M), 29.82 nm with addition of 8ul $HAuCl_4$ (0.5M) and 31.29 nm with 40ul $HAuCl_4$ (0.5M). Similar patterns of height increase can be observed for the other loading ratio tried, 0.2, for which the values are listed in Table 5.1.

Firstly, the size of the nanoparticles shows the greatest dependance on the amount of $SnCl_2$ loading in the micelles, with the larger loading ratio leading to larger particles. This is consistent with previous reports on PS-b-P2VP templated SnO_2 nanoparticles [169]. Secondly, the nanoparticle size progressively increases with the amount of $HAuCl_4$ introduced. Thirdly, the order of the PS-b-P2VP templated nanoparticles is maintained, that is the resulting nanoparticles are hexagonally distributed with respect to each other (see Figure SI-2).

By loading the $SnCl_2$ and removing the excess precursor salt by centrifuging before the loading of the $HAuCl_4$, the reaction and therefore the nanoparticle growth is localized within the core of the micelles. It should be expected that the loading density of $SnCl_2$ would have a greater influence on the final size of the nanoparticle by

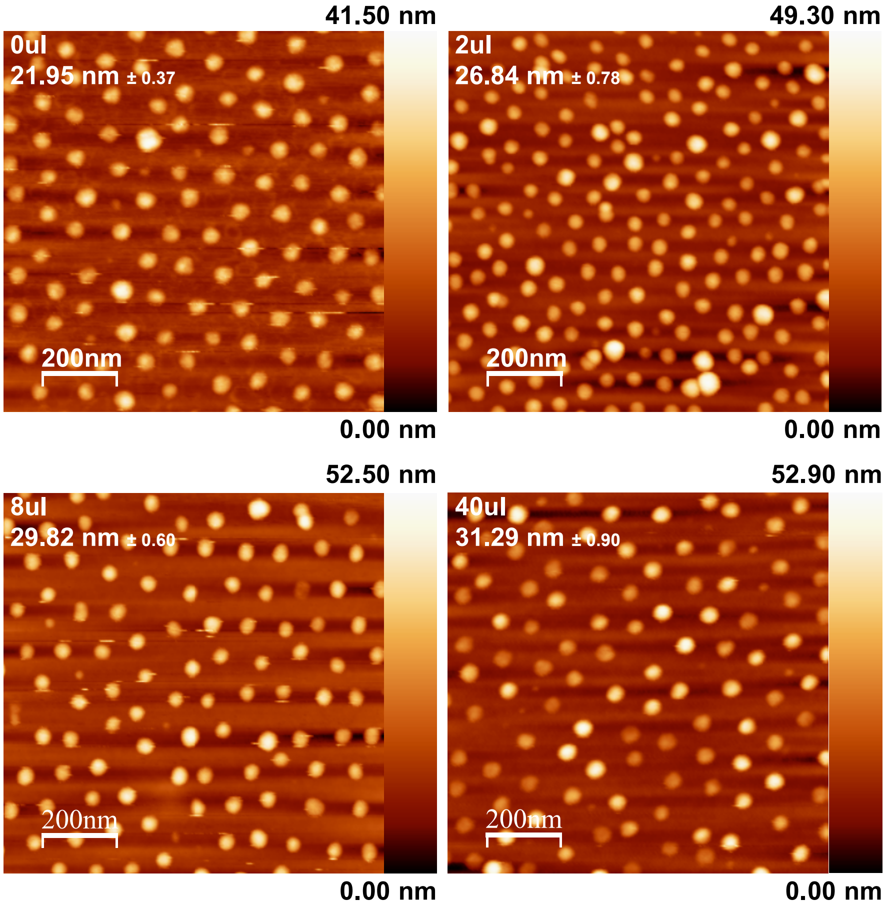

Figure 5.3: AFM images of nanoparticles produced from a polymer loading ratio of 1 of $SnCl_2$ and varying amounts of 0.5M $HAuCl_4$. The molar ratio of Sn and Au and average nanoparticle heights are indicated on the images.

virtue of being the first salt to load and occupy the micellar core. The redox reaction then proceeds within the core as the $HAuCl_4$ infiltrates leading to increase in size. This suggests that further tuning of the nanoparticles, in both deposited arrays and in solution, should be possible using the typically process variables available in micellar templating such as polymer molecular weight, stirring time, solvent and precursor loading ratios.

XPS is useful to identify the chemical species in a monolayer of nanoparticles and

Table 5.1: Table of average heights of Au-decorated SnO_2 nanoaparticles obtained from analysis of AFM images.

$\frac{[SnCl_2]}{[2VP]}$	Volume of 0.5M $HAuCl_4$ (μl)	Size (nm)
1	0	21.95±0.37
	2	26.84±0.78
	8	29.82±0.6
	40	31.29±0.9
0.2	0	15.31±0.21
	2	18.17±0.36
	20	20.43±0.34

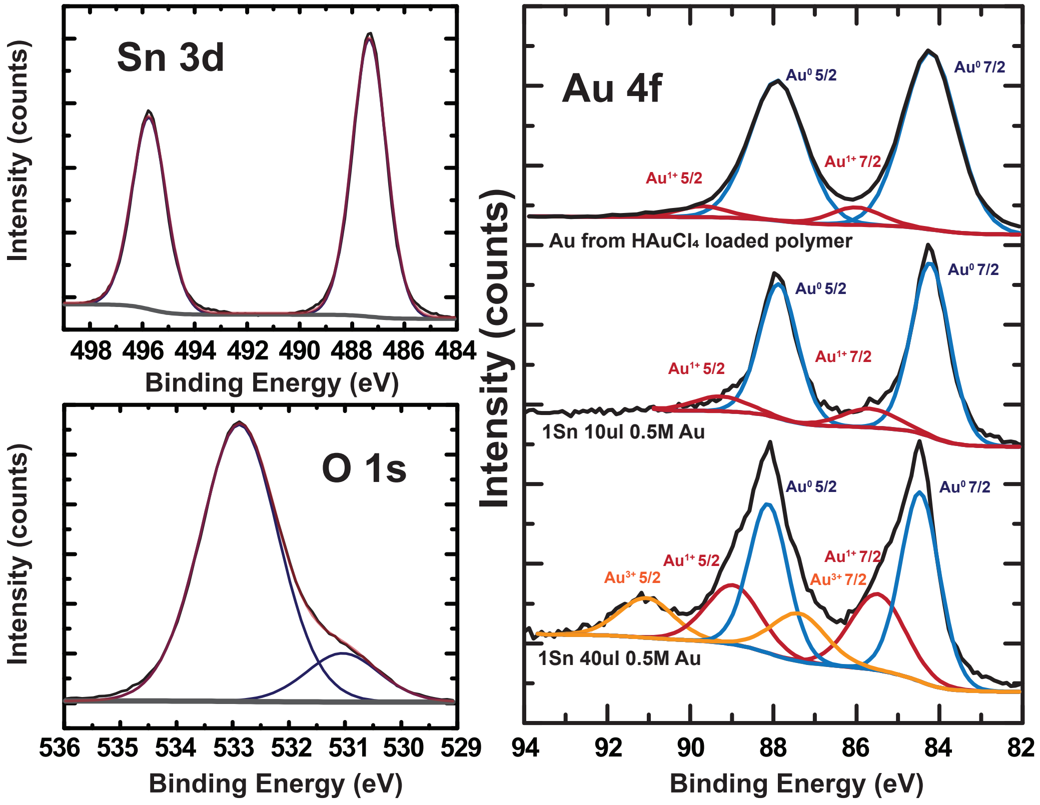

Figure 5.4: High-resolution XPS scans with fitted Gaussian-Lorenzian peaks in the regions of (a) Sn 3d, (b) O 1s and (c) Au 4f.

using silicon substrates, we can correct the spectra for charging and substrate effects using the Si2p core levels. The survey scans in Figure SI-3 show the presence of Au, Sn and O, while the absence of N and Cl peaks confirms the complete removal of polymer and complete conversion of $SnCl_2$ and $HAuCl_4$ respectively. Figure 5.4 (a and b) show the fitted experimental data for 1LR $SnCl_2$ with 10ul of 0.5M $HAuCl_4$) as representative for the entire set, as all other samples show peaks with similar centers as summarized in Table 5.2. By deconvoluting the high-resolution peaks of each element, we can observe peaks emerging from different chemical species. For Sn, the Sn 3d 5/2 level can be fitted with a single peak around 487.3 eV, FWHM of 1.6 and a ΔBE of 8.4 between the doublet peaks. This is consistent with values previously reported for SnO_2 [335–338]. In the O1s region, the core level can be deconvoluted into two peaks. The higher BE peak $\sim$ 533 eV is consistent with reported O1s from native SiO_2 from the silicon substrate [339]. The lower BE O1s peak, shows a center around 531 eV (43.5 eV higher than Sn3d peaks) with a FWHM of 1.6 which is consistent with reported values for oxygen in SnO_2 [336,337,340]. The stoichiometric ratios can be extracted by approximating the equivalent homogenous atomic fraction of oxygen and tin, using the normalized peak area (A/SF) from fitted area (A) and XPS sensitivity factors (SF) [341]. The O/Sn ratio is close to 2 for most of the samples, as expected for SnO_2 and is close to reported literature values of $\sim$1.9 [335]. Similarly, the O1s feature attributed to SiO_2, shows a ratio of $\approx$ 1.5-1.7 which is consistent with reported literature values for SiO_2 [339,340]. One outlier was observed, in the case of 40ul of $HAuCl_4$, where the $\frac{[O]}{[Sn]}$ ratio is significantly larger at 3.58 while the $\frac{[O]}{[Si]}$ is also slightly larger at 1.89. This sample shows an oxygen rich response even though the same preparation and synthesis method was followed for all samples.

The XPS scans of the Au 4f regions, in Figure 5.4 (c), shows a doublet as would be expected for Au 4f 7/2 and 5/2 states for all the samples. The scans in Figure 5.4 (b) contains fitted data for 1LR $SnCl_2$ samples with 10 and 40 ul of $HAuCl_4$ added which is representative of other samples. The fitted data for Au nanoparticles from $HAuCl_4$-loaded polymer is also included. We can clearly see the Au 4f core levels can be deconvoluted into multiple species, dominated by the Au 4f 7/2 centered around 84.2-84.4 eV consistent with metallic Au [340, 342, 343]. A small peak shifted by 1.5-2 eV at around 85.5-85.6 eV is also observed for all samples, which can be assigned to Au^{1+} [316, 317, 338, 343–346]. For higher amount of $HAuCl_4$, where the Raman spectrum showed resonance enhanced peaks, we can also observe additional peaks with a clear mode between 90-92 eV. This corresponds to the expected Au 4f 5/2 doublet of Au^{3+} [316], and the main peak could also be deconvoluted using the corresponding Au 4f 7/2 centred around 87.2 eV, seen in Figure 5.4 (d). However, this additional doublet cannot be seen in the Au nanoparticles from $HAuCl_4$-loaded micelles.

This feature was only seen samples with a high Au:Sn precursor ratio. Though this could be taken as an indication of remnant $HAuCl_4$, no features in the spectrum were observed for Cl or N to indicate unreacted salt or polymer residue. It is likely that this Au^{3+} feature is an indication of higher order oxide of Au, which has been observed previously for Au nanostructures supported on metal oxide supports [316]. The presence of Au^{3+} peaks is also consistent with the appearance of resonance enhanced Raman modes or the red shifts in the UV/Vis absorbance for both loading ratios of Sn. It is possible that the additional peaks are due to the excess $HAuCl_4$

Table 5.2: Table of assigned XPS peaks for all the samples with respect to Loading Ratio of $SnCl_2$ and volume of 0.5M $HAuCl_4$ added.

	Volume of 0.5M	$Au4f_{\frac{7}{2}}$					O1s				
$\frac{[SnCl_2]}{[2VP]}$	$HAuCl_4$ (μl)	Au^0	Au^{1+}	Au^{3+}	$\frac{Au^{1+}}{Au^0}$	$\frac{Au^{3+}}{Au^0}$	(SiO_2)	(SnO_2)	$Sn3d_{\frac{5}{2}}$	$\frac{[O]}{[Sn]}$	$\frac{[O]}{[Si]}$
1	2	84.18	85.54		0.26		532.82	530.96	487.28	1.78	1.59
1	10	84.19	85.66		0.15		532.77	531.01	487.31	1.74	1.60
1	40	84.47	85.54	87.38	0.53	0.32	532.56	531.14	487.53	1.44	1.67
0.2	5	84.67	86.22		0.38		533.04	531.04	487.40	2.17	1.46
0.2	10	84.59	85.97	87.27	0.11	0.46	532.99	531.06	487.32	2.34	1.53
0.2	40	84.58	87.01		0.38		533.08	531.10	487.34	3.58	1.89

in the polymer solution, however, this doublet is not visible in the Au nanoparticles formed from $HAuCl_4$ loaded micelles as can be seen in Figure 5.4 (c).

The presence of oxidized species of Au is also consistent with oxygen plasma treatment of Au nanostructures, which can lead to the formation of oxides [317, 347–349]. It may be possible to eliminate such species with a reductive plasma treatment (such as with H_2 [316,350]); however, such species have been observed to be necessary for oxidative catalysis, such as for CO oxidation [316, 317, 343].

In light of the Raman spectra confirming the presence of SnO_2, UV/Vis supporting the presence of Au nanoparticles and XPS reflecting the presence of gold and tin oxides, we can conclude that SnO_2-Au composite nanoparticles were successfully synthesized. When $HAuCl_4$-loaded or $SnCl_2$-loaded PS-b-P2VP is used to make Au or pristine SnO_2 nanoparticles, respectively, plasma treatment is required post-deposition. This plasma treatment removes the polymer and subsequently converts the salt to its metallic or oxide form. Depending on the plasma used, especially oxygen, oxidized Au species can be present while hydrogen plasma completely reduces the nanoparticle array to Au^0. [316, 350]. In the case of pristine SnO_2 nanoparticles, $SnCl_2$ reacts with added alcohol or water to form SnOH which is subsequently converted to SnO_2 upon oxygen plasma treatment. [31] The important thing of note here is the need for plasma and polymer removal for nanoparticle formation reactions to proceed. On the other hand in the case of the Au-decorated SnO_2, the $SnCl_2$ serves as the active site for the redox reaction with $HAuCl_4$ in the presence of IPA, therefore, SnO_2 and Au respectively form within the micelle core and are not dependant on the post-deposition oxygen plasma treatment or polymer removal for formation. This is a success of this technique allowing for either depositable self-assembled films of tunable size and periodicity or monodispersed nanoparticles enveloped in polymer and suspended in solution.

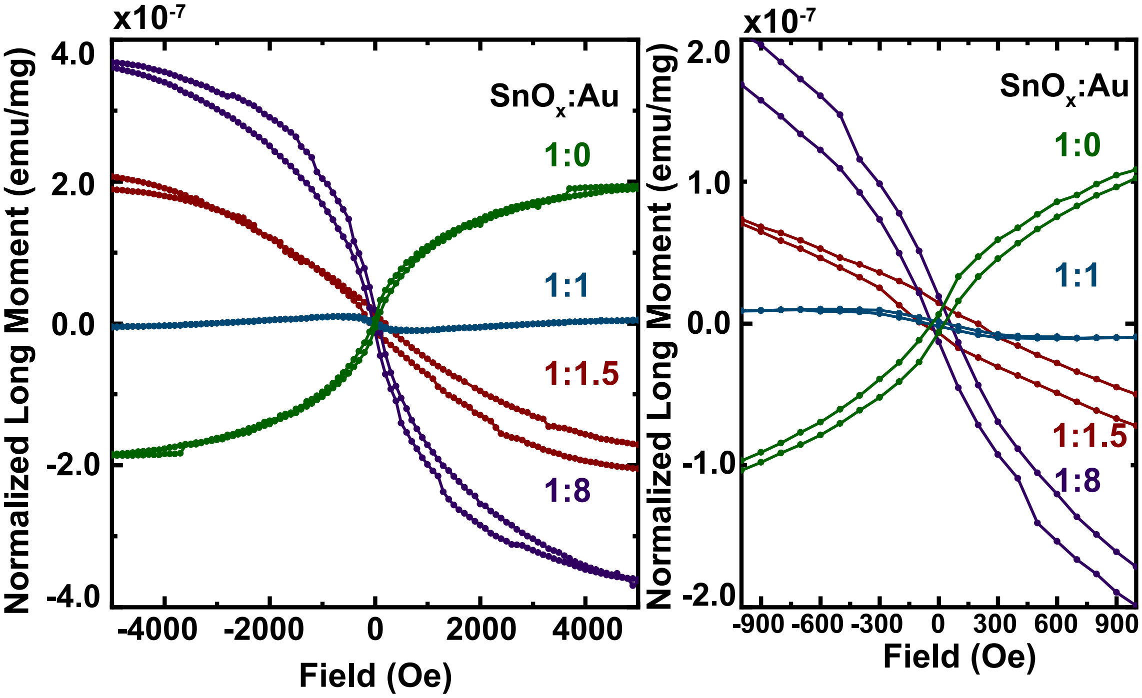

Figure 5.5: Applied field magnetization curves of monolayers of different ratios of SnO_2−Au nanoparticles. The $SnCl_2$-loading in all cases was a ratio of 0.2 Sn:2VP.

These composite nanoparticles were also found to have some interesting magneto-optic properties, that introduces wider applications of such structures. Pristine SnO_2

nanoparticles without annealing synthesized using PS-b-P2VP have shown room temperature ferromagnetism [315], most likely stemming from the oxygen vacancy dependant ferromagnetism reported previously in SnO_2 nanoparticles produced by other methods [295]. The magnetization curves under an applied field using SQUID for monolayers of pure SnO_2 and SnO_2-Au nanoparticles can be seen in Figure 5.5. With increasing Au content, a trend towards increased diamagnetism can be observed. This is consistent with reports in literature on increased diamagnetism of Au nanostructures with increasing size [351, 352] and a complex reduced magnetization response in core-shell structures with Fe_2O_3 cores due to increasing thickness of Au shell. [303, 353, 354]. As the composite particles also increased in size with greater addition of gold salts, we can attribute the increasingly diamagnetic response of the SnO_2-Au in terms of the increasing amount of Au in the nanoparticles. This is also consistent with the increasing intensity of the Au core level peaks relative to the Si substrate signal.

There is a degree of tunability of the magnetic response of a thin film of nanoparticles, offered by the reverse micelle templating route to making composite nanoparticles. With increasing amounts of $HAuCl_4$ added to the solution, the nanoparticle magnetization can be taken from weakly ferromagnetic to diamagnetic.

To take advantage of the interesting magneto-optical effects occurring in these composite particles, we incorporated a film of SnO_2-Au nanoparticles (LR0.2/2ul 0.5M Au) on silicon waveguides with Distributed Bragg Rreflector grating, shown schematically in Figure 5.6. The transmission spectra and the schematic of the entire experimental set-up can be seen in Figure 5.6. The spectra shows the fiber-to-fiber loss (without the waveguide). Including an empty air-cladded waveguide results in a

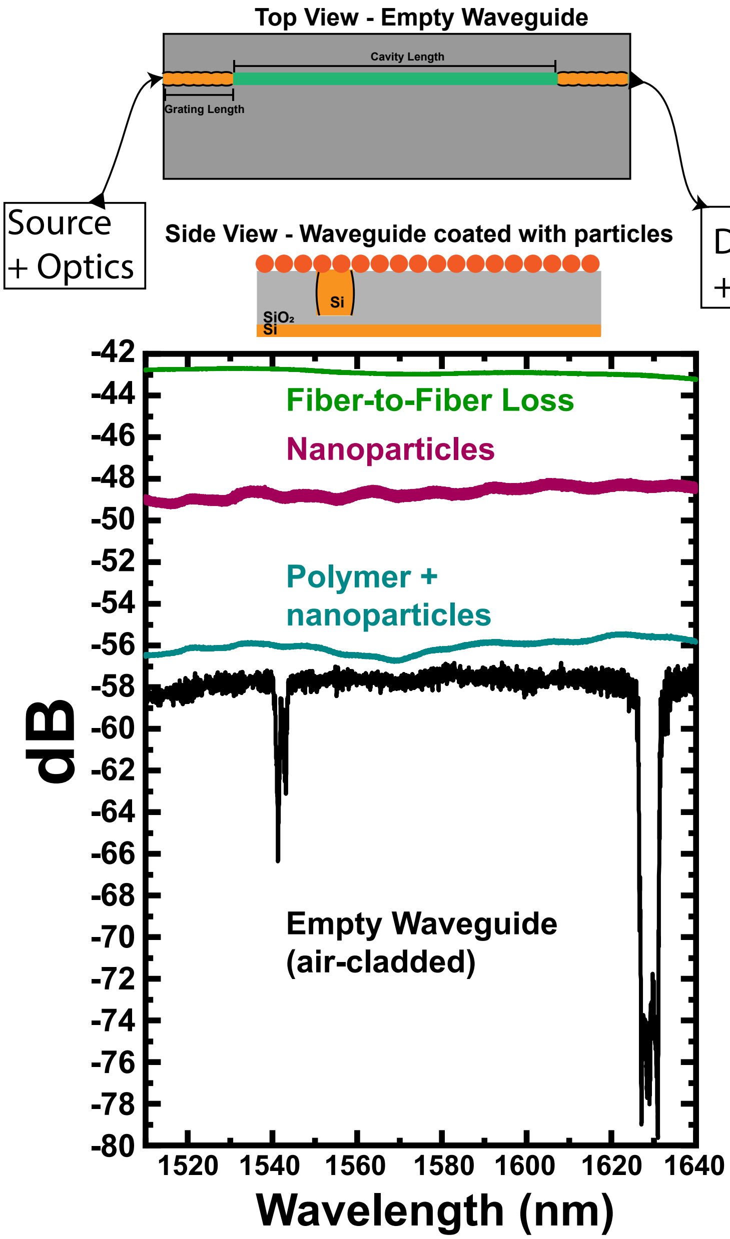

Figure 5.6: (a) Schematic of the experimental setup used for the measurement of the waveguide transmission. (b) Comparison of transmission spectra of air-cladded (empty) waveguides with and without loaded micelles and nanoparticles. The fiber-to-fiber loss is also plotted on the same spectra.

significant increase in the transmission loss, with the emergence of resonance modes clearly visible around 1540 and 1630 nm. With the addition of a polymer or nanoparticle loading, a significant decrease in the overall transmission loss was observed. Additionally, a small localized increase in loss around 1570 nm can be observed, which suggests a shift in the resonance mode around 1540 nm. Though this feature is not very pronounced, its emergence suggests a potential to utilize the nanoparticles for optical bio-sensors, while tracking shifts in resonance modes which can be used to evaluate interaction of biomolecules like proteins [319]. Overall, the incorporation of these composite nanoparticles shows promise for photonics applications, with the potential of these monolayers as cladding layers to reduced overall transmission loss in waveguides, or with further optimization, as optical bio-sensors.

5.1.4 Conclusion

In this paper, we have described a method to synthesize nanoparticles with controllable magnetic and plasmonic properties, which can be deposited using cheap solution processing methods. We have also used the nanoparticles on waveguides to assess their photonic potential.

In light of the Raman spectra confirming the presence of SnO_2, UV/Vis supporting the presence of Au nanoparticles and XPS reflecting the presence of gold and tin oxides, we can conclude that SnO_2-Au composite nanoparticles were successfully synthesized. Additionally, with the help of the periodic AFM we can also resolve the change in size of the nanoparticles and the effect of precursors on the order of the thin film. We have discussed the correlation of excess Au^{3+} ions and the appearance of features using various characterization methods, which also opens the aspect of tunability in terms of size and chemical species (that is, the presence of oxidized Au). When $HAuCl_4$-loaded PS-b-P2VP is typically used to make Au nanoparticles, plasma treatment is required post-deposition. This plasma treatment removes the polymer and subsequently reduces the salt to its metallic form. This limits the use of such particles to applications that require the decoration of surfaces. This new approach bypasses the requirement for the plasma with the reduction of the $HAuCl_4$ in the presence of $SnCl_2$, which results in the formation of metallic gold in the polymer micelles in solution. This speaks to the benefit of reverse micelle templating for self-assembly and control of monolayers of nanoparticles which can be easily deposited (spin-coating, spray-coating or dipping). This is a success of this technique allowing for either depositable self-assembled films of tunable size and periodicity or monodispersed nanoparticles enveloped in polymer and suspended in solution. The benefits of these structures extend beyond SnO_2 to other metal oxides (like TiO_2) with Au and other noble metals (like Pt, Ag), and this technique offers a controllable way of synthesizing and characterizing them. Combined with the tunability of the optical and magnetic properties by changing various deposition parameters provides a powerful system for a wide range of possible applications.

Chapter 6

Conclusion

With this thesis, I have attempted to address and bring together solutions in the use of PS-b-P2VP reverse micelles in the formation of different nanoparticles. This work aims to make the application of these nanoparticles more accessible for devices. The merits of this technique have been discussed in terms of the control over nanoparticle size and dispersion. The insulating polymer layer presents an obstacle in the use of the nanoparticles and for that, I have discussed the efficiency of polymer removal treatments like gas plasmas and UV/Ozone treatments.

I have also discussed enhanced vibrational spectroscopy for the characterization of a monolayer of the reverse micelles and the visibility of the loading of transition metal salts in to the micelle core due to Resonance enhancement of Raman modes of the polymer. This provided us a deeper understanding of the mechanism of transition salt loading and a method to track the process at different points. In this way, PS-b-P2VP is an effective fabrication method of self-assembled nanoparticle arrays.

Iron oxide nanoparticles from $FeCl_3$-loaded PS-b-P2VP micelles is a good model system to assess the flexibility of this technique; the different polymorphs of iron oxide are Raman visible and $FeCl_3$ loaded polymer shows resonance enhanced Raman modes of P2VP. Using different polymers and different post-etching treatments, mixed compositions of α-Fe_2O_3 and γ-Fe_2O_3 nanoparticles with control over the phase fraction. The control over different properties of nanoparticles offered by PS-b-P2VP reverse micelle templating is seen. Utilizing our control over nanoparticle phase and dispersion of arrays, we used pure γ-Fe_2O_3 nanoparticles in α-Fe_2O_3-based photoanode for water-splitting. We showed increased efficiency of the photoanode with the inclusion of γ-Fe_2O_3 nanoparticles. We also observed a higher efficiency for ordered nanoparticles than disordered arrays as evidence for the importance of nanoparticle dispersion on device performance.

Lastly, I extended the role of PS-b-P2VP by using them as nanoreactors for the spontaneous redox reaction of $HAuCl_4$ and $SnCl_2$ for the production of $SnO_{2/}Au$ composite nanoparticles. This is different from how we used it earlier to sequester precursor salts due to the affinity of the 2VP groups and the transition metal ions. I used a variety of characterization techniques to observe reactants and the products. Composites of SnO_2 and Au are desirable for gas-sensing and oxidative catalysis, and this method is a viable method of producing ordered thin films of nanoparticles targeting these applications. I also reported on a tunable magnetic response of these thin films from paramagnetic to increasing diamagnetism with the addition of $HAuCl_4$. Using a variety of characterization methods, I have shown the ability to control the nanostructures in size and composition for a composite system as evidence of the flexibility of PS-b-P2VP reverse micelle templating.

In this piece of work, I have formed a deeper understanding of the salt incorporation mechanism and focused on Fe_2O_3 and $SnO_{2/}Au$ nanoparticles to show the merits of PS-b-P2VP reverse micelles as a method of growing designer nanoparticle arrays. I aim for this thesis to outline a map for the use of PS-b-P2VP reverse micelles for various metal, metal oxide and dielectric nanoparticle arrays which can be controlled in size and dispersion.

6.1 Road Ahead

The road ahead can be broken down into three main areas of interest; The nanoparticles, the polymer and applications.

Firstly, I have discussed the synthesis of Al_2O_3, Fe_2O_3, CuO, Al_2O_3, Au, ZnO and SnO_2 but the same technique can be extended to a variety of other salts such as Pt, Pd, Ag, TiO_2, NiO, WO_3 and MnO, each of which are desirable for their optical, electrical and chemical properties. The progress of the synthesis of each of them can be tracked using the Raman methods described and in this way, the study of the tunability of Fe_2O_3 can be used as an analogue for the other salts as well. Moreover, I have also shown the use of PS-b-P2VP micelles for multi-component nanoparticles, in this case $SnO_{2/}$Au and in other publications halide hybrid perovskites. In that regard, PS-b-P2VP can be used to synthesize structures using multiple salts which are typically difficult to control using other techniques. The method described for $SnO_{2/}$Au can be extended to include other semi-conducting metal oxides and noble metals such as TiO_2 or ZnO with Pt or Ag. Using this method allows us to control the composition uniformly across all the nanoparticles in the solution.

Secondly, I have discussed the role of order of nanoparticle arrays as a factor of thin film performance and we observed an increased performance from not only the inclusion of γ-Fe_2O_3 at the FTO/hematite interface in a photoanode for water-splitting but also increased periodicity of nanoparticles. It would be pertinent to conduct a more comprehensive study of the self-assembly parameters such as dispersion and size as a factor of polymer and salt concentration, additive solvents and post-deposition treatments. I have used two different types of reverse micelles (dense core and crew cut) and it would be interesting to extend this model to other weights of PS-b-P2VP copolymers for the synthesis of larger or smaller nanoparticles. The techniques described and $FeCl_3$ can be used to assess the quality of nanoparticles synthesized, utilizing the understanding of the growth of Fe_2O_3 that I have grown in Chapter 3 and 4. The dependance of the thin-film thickness and order of arrays can be studied in terms of deposition method. In this work, I have focused on using spin-coating and drop-casting, but similar results are possible using dip-coating, blade-coating or electro-spraying. All of these are feasible methods for thin-film devices.

Thirdly, the different nanoparticles can be used in optical or electrical devices. SnO_2 and $SnO_{2/}$Au nanoparticles should be tested for their gas sensing properties which can be done using resistivity measurements under flowing gas. For this purpose, thicker layers of nanoparticles would be preferred because we need flowing current between the nanoparticles as the figure of merit. The other nanoparticles synthesized should be used in OPVs at different interfaces. For layers that are sensitive to plasma treatments, nanoparticles can be deposited using transfer printing methods utilizing sacrificial substrates. Using the charge transport properties, the power conversion efficiency of OPVs should increase.

References

[1] Marek Grzelczak, Jan Vermant, Eric M. Furst, and Luis M. Liz-Marzán. Directed self-assembly of nanoparticles. *ACS Nano*, 4(7):3591–3605, 2010. PMID: 20568710.

[2] Hongbo Feng, Xinyi Lu, Weiyu Wang, Nam Goo Kang, and Jimmy W. Mays. Block copolymers: Synthesis, self-assembly, and applications. *Polymers*, 2017.

[3] Kayori Iyama and Takuhei Nose. Kinetics of Micelle Formation with Change of Micelle Shape in a Dilute Solution of Diblock Copolymers. *Macromolecules*, 31(21):7356–7364, October 1998.

[4] Luciana Meli, Jessica M. Santiago, and Timothy P. Lodge. Path-Dependent Morphology and Relaxation Kinetics of Highly Amphiphilic Diblock Copolymer Micelles in Ionic Liquids. *Macromolecules*, 43(4):2018–2027, February 2010.

[5] Lifeng Zhang and Adi Eisenberg. Multiple morphologies and characteristics of "Crew-Cut" micelle-like aggregates of polystyrene-b-poly(acrylic acid) diblock copolymers in aqueous solutions. *J. Am. Chem. Soc.*, 118(13):3168–3181, 1996.

[6] Shang-Pin Wen and Lee A. Fielding. Pyridine-functional diblock copolymer nanoparticles synthesized via RAFT-mediated polymerization-induced self-assembly: effect of solution pH. *Soft Matter*, 18(7):1385–1394, 2022. Publisher: Royal Society of Chemistry.

[7] Se Gyu Jang, Anzar Khan, Craig J. Hawker, and Edward J. Kramer. Morphology Evolution of PS-b-P2VP Diblock Copolymers via Supramolecular Assembly of Hydroxylated Gold Nanoparticles. *Macromolecules*, 45(3):1553–1561, February 2012. Publisher: American Chemical Society.

[8] Joachim P. Spatz, Stefan Mössmer, Christoph Hartmann, Martin Möller, Thomas Herzog, Michael Krieger, Hans-Gerd Boyen, Paul Ziemann, and Bernd Kabius. Ordered Deposition of Inorganic Clusters from Micellar Block Copolymer Films. *Langmuir*, 16(2):407–415, January 2000. Publisher: American Chemical Society.

[9] Sivashankar Krishnamoorthy, Raphaël Pugin, Jürgen Brugger, Harry Heinzelmann, and Christian Hinderling. Tuning the dimensions and periodicities of nanostructures starting from the same polystyrene-block-poly(2-vinylpyridine) diblock copolymer. *Advanced Functional Materials*, 2006.

[10] Yoon-Hee Cho, Jung-Eun Yang, and Jae-Suk Lee. Size control of polymeric nanoparticles from polystyrene-b-poly(2-vinylpyridine). *Materials Science and Engineering: C*, 24(1–2):293–295, 2004.

[11] G. Kastle, H.-G. Boyen, F. Weigl, G. Lengl, T. Herzog, P. Ziemann, S. Riethmuller, O. Mayer, C. Hartmann, J.P. Spatz, M. Moller, M. Ozawa, F. Banhart,

M.G. Garnier, and P. Oelhafen. Micellar Nanoreactors—Preparation and Characterization of Hexagonally Ordered Arrays of Metallic Nanodots. *Adv. Funct. Mater.*, 13(11):853–861, November 2003.

[12] LS Hui, C Beswick, A Getachew, H Heilbrunner, K Liang, G Hanta, R Arbi, M Munir, H Dawood, N Isik Goktas, et al. Reverse micelle templating route to ordered monodispersed spherical organo-lead halide perovskite nanoparticles for light emission. *ACS Applied Nano Materials*, 2(7):4121–4132, 2019.

[13] Limin Qi. Synthesis of inorganic nanostructures in reverse micelles. In P. Somasundaran and A. Hubbard, editors, *Encyclopedia of Surface and Colloid Science*, pages 6183–6207. Taylor & Francis, London, second edition, 2006.

[14] Ayse Turak. Reverse micelles as a universal route to solution processed nanoparticles for optical, optoelectronic and photonic applications: A story of salt complexation, micellar stability, and nanoparticle spatial distribution. *Vid. Proc. Adv. Mater.*, 2:2103166, 2021.

[15] Muhammad Munir, Ramis Arbi, Pedro Oliveria, Lok Shu Hui, Matt Bumstead, Greg Hanta, Kunyu Liang, Amr Ibrahim, HyeongHwa Yu, and Ayse Turak. Photonics made to order: reverse micelle templating as a universal approach to functional nanoparticles. In *2021 Photonics North (PN)*, pages 1–2, May 2021. ISSN: 2693-8316.

[16] Masato Aizawa and Jillian M. Buriak. Block copolymer templated chemistry for the formation of metallic nanoparticle arrays on semiconductor surfaces. *Chemistry of Materials*, 19(21):5090–5101, 2007.

[17] Ramis Arbi, Amr Ibrahim, Liora Goldring-Vandergeest, Kunyu Liang, Greg Hanta, Lok Shu Hui, and Ayse Turak. Role of hydration and micellar shielding in tuning the structure of single crystalline iron oxide nanoparticles for designer applications. *Nano Select*, 2021.

[18] Vignesh Suresh, Meiyu Stella Huang, M.P. Srinivasan, and Sivashankar Krishnamoorthy. In situ synthesis of high density sub-50 nm zno nanopatterned arrays using diblock copolymer templates. *ACS Applied Materials & Interfaces*, 5(12):5727–5732, 2013. PMID: 23675650.

[19] Sivashankar Krishnamoorthy, Raphael Pugin, Juergen Brugger, Harry Heinzelmann, and Christian Hinderling. Nanopatterned self-assembled monolayers by using diblock copolymer micelles as nanometer-scale adsorption and etch masks. *Advanced Materials*, 20(10):1962–1965, 2008.

[20] Theobald Lohmueller, Eva Bock, and Joachim P. Spatz. Synthesis of Quasi-Hexagonal Ordered Arrays of Metallic Nanoparticles with Tuneable Particle Size. *Advanced Materials*, 20(12):2297–2302, 2008. _eprint: https://onlinelibrary.wiley.com/doi/pdf/10.1002/adma.200702635.

[21] V. Castelletto and I. W. Hamley. Morphologies of block copolymer melts. *Current Opinion in Solid State and Materials Science*, 2004.

[22] Matumuene Joe Ndolomingo, Ndzondelelo Bingwa, and Reinout Meijboom. Review of supported metal nanoparticles: synthesis methodologies, advantages and application as catalysts. *Journal of Materials Science*, 55(15):6195–6241, May 2020.

[23] Jiahai Wang, Wei Cui, Qian Liu, Zhicai Xing, Abdullah M. Asiri, and Xuping Sun. Recent progress in cobalt-based heterogeneous catalysts for electrochemical water splitting. *Advanced Materials*, 28(2):215–230, 2016.

[24] Lin He, Florian Weniger, Helfried Neumann, and Matthias Beller. Synthesis, characterization, and application of metal nanoparticles supported on nitrogen-doped carbon: Catalysis beyond electrochemistry. *Angewandte Chemie International Edition*, 55(41):12582–12594, 2016.

[25] Jaise Mariya George, Arun Antony, and Beena Mathew. Metal oxide nanoparticles in electrochemical sensing and biosensing: a review. *Microchimica Acta*, 185(7):358, July 2018.

[26] Xiliang Luo, Aoife Morrin, Anthony J. Killard, and Malcolm R. Smyth. Application of nanoparticles in electrochemical sensors and biosensors. *Electroanalysis*, 18(4):319–326, 2006.

[27] Didier Astruc. Introduction: Nanoparticles in catalysis. *Chemical Reviews*, 120(2):461–463, 2020. PMID: 31964144.

[28] Samuel M. Stavis, Jeffrey A. Fagan, Michael Stopa, and J. Alexander Liddle. Nanoparticle Manufacturing – Heterogeneity through Processes to Products. *ACS Appl. Nano Mater.*, 1(9):4358–4385, September 2018.

[29] Ayse Turak. On the Role of LiF in Organic Optoelectronics. *Electron. Mater.*, 2(2):198–221, June 2021.

[30] Ayse Turak, Taner Aytun, and Cleva W Ow-Yang. Solution processed LiF anode modification for polymer solar cells. *Appl. Phys. Lett.*, 100(25):253303, 2012.

[31] Seung Il Lee, Geum Jae Yun, Jin Wook Kim, Gregory Hanta, Kunyu Liang, Lazar Kojvic, Lok Shu Hui, Ayse Turak, and Woo Young Kim. Improved hole injection for blue phosphorescent organic light-emitting diodes using solution deposited tin oxide nano-particles decorated ITO anodes. *Scientific Reports*, 9(1):2411, February 2019.

[32] Seung Il Lee, Kunyu Liang, Lok Shu Hui, Ramis Arbi, Muhammad Munir, Seok Je Lee, Jin Wook Kim, Ki Ju Kim, Woo Young Kim, and Ayse Turak. Necessity of submonolayer LiF anode interlayers for improved device performance in blue phosphorescent OLEDs. *Journal of Materials Science: Materials in Electronics*, 32(1):1161–1177, January 2021.

[33] Heyou Zhang, Jasper Cadusch, Calum Kinnear, Timothy James, Ann Roberts, and Paul Mulvaney. Direct Assembly of Large Area Nanoparticle Arrays. *ACS Nano*, 12(8):7529–7537, August 2018.

[34] Muhammad Munir, Jinglan Tan, Ramis Arbi, Pedro Oliveira, Elisabeth Leeb, Yolanda Salinas, Markus Clark Scharber, Niyazi Serdar Sariciftci, and Ayse Turak. Enhanced stokes shift and phase stability by cosynthesizing perovskite nanoparticles (mapbi3/mapbbr3) in a single solution. *Advanced Photonics Research*, n/a(n/a):2100372.

[35] Tsuyoshi Tokubuchi, Ramis Imran Arbi, Pan Zhenhua, Kenji Katayama, Ayse Turak, and Woon Yong Sohn. Enhanced photoelectrochemical water splitting

efficiency of hematite (α-Fe2O3)-Based photoelectrode by the introduction of maghemite (γ-Fe2O3) nanoparticles. *J. Photochem. Photobiol. A*, 410:113179, April 2021.

[36] Justin G. Kennemur. Poly(vinylpyridine) Segments in Block Copolymers: Synthesis, Self-Assembly, and Versatility. *Macromolecules*, 52(4):1354–1370, February 2019.

[37] M. Jaritz, H. Behm, Ch Hopmann, D. Kirchheim, F. Mitschker, P. Awakowicz, and R. Dahlmann. The effect of UV radiation from oxygen and argon plasma on the adhesion of organosilicon coatings on polypropylene. *Journal of Physics D: Applied Physics*, 50(1):015201, November 2016. Publisher: IOP Publishing.

[38] Yusuke Fukunaga, Roberto C. Longo, Peter L. G. Ventzek, Barton Lane, Alok Ranjan, Gyeong S. Hwang, Gregory Hartmann, Takayoshi Tsutsumi, Kenji Ishikawa, Hiroki Kondo, Makoto Sekine, and Masaru Hori. Interaction of oxygen with polystyrene and polyethylene polymer films: A mechanistic study. *Journal of Applied Physics*, 127(2):023303, January 2020. Publisher: American Institute of Physics.

[39] P. Luan and G. S. Oehrlein. Stages of polymer transformation during remote plasma oxidation (RPO) at atmospheric pressure. *Journal of Physics D: Applied Physics*, 51(13):135201, March 2018. Publisher: IOP Publishing.

[40] Lok Shu Hui, Eric Whiteway, Michael Hilke, and Ayse Turak. Synergistic oxidation of CVD graphene on Cu by oxygen plasma etching. *Carbon*, 125:500–508, December 2017.

[41] Kateryna Bazaka, Oleg Baranov, Uros Cvelbar, Bojan Podgornik, Youmei Wang, Shiyong Huang, Luxiang Xu, Mark Lim, Igor Levchenko, and Shuyan Xu. Oxygen plasmas: A sharp chisel and handy trowel for nanofabrication. *Nanoscale*, September 2018.

[42] Lok Shu Hui, Muhammad Munir, An Vuong, Michael Hilke, Victor Wong, Giovanni Fanchini, Markus Clark Scharber, Niyazi Serdar Sariciftci, and Ayse Turak. Universal Transfer Printing of Micelle-Templated Nanoparticles Using Plasma-Functionalized Graphene. *ACS Appl. Mater. Interfaces*, 12(41):46530–46538, October 2020.

[43] Kunyu Liang, Lok Shu Hui, and Ayse Turak. Probing the multi-step crystallization dynamics of micelle templated nanoparticles: Structural evolution of single crystalline γ-Fe 2 O 3. *Nanoscale*, 11(18):9076–9084, May 2019. Publisher: The Royal Society of Chemistry.

[44] Ramis Arbi, Lok Shu Hui, Maria Dittrich, and Ayse Turak. Utility of far-field effects from tip-assisted raman spectroscopy for the detection of a monolayer of diblock copolymer reverse micelles for nanolithography. *Physical Chemistry Chemical Physics*, 23(18):11065–11074, 2021.

[45] Ramis Arbi and Ayse Turak. Resonance enhanced raman modes of polymer due to proximity of certain precursor salts. *In preparation for submission.*

[46] Irina Chamritski and Gary Burns. Infrared- and Raman-Active Phonons of Magnetite, Maghemite, and Hematite: A Computer Simulation and Spectroscopic Study. *J. Phys. Chem. B*, 109(11):4965–4968, March 2005.

[47] H. Kanno and J. Hiraishi. A Raman study of aqueous solutions of ferric nitrate, ferrous chloride and ferric chloride in the glassy state. *J. Raman Spectrosc.*, 12(3):224–227, 1982.

[48] Charles Soong, Patrick Woo, and David Hoyle. Contamination Cleaning of TEM/SEM Samples with the ZONE Cleaner. *Microscopy Today*, 20(6):44–48, November 2012. Publisher: Cambridge University Press.

[49] Andras Vladar, David Hoyle, and Hosoya Kotaro. Electron Irradiation Cleaning of the SEM and its Samples. *Microscopy and Microanalysis*, 27(S1):434–435, 2021. Edition: 2021/07/30 Publisher: Cambridge University Press.

[50] Sparkle ec of hitachi high-technologies canada, inc.

[51] I. Horcas, R. Fernandez, J. M. Gómez-Rodriguez, J. Colchero, J. Gómez-Herrero, and A. M. Baro. WSXM: A software for scanning probe microscopy and a tool for nanotechnology. *Review of Scientific Instruments*, 78(1):013705, January 2007. Publisher: American Institute of Physics.

[52] Joseph L. Lippert and E. Steven Brandt. Surface-enhanced Raman spectroscopy of poly(2-vinylpyridine) adsorbed on silver electrode surfaces. *Langmuir*, 4(1):127–132, January 1988.

[53] W. H. Tsai, F. J. Boerio, S. J. Clarson, E. E. Parsonage, and M. Tirrell. Characterization of adsorbed 2-vinylpyridine/styrene diblock copolymers on silver surfaces using surface-enhanced Raman scattering. *Macromolecules*, 24(9):2538–2545, April 1991.

[54] P. P. Hong, F. J. Boerio, M. Tirrell, S. Dhoot, and P. Guenoun. An investigation of the adsorption of polystyrene/poly (2-vinylpyridine) diblock copolymers onto silver substrates using surface-enhanced Raman scattering. *Macromolecules*, 26(15):3953–3959, July 1993. Publisher: American Chemical Society.

[55] F. Genuzio, A. Sala, Th. Schmidt, D. Menzel, and H.-J. Freund. Phase transformations in thin iron oxide films: Spectromicroscopic study of velocity and shape of the reaction fronts. *Surf. Sci.*, 648:177–187, June 2016.

[56] J. P. Luongo. Infrared study of oxygenated groups formed in polyethylene during oxidation. *J. Polym. Sci.*, 42(139):139–150, January 1960.

[57] Carles Corbella, Simon Große-Kreul, and Achim von Keudell. Exploring the Structure of the Modified Top Layer of Polypropylene During Plasma Treatment. *Plasma Process. Polym.*, 12:564–573, 2015.

[58] Gregor Primc. Generation of Neutral Chemically Reactive Species in Low-Pressure Plasma. *Frontiers in Physics*, 10, 2022.

[59] Alenka Vesel, Rok Zaplotnik, Miran Mozetič, and Gregor Primc. Surface modification of PS polymer by oxygen-atom treatment from remote plasma: Initial kinetics of functional groups formation. *Applied Surface Science*, 561:150058, September 2021.

[60] Achim von Keudell and Carles Corbella. Unraveling synergistic effects in plasma-surface processes by means of beam experiments. *J. Vac. Sci. Technol., A*, 35(5):050801, May 2017.

[61] M. A. Hartney, D. W. Hess, and D. S. Soane. Oxygen plasma etching for resist stripping and multilayer lithography. *Journal of Vacuum Science & Technology B: Microelectronics Processing and Phenomena*, 7(1):1–13, January 1989.

[62] Marta Palacios, Olga Garcia, and Juan Rodriguez-Hernandez. Constructing Robust and Functional Micropatterns on Polystyrene Surfaces by Using Deep UV Irradiation. *Langmuir*, 29(8):2756–2763, February 2013. Publisher: American Chemical Society.

[63] Van-Tien Bui, Hwa Su Lee, Jae-Hak Choi, and Ho-Suk Choi. Data from crosslinked PS honeycomb thin film by deep UV irradiation. *Data in Brief*, 5:990–994, December 2015.

[64] Nan Gao and Yuying Yan. Characterisation of surface wettability based on nanoparticles. *Nanoscale*, 4:2202–2218, 2012.

[65] Hendrik Heinz, Chandrani Pramanik, Ozge Heinz, Yifu Ding, Ratan K. Mishra, Delphine Marchon, Robert J. Flatt, Irina Estrela-Lopis, Jordi Llop, Sergio Moya, and Ronald F. Ziolo. Nanoparticle decoration with surfactants: Molecular interactions, assembly, and applications. *Surface Science Reports*, 72(1):1–58, 2017.

[66] Shivaprakash N. Ramakrishna, Lucy Y. Clasohm, Akshata Rao, and Nicholas D. Spencer. Controlling adhesion force by means of nanoscale surface roughness. *Langmuir*, 27(16):9972–9978, 2011. PMID: 21721580.

[67] David T. Thompson. Using gold nanoparticles for catalysis. *Nano Today*, 2(4):40–43, 2007.

[68] Hyeonghwa Yu and Ayse Turak. Nanoreactors or nanoscale stablizers: Routes for solution processed indium tin oxide nanoparticles by reverse micelle deposition. *Can. J. Phys.*, 92(7/8):797–801, January 2014.

[69] Alla Petukhova & Eugenia Kumacheva Zhihong Nie. Properties and emerging applications of self-assembled structures made from inorganic nanoparticles. *Nature Nanotech*, 5:15–25, January 2010.

[70] Miguel A. Correa-Duarte, Jorge Perez-Juste, Ana Sanchez-Iglesias, Michael Giersig, and Luis M. Liz-Marzan. Aligning au nanorods by using carbon nanotubes as templates. *Angewandte Chemie International Edition*, 44(28):4375–4378, 2005.

[71] Erik Dujardin, Charlie Peet, Gerald Stubbs, James N. Culver, and Stephen Mann. Organization of metallic nanoparticles using tobacco mosaic virus templates. *Nano Letters*, 3(3):413–417, 2003.

[72] Faisal A. Aldaye, Alison L. Palmer, and Hanadi F. Sleiman. Assembling materials with dna as the guide. *Science*, 321(5897):1795–1799, 2008.

[73] John R Ferraro, Kazuo Nakamoto, and Chris W Brown. *Introductory Raman Spectroscopy*. Academic Press, Amsterdam ; Boston, 2nd ed edition, 2003.

[74] Challa S. S. R. Kumar, editor. *Raman Spectroscopy for Nanomaterials Characterization*. Springer-Verlag, Berlin Heidelberg, 2012.

[75] Gwenae Gouadec and Philippe Colomban. Raman Spectroscopy of nanomaterials: How spectra relate to disorder, particle size and mechanical properties. *Prog. Cryst. Growth Charact. Mater.*, 53(1):1–56, 2007.

[76] Lawrence C. Wagner. *Failure Analysis of Integrated Circuits.* Springer US, 1999.

[77] G. Cappuccio and M.L. Terranova. Thin film characterisation by advanced X-ray diffraction techniques, 1996.

[78] M.A. Aronova and R.D. Leapman. Development of electron energy-loss spectroscopy in the biological sciences. *MRS Bulletin*, 37(1):53–62, 2012.

[79] Donald R. Baer. Guide to making xps measurements on nanoparticles. *Journal of Vacuum Science & Technology A*, 38(3):031201, 2020.

[80] G. a. N. Connell, R. J. Nemanich, and C. C. Tsai. Interference enhanced Raman scattering from very thin absorbing films. *Appl. Phys. Lett.*, 36(1):31–33, 1980.

[81] D. Solonenko, O. D. Gordan, A. Milekhin, M. Panholzer, K. Hingerl, and D. R. T. Zahn. Interference-enhanced Raman scattering of F 16 CuPc thin films. *J. Phys. D: Appl. Phys.*, 49(11):115502, 2016.

[82] Lian C. T. Shoute, Adam Johan Bergren, Amr M. Mahmoud, Ken D. Harris, and Richard L. McCreery. Optical Interference Effects in the Design of Substrates for Surface-Enhanced Raman Spectroscopy. *Appl. Spectrosc., AS*, 63(2):133–140, 2009.

[83] Elena Bailo and Volker Deckert. Tip-enhanced Raman scattering. *Chem. Soc. Rev.*, 37(5):921–930, 2008.

[84] Satoshi Kawata, Taro Ichimura, Atsushi Taguchi, and Yasuaki Kumamoto. Nano-Raman Scattering Microscopy: Resolution and Enhancement. *Chem. Rev.*, 117(7):4983–5001, April 2017.

[85] Tanja Deckert-Gaudig, Atsushi Taguchi, Satoshi Kawata, and Volker Deckert. Tip-enhanced Raman spectroscopy – from early developments to recent advances. *Chem. Soc. Rev.*, 46(13):4077–4110, July 2017.

[86] Xian Shi, Nicolas Coca-Lopez, Julia Janik, and Achim Hartschuh. Advances in Tip-Enhanced Near-Field Raman Microscopy Using Nanoantennas. *Chem. Rev.*, 117(7):4945–4960, April 2017.

[87] Prabhat Verma. Tip-Enhanced Raman Spectroscopy: Technique and Recent Advances. *Chem. Rev.*, 117(9):6447–6466, May 2017.

[88] Xiang Wang, Sheng-Chao Huang, Teng-Xiang Huang, Hai-Sheng Su, Jin-Hui Zhong, Zhi-Cong Zeng, Mao-Hua Li, and Bin Ren. Tip-enhanced Raman spectroscopy for surfaces and interfaces. *Chem Soc Rev*, 46(13):4020–4041, 2017.

[89] Naresh Kumar, Bert M. Weckhuysen, Andrew J. Wain, and Andrew J. Pollard. Nanoscale chemical imaging using tip-enhanced Raman spectroscopy. *Nat. Protoc.*, 14(4):1169–1193, April 2019.

[90] Raoul M. Stockle, Yung Doug Suh, Volker Deckert, and Renato Zenobi. Nanoscale chemical analysis by tip-enhanced Raman spectroscopy. *Chemical Physics Letters*, 318(1):131–136, February 2000.

[91] Norihiko Hayazawa, Yasushi Inouye, Zouheir Sekkat, and Satoshi Kawata. Metallized tip amplification of near-field Raman scattering. *Optics Communications*, 183(1):333–336, September 2000.

[92] Mark S Anderson. Locally enhanced Raman spectroscopy with an atomic force microscope. *Appl. Phys. Lett.*, 76(21):3130–3132, 2000.

[93] Quang Nguyen, Razvigor Ossikovski, and Joachim Schreiber. Contrast enhancement on crystalline silicon in polarized reflection mode tip-enhanced Raman spectroscopy. *Opt. Commun.*, 274(1):231–235, 2007.

[94] D. Richards, R. G. Milner, F. Huang, and F. Festy. Tip-enhanced Raman microscopy: Practicalities and limitations. *J. Raman Spectrosc.*, 34(9):663–667, 2003.

[95] Norihiko Hayazawa, Hiroyuki Watanabe, Yuika Saito, and Satoshi Kawata. Towards atomic site-selective sensitivity in tip-enhanced Raman spectroscopy. *J. Chem. Phys.*, 125(24):244706, 2006.

[96] Emanuele Poliani, Markus R. Wagner, Asmus Vierck, Felix Herziger, Christian Nenstiel, Florentina Gannott, Manuel Schweiger, Stephanie Fritze, Armin Dadgar, Jana Zaumseil, Alois Krost, Axel Hoffmann, and Janina Maultzsch. Breakdown of Far-Field Raman Selection Rules by Light-Plasmon Coupling Demonstrated by Tip-Enhanced Raman Scattering. *J. Phys. Chem. Lett.*, 8(22):5462–5471, 2017.

[97] Martin Moskovits. Surface-enhanced spectroscopy. *Rev. Mod. Phys.*, 57(3):783–826, July 1985.

[98] Alan Campion and Patanjali Kambhampati. Surface-enhanced Raman scattering. *Chem. Soc. Rev.*, 27(4):241–250, January 1998.

[99] Lixin Xia, Maodu Chen, Xiuming Zhao, Zhenglong Zhang, Jiarui Xia, Hongxing Xu, and Mengtao Sun. Visualized method of chemical enhancement mechanism on SERS and TERS. *J. Raman Spectrosc.*, 45(7):533–540, 2014.

[100] Kevin Fiederling, Mostafa Abasifard, Martin Richter, Volker Deckert, Stefanie Grafe, and Stephan Kupfer. The chemical effect goes resonant – a full quantum mechanical approach on TERS. *Nanoscale*, 12(11):6346–6359, March 2020.

[101] M. Grant Albrecht and J. Alan Creighton. Anomalously intense Raman spectra of pyridine at a silver electrode. *J. Am. Chem. Soc.*, 99(15):5215–5217, June 1977.

[102] Lukas Novotny, Randy X. Bian, and X. Sunney Xie. Theory of nanometric optical tweezers. *Phys. Rev. Lett.*, 79(4):645–648, July 1997.

[103] Katsuyoshi Ikeda, Mai Takase, Yoshitaka Sawai, Hideki Nabika, Kei Murakoshi, and Kohei Uosaki. Hyper-raman scattering enhanced by anisotropic dimer plasmons on artificial nanostructures. *The Journal of Chemical Physics*, 127(11):111103, 2007.

[104] M. Ramsteiner, C. Wild, and J. Wagner. Interference effects in the Raman scattering intensity from thin films. *Appl. Opt., AO*, 28(18):4017–4023, September 1989.

[105] R. J. Nemanich, C. C. Tsai, and G. A. N. Connell. Interference-Enhanced Raman Scattering of Very Thin Titanium and Titanium Oxide Films. *Phys. Rev. Lett.*, 44(4):273–276, January 1980.

[106] Yimin Yang, Teng Qiu, Fan Kong, Jiyang Fan, Huiling Ou, Qingyu Xu, and Paul K. Chu. Interference effects on indium tin oxide enhanced Raman scattering. *Journal of Applied Physics*, 111(3):033110, February 2012.

[107] Bruno Pettinger, Gennaro Picardi, Rolf Schuster, and Gerhard Ertl. Surface enhanced raman spectroscopy: Towards single molecule spectroscopy. *Electrochemistry*, 68(12):942–949, 2000.

[108] C.W. Ow-Yang, J. Jia, T. Aytun, M. Zamboni, A. Turak, K. Saritas, and Y. Shigesato. Work function tuning of tin-doped indium oxide electrodes with solution-processed lithium fluoride. *Thin Solid Films*, 559:58–63, May 2014.

[109] Taner Aytun, Ayse Turak, Iain Baikie, Grzegorz Halek, and Cleva W Ow-Yang. Solution-processed LiF for work function tuning in electrode bilayers. *Nano Lett.*, 12(1):39–44, January 2012.

[110] Stephan Forster and Markus Antonietti. Amphiphilic Block Copolymers in Structure-Controlled Nanomaterial Hybrids. *Adv. Mater.*, 10(3):195–217, February 1998.

[111] N. V. Sastry and H. Hoffmann. Interaction of amphiphilic block copolymer micelles with surfactants. *Colloids and Surfaces A: Physicochemical and Engineering Aspects*, 250(1):247–261, 2004.

[112] Kauzo Nakamoto. Applications in Coordination Chemistry. In *Infrared and Raman Spectra of Inorganic and Coordination Compounds Part B*, chapter 1, pages 1–273. John Wiley & Sons, Ltd, 2009.

[113] M. Kadleikova, J. Breza, and M. Vesely. Raman spectra of synthetic sapphire. *Microelectron. J.*, 32(12):955–958, 2001.

[114] M. Fleischmann, P. J. Hendra, and A. J. McQuillan. Raman spectra of pyridine adsorbed at a silver electrode. *Chemical Physics Letters*, 26(2):163–166, 1974.

[115] David L. Jeanmaire and Richard P. Van Duyne. Surface raman spectroelectrochemistry: Part I. Heterocyclic, aromatic, and aliphatic amines adsorbed on the anodized silver electrode. *Journal of Electroanalytical Chemistry and Interfacial Electrochemistry*, 84(1):1–20, November 1977.

[116] Bhavya Sharma, Renee R. Frontiera, Anne-Isabelle Henry, Emilie Ringe, and Richard P. Van Duyne. SERS: Materials, applications, and the future. *Mater. Today*, 15(1):16–25, 2012.

[117] Paul L Stiles, Jon a Dieringer, Nilam C Shah, and Richard P Van Duyne. Surface-enhanced Raman spectroscopy. *Annu. Rev. Anal. Chem. Palo Alto Calif*, 1(July 2015):601–626, 2008.

[118] J. Stadler, C. Stanciu, C. Stupperich, and A. J. Meixner. Tighter focusing with a parabolic mirror. *Opt. Lett.*, 33(7):681–683, April 2008.

[119] Pritam Khan, Grace Brennan, James Lillis, Syed A. M. Tofail, Ning Liu, and Christophe Silien. Characterisation and manipulation of polarisation response in plasmonic and magneto-plasmonic nanostructures and metamaterials. *Symmetry*, 12(8), 2020.

[120] James B. Breckinridge and Ben R. Oppenheimer. Polarization effects in reflecting coronagraphs for white-light applications in astronomy. *Astrophys. J.*, 600(2):1091–1098, January 2004.

[121] Jan P F Lagerwall, Jesse T. McCann, Eric Formo, Giusy Scalia, and Younan Xia. Coaxial electrospinning of microfibres with liquid crystal in the core. *Chem. Commun.*, (42):5420–5422, 2008.

[122] Satyanarayan Pal. *Pyridine: A Useful Ligand in Transition Metal Complexes*. IntechOpen, November 2018.

[123] Elnaz Hobbollahi, Manuela List, and Uwe Monkowius. Poly(4-vinylpyridine) as ligand for Au(I) and Zn(II) cations: luminescent metal-containing polymers. *Monatshefte für Chemie - Chemical Monthly*, 150(5):877–883, May 2019.

[124] Graham A. Bowmaker, Effendy, Fariati, Susanto I. Rahajoe, Brian W. Skelton, and Allan H. White. Structural and Infrared Spectroscopic Studies of Some Adducts of Divalent Metal Dihalides (MX2, M = Zn, Cd; X = CI, Br, I) with Variously Hindered Monodentate Nitrogen (Pyridine) Base Ligands (L = Pyridine, 2-Methylpyridine, and Quinoline) of 1:2 Stoichiometry. *Zeitschrift für anorganische und allgemeine Chemie*, 637(10):1361–1370, 2011. https://onlinelibrary.wiley.com/doi/pdf/10.1002/zaac.201100126.

[125] Manfred Schlosser and Florence Mongin. Pyridine elaboration through organometallic intermediates: regiochemical control and completeness. *Chemical Society Reviews*, 36(7):1161–1172, June 2007. Publisher: The Royal Society of Chemistry.

[126] J. M. Harrowfield, H. Miyamae, B. W. Skelton, A. A. Soudi, and A. H. White. Lewis-Base Adducts of Lead(II) Compounds. XX. Synthesis and Structure of the 1:1 Adduct of Pyridine With Lead(II) Thiocyanate. *Australian Journal of Chemistry*, 49(10):1165–1169, 1996. Publisher: CSIRO PUBLISHING.

[127] Nam-Goo Kang, Beom-Goo Kang, Haeng-Deog Koh, Mohammad Changez, and Jae-Suk Lee. Block copolymers containing pyridine moieties: Precise synthesis and applications. *Reactive and Functional Polymers*, 69(7):470–479, July 2009.

[128] Mingqi Li and Christopher K. Ober. Block copolymer patterns and templates. *Materials Today*, 9(9):30–39, September 2006.

[129] Yao Lin, Alexander Böker, Jinbo He, Kevin Sill, Hongqi Xiang, Clarissa Abetz, Xuefa Li, Jin Wang, Todd Emrick, Su Long, Qian Wang, Anna Balazs, and Thomas P. Russell. Self-directed self-assembly of nanoparticle/copolymer mixtures. *Nature*, 434(7029):55–59, March 2005. Number: 7029 Publisher: Nature Publishing Group.

[130] Jongheon Kwak, Sung Hyun Han, Hong Chul Moon, Jin Kon Kim, Jaseung Koo, Jeong-Soo Lee, Victor Pryamitsyn, and Venkat Ganesan. Phase Behavior of Binary Blend Consisting of Asymmetric Polystyrene-block-poly(2-vinylpyridine) Copolymer and Asymmetric Deuterated Polystyrene-block-poly(4-hydroxystyrene) Copolymer. *Macromolecules*, 48(4):1262–1266, February 2015. Publisher: American Chemical Society.

[131] Andriy Horechyy, Nikolaos E. Zafeiropoulos, Bhanu Nandan, Petr Formanek, Frank Simon, Anton Kiriy, and Manfred Stamm. Highly ordered arrays of magnetic nanoparticles prepared via block copolymer assembly. *Journal of Materials Chemistry*, 20(36):7734–7741, August 2010. Publisher: The Royal Society of Chemistry.

[132] Muhammad Munir, Ramis Arbi, Markus Clark Scharber, Yolanda Salinas, Niyazi Serdar Sariciftci, and Ayse Turak. Anionic exchange route to synthesize highly uniform, stable and luminescent mapbr nanoparticles. In *OSA Advanced Photonics Congress (AP) 2020 (IPR, NP, NOMA, Networks, PVLED, PSC, SPPCom, SOF)*, page PvTu3G.5. Optica Publishing Group, 2020.

[133] Frédéric S. Diana, Seung-Heon Lee, Pierre M. Petroff, and Edward J. Kramer. Fabrication of hcp-co nanocrystals via rapid pyrolysis in inverse ps-b-pvp micelles and thermal annealing. *Nano Letters*, 3(7):891–895, 2003.

[134] Sivashankar Krishnamoorthy, Christian Hinderling, and Harry Heinzelmann. Nanoscale patterning with block copolymers. *Materials Today*, 16(11):1469–1475, 2006.

[135] Osman El-Atwani, Taner Aytun, Omer Faruk Mutaf, Vesna Srot, Peter A. van Aken, and Cleva W. Ow-Yang. Determining the morphology of polystyrene-block-poly(2-vinylpyridine) micellar reactors for zno nanoparticle synthesis. *Langmuir*, 26(10):7431–7436, 2010.

[136] Hu Zhu, Jean-François Masson, and C. Geraldine Bazuin. Monolayer arrays of nanoparticles on block copolymer brush films. *Langmuir*, 35(15):5114–5124, 2019.

[137] Hyowon Han, Beomjin Jeong, Tae Hyun Park, Wonhee Cha, Suk Man Cho, Yeongsik Kim, Hong Hee Kim, Dongho Kim, Do Yeol Ryu, Won Kook Choi, and Cheolmin Park. Highly photoluminescent and environmentally stable perovskite nanocrystals templated in thin self-assembled block copolymer films. *Advanced Functional Materials*, 29(26):1808193, 2019.

[138] Shaocong Hou, Yuzheng Guo, Yuguo Tang, and Qimin Quan. Synthesis and stabilization of colloidal perovskite nanocrystals by multidentate polymer micelles. *ACS Applied Materials & Interfaces*, 9(22):18417–18422, 2017.

[139] Kyunghyeon Lee, Joon Young Kim, and Byeong-Hyeok Sohn. White-emitting film of diblock copolymer micelles with perovskite nanocrystals. *RSC Adv.*, 12(11):6389–6395, 2022.

[140] Qiang Fu, Shaoming Huang, and Jie Liu. Chemical Vapor Depositions of Single-Walled Carbon Nanotubes Catalyzed by Uniform Fe2O3 Nanoclusters Synthesized Using Diblock Copolymer Micelles. *The Journal of Physical Chemistry B*, 108(20):6124–6129, May 2004. Publisher: American Chemical Society.

[141] Michael Haupt, Stephan Miller, Andreas Ladenburger, Rolf Sauer, Klaus Thonke, Silke Riethmueller, Martin Moeller, and Florian Banhart. Semiconductor Nanostructures defined by self-organizing Polymers. *MRS Online Proceedings Library (OPL)*, 728, 2002. Publisher: Cambridge University Press.

[142] Xiaojiang Zhang, Kenneth D. Harris, Nathanael L. Y. Wu, Jeffrey N. Murphy, and Jillian M. Buriak. Fast Assembly of Ordered Block Copolymer Nanostructures through Microwave Annealing. *ACS Nano*, 4(11):7021–7029, November 2010.

[143] Jinan Chai, Dong Wang, Xiangning Fan, and Jillian M. Buriak. Assembly of aligned linear metallic patterns on silicon. *Nature Nanotechnology*, 2(8):500–506, August 2007.

[144] Yoshio Sageshima, Atsushi Noro, and Yushu Matsushita. Structural isomer effects on the morphology of block copolymer/metal salts hybrids. *Journal of Polymer Science Part B: Polymer Physics*, 52(5):377–386, 2014.

[145] M. Anderson, C. Ramanan, C. Fontanesi, A. Frick, S. Surana, D. Cheyns, M. Furno, T. Keller, S. Allard, U. Scherf, D. Beljonne, G. D'Avino, E. von Hauff, and E. Da Como. Displacement of polarons by vibrational modes in doped conjugated polymers. *Physical Review Materials*, 1(5):055604, October 2017. Publisher: American Physical Society.

[146] Yukio Furukawa. Electronic Absorption and Vibrational Spectroscopies of Conjugated Conducting Polymers. *The Journal of Physical Chemistry*, 100(39):15644–15653, January 1996. Publisher: American Chemical Society.

[147] B. L. Papke, M. A. Ratner, and D. F. Shriver. Vibrational spectroscopy and structure of polymer electrolytes, poly(ethylene oxide) complexes of alkali metal salts. *Journal of Physics and Chemistry of Solids*, 42(6):493–500, January 1981.

[148] John R. Lombardi, Ronald L. Birke, Tianhong Lu, and Jia Xu. Charge-transfer theory of surface enhanced Raman spectroscopy: Herzberg–Teller contributions. *The Journal of Chemical Physics*, 84(8):4174–4180, April 1986.

[149] John R. Lombardi and Ronald L. Birke. Time-dependent picture of the charge-transfer contributions to surface enhanced Raman spectroscopy. *The Journal of Chemical Physics*, 126(24):244709, June 2007. Publisher: American Institute of Physics.

[150] T G Spiro and P Stein. Resonance Effects in Vibrational Scattering From Complex Molecules. *Annual Review of Physical Chemistry*, 28(1):501–521, 1977. _eprint: https://doi.org/10.1146/annurev.pc.28.100177.002441.

[151] Alexander F. Wells. *Structural Inorganic Chemistry.* Oxford Classic Texts in the Physical Sciences. Oxford, New York, September 2012.

[152] F. Albert Cotton, Geoffrey Wilkinson, Carlos A. Murillo, and Manfred Bochmann. *Advanced Inorganic Chemistry.* John Wiley and Sons, Inc., 1999. Accepted: 2020-04-29T01:31:53Z.

[153] A. E. Martell, R. D. Hancock, and R. J. Motekaitis. Factors affecting stabilities of chelate, macrocyclic and macrobicyclic complexes in solution. 133:39–65, 1994.

[154] Robert D. Hancock and Arthur E. Martell. The chelate, cryptate and macrocyclic effects. 6(5):237–284.

[155] Xiaotian Wang, Wensheng Shi, Guangwei She, and Lixuan Mu. Surface-Enhanced Raman Scattering (SERS) on transition metal and semiconductor nanostructures. *Physical Chemistry Chemical Physics*, 14(17):5891, 2012.

[156] Xiaotian Wang, Wensheng Shi, Guangwei She, and Lixuan Mu. Using Si and Ge Nanostructures as Substrates for Surface-Enhanced Raman Scattering Based on Photoinduced Charge Transfer Mechanism. *Journal of the American Chemical Society*, 133(41):16518–16523, October 2011. Publisher: American Chemical Society.

[157] Andreas C. Albrecht. On the Theory of Raman Intensities. *The Journal of Chemical Physics*, 34(5):1476–1484, May 1961. Publisher: American Institute of Physics.

[158] Dennis P. Strommen and Kazuo Nakamoto. Resonance raman spectroscopy. *Journal of Chemical Education*, 54(8):474, August 1977. Publisher: American Chemical Society.

[159] Kazuo Nakamoto. Theory of Normal Vibrations. In *Infrared and Raman Spectra of Inorganic and Coordination Compounds*, pages 1–147. John Wiley & Sons, Ltd, 2008. Section: 1 _eprint: https://onlinelibrary.wiley.com/doi/pdf/10.1002/9780470405840.ch1.

[160] Wiley Science Solutions. KnowItAll Raman Spectral Database Collection.

[161] Ramis Arbi, Muhammad Munir, and Ayse Turak. Effectivity of plasma etching on template removal of reverse micelle deposited nanoparticles. *In preparation for submission.*

[162] David Tuschel. Stress, Strain, and Raman Spectroscopy. *Spectroscopy*, 34(9):10–21, September 2019. Publisher: MJH Life Sciences.

[163] Joseph L. Lippert and E. Steven Brandt. Surface-enhanced Raman spectroscopy of poly(2-vinylpyridine) adsorbed on silver electrode surfaces. *Langmuir*, 4(1):127–132, January 1988. Publisher: American Chemical Society.

[164] A. M. Lyons, M. J. Vasile, E. M. Pearce, and J. V. Waszczak. Copper chloride complexes with poly(2-vinylpyridine): preparation and redox properties. *Macromolecules*, 21(11):3125–3134, November 1988. Publisher: American Chemical Society.

[165] Anton Dimitrov, Detlef Heidemann, and Erhard Kemnitz. F/cl-exchange on alcl3-pyridine adducts: Synthesis and characterization of trans-difluoro-tetrakis-pyridine-aluminum-chloride, [alf2(py)4]+cl-. *Inorganic Chemistry*, 45(26):10807–10814, 2006. PMID: 17173440.

[166] Arnd Vogler and Horst Kunkely. Photoreactivity of gold complexes. *Coordination Chemistry Reviews*, 219-221:489–507, October 2001.

[167] R. B. Mason and J. H. Mathews. Equilibrium in the Systems: Zinc Chloride-Pyridine and Calcium Chloride-Pyridine. *The Journal of Physical Chemistry*, 29(9):1178–1183, September 1925. Publisher: American Chemical Society.

[168] Faridul Islam, Md Amran Hossain, Nur Mostaq Shah, Hridika Talukder Barua, Md Alamgir Kabir, Mohammad Jamshed Khan, and Romel Mullick. Synthesis, Characterization, and Antimicrobial Activity Studies of Ni(II) Complex with Pyridine as a Ligand. *Journal of Chemistry*, 2015:e525239, April 2015. Publisher: Hindawi.

[169] Greg Hanta. Nanomechanical Dependence of Micelles on Salt Loading Ratios: A Story of Salt Complexation, Micellar Stability, and Nanoparticle Spatial Distribution, August 2019.

[170] Simon A. Cotton. Iron(III) chloride and its coordination chemistry. *Journal of Coordination Chemistry*, 71(21):3415–3443, November 2018.

[171] Wiley Roy Mason and Harry B. Gray. Electronic structures and spectra of square-planar gold(III) complexes. *Inorganic Chemistry*, 7(1):55–58, January 1968. Publisher: American Chemical Society.

[172] S. J. Costanzo and N. B. Jurinski. Charge transfer complexes of aluminum chloride. *Tetrahedron*, 23(6):2571–2576, January 1967.

[173] Arnd Vogler and Horst Kunkely. Optical Ligand to Ligand Charge Transfer of Metal Complexes Including Ligand-Based Mixed-Valence Systems. *Comments on Inorganic Chemistry*, 9(3-4):201–220, January 1990. Publisher: Taylor & Francis _eprint: https://doi.org/10.1080/02603599008035810.

[174] Mikio Morita, Kunio Hirosawa, Toshio Sato, and Koji Ouchi. Interaction between Aromatics and Zinc Chloride. II. The Formation of σ-Complexes and Cation Radicals on Supported Zinc Chloride. *Bulletin of the Chemical Society of Japan*, 53(10):3013–3014, October 1980. Publisher: The Chemical Society of Japan.

[175] Jiri Tucek, Kingsley Christian Kemp, Kwang Soo Kim, and Radek Zboȓil. Iron-oxide-supported nanocarbon in lithium-ion batteries, medical, catalytic, and environmental applications. *ACS Nano*, 8(8):7571–7612, 2014.

[176] Karel Sirok, Jana Jiresova, and Lubomir Hudec. Iron oxide thin film gas sensor. *Thin Solid Films*, 245(1–2):211–214, 1994.

[177] Pier Paolo Prosini, Maria Carewska, Stefano Loreti, Carla Minarini, and Stefano Passerini. Lithium iron oxide as alternative anode for li-ion batteries. *Int. J. Inorg. Mater.*, 2(4):365–370, 2000.

[178] Shendan Zhang, Mingjie Yang, Kunyu Liang, Ayse Turak, Bingxue Zhang, Da Meng, Chuanxi Wang, Fengdong Qu, Wenlong Cheng, and Minghui Yang.

An acetone gas sensor based on nanosized Pt-loaded Fe2O3 nanocubes. *Sensors and Actuators B: Chemical*, 290:59–67, July 2019.

[179] Libor Machala, Jiri Tucek, and Radek Zboril. Polymorphous Transformations of Nanometric Iron(III) Oxide: A Review. *Chem. Mater.*, 23(14):3255–3272, July 2011.

[180] Taeghwan Hyeon. Chemical synthesis of magnetic nanoparticles. *Chem. Commun.*, 3(8):927–934, 2003.

[181] Monty Liong, Jie Lu, Michael Kovochich, Tian Xia, Stefan G Ruehm, Andre E Nel, Fuyuhiko Tamanoi, and Jeffrey I Zink. Multifunctional inorganic nanoparticles for imaging, targeting, and drug delivery. *ACS Nano*, 2(5):889–896, 2008.

[182] Ajay Kumar Gupta and Mona Gupta. Synthesis and surface engineering of iron oxide nanoparticles for biomedical applications. *Biomaterials*, 26(18):3995–4021, 2005.

[183] Zhen Li, Li Wei, Mingyuan Gao, and Hao Lei. One-pot reaction to synthesize biocompatible magnetite nanoparticles. *Adv. Mater.*, 17(8):1001–1005, 2005.

[184] Hyon Bin Na, In Chan Song, and Taeghwan Hyeon. Inorganic nanoparticles for MRI contrast agents. *Adv. Mater.*, 21(21):2133–2148, 2009.

[185] Benjamin C. M. Martindale and Erwin Reisner. Bi-Functional Iron-Only Electrodes for Efficient Water Splitting with Enhanced Stability through In Situ Electrochemical Regeneration. *Advanced Energy Materials*, 6(6):1502095, 2016. _eprint: https://onlinelibrary.wiley.com/doi/pdf/10.1002/aenm.201502095.

[186] Pavani Katikaneani, Ajay Kumar Vaddepally, Narender Reddy Tippana, Ramu Banavath, and Srivani Kommu. Phase Transformation of Iron Oxide Nanoparticles from Hematite to Maghemite in Presence of Polyethylene Glycol: Application as Corrosion Resistant Nanoparticle Paints. *Journal of Nanoscience*, 2016:1–6, August 2016.

[187] Pier Carlo Ricci, C. M. Carbonaro, R. Corpino, D. Chiriu, and L. Stagi. Surface effects and phase stability in metal oxides nanoparticles under visible irradiation. *AIP Conference Proceedings*, 1624(1):104–110, October 2014. Publisher: American Institute of Physics.

[188] Afshin Masoudi, Hamid Reza Madaah Hosseini, Seyed Morteza Seyed Reyhani, Mohammad Ali Shokrgozar, Mohammad Ali Oghabian, and Reza Ahmadi. Long-term investigation on the phase stability, magnetic behavior, toxicity, and MRI characteristics of superparamagnetic Fe/Fe-oxide core/shell nanoparticles. *International Journal of Pharmaceutics*, 439(1):28–40, December 2012.

[189] Igor Chourpa, Laurence Douziech-Eyrolles, Lazare Ngaboni-Okassa, Jean-Francois Fouquenet, Simone Cohen-Jonathan, Martin Souce, Hervé Marchais, and Pierre Dubois. Molecular composition of iron oxide nanoparticles, precursors for magnetic drug targeting, as characterized by confocal Raman microspectroscopy. *The Analyst*, 130(10):1395, 2005.

[190] I. V. Chernyshova, M. F. Hochella Jr, and A. S. Madden. Size-dependent structural transformations of hematite nanoparticles. 1. Phase transition. *Phys. Chem. Chem. Phys.*, 9(14):1736, 2007.

[191] S Laurent, D Forge, M Port, a Roch, C Robic, L V Elst, and R N Muller. Magnetic Iron Oxide Nanoparticles: Synthesis, Stabilization, Vectorization, Physicochemical Characterizations, and Biological Applications. *Chem. Rev.*, 108(6):2064–2110, 2008.

[192] Shunsuke Sakurai, Asuka Namai, Kazuhito Hashimoto, and Shin-ichi Ohkoshi. First Observation of Phase Transformation of All Four Fe2O3 Phases ($\gamma \rightarrow \epsilon \rightarrow \beta \rightarrow \alpha$-Phase). *J. Am. Chem. Soc.*, 131(51):18299–18303, December 2009.

[193] Weiliang Qi, Ying Zhou, Siqi Liu, Honghong Liu, Lok Shu Hui, Ayse Turak, Jun Wang, and Minghui Yang. Oxidized impurity in transition metal nitride for improving the hydrogen evolution efficiency of transition metal nitride-based catalyst. *Applied Materials Today*, 18:100476, March 2020.

[194] R M Cornell and U Schwertmann. *The Iron Oxides: Structure, Properties, Reactions, Occurences and Uses.* Wiley-VCH Verlag GmbH & Co. KGaA, 2003.

[195] Young Soo Kang, Subhash Risbud, John F. Rabolt, and Pieter Stroeve. Synthesis and Characterization of Nanometer-Size Fe3O4 and γ-Fe2O3 Particles. *Chem. Mater.*, 8(9):2209–2211, 1996.

[196] Wenhui Zhu, Jonathan Winterstein, Itai Maimon, Qiyue Yin, Lu Yuan, Aleksey N. Kolmogorov, Renu Sharma, and Guangwen Zhou. Atomic structural evolution during the reduction of α-Fe2O3nanowires. *J. Phys. Chem. C*, 120(27):14854–14862, 2016.

[197] Xisheng Ye, Dongsheng Lin, Zhengkuan Jiao, and Lide Zhang. The thermal stability of nanocrystalline maghemite. *J. Phys. D: Appl. Phys.*, 31(20):2739–2744, October 1998.

[198] Alexandra Navrotsky, Lena Mazeina, and Juraj Majzlan. Size-Driven Structural and Thermodynamic Complexity in Iron Oxides. *Science*, 319(5870):1635–1638, March 2008.

[199] P. Ayyub, M. Multani, M. Barma, V. R. Palkar, and R. Vijayaraghavan. Size-induced structural phase transitions and hyperfine properties of microcrystalline Fe2O3. *J. Phys. C: Solid State Phys.*, 21(11):2229–2245, April 1988.

[200] Karthik Kannan, D. Radhika, A.S Nesaraj, Kishor Kumar Sadasivuni, Kakarla Raghava Reddy, Deepak Kasai, and Anjanapura V. Raghu. Photocatalytic, antibacterial and electrochemical properties of novel rare earth metal oxides-based nanohybrids. *Materials Science for Energy Technologies*, 3:853–861, 2020.

[201] Youkun Tao, Jing Shao, Jianxin Wang, and Wei Guo Wang. Morphology control of ce0.9gd0.1o1.95 nanopowder synthesized by sol–gel method using pvp as a surfactant. *Journal of Alloys and Compounds*, 484(1):729–733, 2009.

[202] Madhavi Jonnalagadda, Vishnu Bhotla Prasad, and Anjanapura V. Raghu. Synthesis of composite nanopowder through mn doped zns-cds systems and its structural, optical properties. *Journal of Molecular Structure*, 1230:129875, 2021.

[203] Usha Jinendra, Jeethendra Kumar, B M Nagabhushana, Anjanapura V Raghu, and Dinesh Bilehal. Facile synthesis of cofe2o4 nanoparticles and application in removal of malachite green dye. *Green Materials*, 7(3):137–142, 2019.

[204] Muhammad Munir, Muhammad Habib, Salman Ali Khan, Myong-Ho Kim, Soonil Lee, Tae-Kwon Song, Abrar H. Baluch, Ayse Turak, and Ali Hussain. Energy storage and piezoelectric properties of lead-free SrTiO3-modified 0.965Bi0.5Na0.5TiO3–0.035BaTiO3 ceramics. *Journal of Materials Science: Materials in Electronics*, March 2021.

[205] Muhammad Habib, Muhammad Munir, Fazli Akram, Soonil Lee, Tae-Kwon Song, Ayse Turak, Myong-Ho Kim, and Ali Hussain. Structural evolution and electromechanical properties of srtio3-modified bi0.5na0.5tio3–batio3 ceramics prepared by sol-gel and hydrothermal methods. *Materials Chemistry and Physics*, 266:124529, 2021.

[206] Sung Min Lee, Ki Chang Song, and Bum Suk Lee. Antibacterial activity of silver nanoparticles prepared by a chemical reduction method. *Korean Journal of Chemical Engineering*, 27(2):688–692, March 2010.

[207] Mohammad Amin Jadidi Kouhbanani, Nasrin Beheshtkhoo, Ali Mohammad Amani, Saeed Taghizadeh, Vahid Beigi, Abbas Zakeri Bazmandeh, and Nesa Khalaf. Green synthesis of iron oxide nanoparticles using \$\less\$i\$\greater\$Artemisia vulgaris\$\less\$/i\$\greater\$ leaf extract and their application as a heterogeneous Fenton-like catalyst for the degradation of methyl orange. *Materials Research Express*, 5(11):115013, September 2018. Publisher: IOP Publishing.

[208] J.J. Merkel, T. Sontheimer, B. Rech, and C. Becker. Directional growth and crystallization of silicon thin films prepared by electron-beam evaporation on oblique and textured surfaces. *Journal of Crystal Growth*, 367:126–130, 2013.

[209] Chaoliang Tan, Junze Chen, Xue-Jun Wu, and Hua Zhang. Epitaxial growth of hybrid nanostructures. *Nature Reviews Materials*, 3(2):17089, January 2018.

[210] Amira Hannachi, Alfredo Segura, and Hager Maghraoui-Meherzi. Growth of manganese sulfide (α-mns) thin films by thermal vacuum evaporation: Structural, morphological and optical properties. *Materials Chemistry and Physics*, 181:326–332, 2016.

[211] Guoxiang Wang, Qiuhua Nie, Xiang Shen, Fen Chen, Jun Li, Wei Zhang, Tiefeng Xu, and Shixun Dai. Phase change and optical band gap behavior of ge–te–ga thin films prepared by thermal evaporation. *Vacuum*, 86(10):1572–1575, 2012. Selected papers from the 20th Conference on Ion-Surface Interactions, Zvenigorod, Moscow Region 25 – 29 August 2011.

[212] R. Shwetharani, H.R. Chandan, M. Sakar, Geetha R. Balakrishna, Kakarla Raghava Reddy, and Anjanapura V. Raghu. Photocatalytic semiconductor thin films for hydrogen production and environmental applications. *International Journal of Hydrogen Energy*, 45(36):18289–18308, 2020. Waste and Biomass-derived Hydrogen Synthesis and Implementation.

[213] Yongqi Liang and Roel van de Krol. Influence of Si dopant and SnO2interfacial layer on the structure of the spray-deposited Fe2O3films. *Chem. Phys. Lett.*, 479(1-3):86–90, 2009.

[214] D. Bersani, P. P. Lottici, and A. Montenero. Micro-Raman investigation of iron oxide films and powders produced by sol-gel syntheses. *J. Raman Spectrosc.*, 30(5):355–360, May 1999.

[215] J. Lopez-Sanchez, A. Serrano, A. Del Campo, M. Abuin, O. Rodriguez de la Fuente, and N. Carmona. Sol–Gel Synthesis and Micro-Raman Characterization of ϵ-Fe2O3 Micro- and Nanoparticles. *Chem. Mater.*, 28(2):511–518, January 2016.

[216] Katsuo Murata and Donald E. Irish. Raman studies of the hydrated melt of FeCl3 6H2O. *Spectrochim. Acta, Part A*, 44(7):739–743, 1988.

[217] M Ibrahim Dar and S A Shivashankar. Single crystalline magnetite, maghemite, and hematite nanoparticles with rich coercivity. *RSC Adv.*, 4(8):4105–4113, 2014.

[218] D. L. A. de Faria, S. Venancio Silva, and M. T. de Oliveira. Raman microspectroscopy of some iron oxides and oxyhydroxides. *J. Raman Spectrosc.*, 28(11):873–878, November 1997.

[219] Guilherme V M Jacintho, Paola Corio, and Joel C. Rubim. Surface-enhanced Raman spectra of magnetic nanoparticles adsorbed on a silver electrode. *J. Electroanal. Chem.*, 603(1):27–34, 2007.

[220] Aaron M. Jubb and Heather C. Allen. Vibrational spectroscopic characterization of hematite, maghemite, and magnetite thin films produced by vapor deposition. *ACS Appl. Mater. Interfaces*, 2(10):2804–2812, 2010.

[221] Huihui Zhu, Jinxia Deng, Jun Chen, Ranbo Yu, and Xianran Xing. Growth of hematite nanowire arrays during dense pentlandite oxidation. *J. Mater. Chem. A*, 2(9):3008–3014, 2014.

[222] N. Caswell and S. A. Solin. Vibrational excitations of pure FeCl3 and graphite intercalated with ferric chloride. *Solid State Commun.*, 27(10):961–967, 1978.

[223] Weijie Zhao, Ping Heng Tan, Jian Liu, and Andrea C. Ferrari. Intercalation of Few-Layer Graphite Flakes with FeCl3: Raman Determination of Fermi Level, Layer Decoupling and Stability. *J. Am. Chem. Soc.*, 133(15):5941–5946, 2011.

[224] Pamela S. Hill and Edwin A. Schauble. Modeling the effects of bond environment on equilibrium iron isotope fractionation in ferric aquo-chloro complexes. *Geochim. Cosmochim. Acta*, 72(8):1939–1958, 2008.

[225] Tadao Sugimoto and Atsushi Muramatsu. Formation Mechanism of Monodispersed α-Fe2O3 Particles in Dilute FeCl3 Solutions. *Journal of Colloid and Interface Science*, 184(2):626–638, 1996.

[226] Hongtao Cui, Yan Liu, and Wanzhong Ren. Structure switch between α-Fe2O3, γ-Fe2O3 and Fe3O4 during the large scale and low temperature sol-gel synthesis of nearly monodispersed iron oxide nanoparticles. *Adv. Powder Technol.*, 24(1):93–97, 2013.

[227] Kurt Stubenrauch, Christian Moitzi, Gerhard Fritz, Otto Glatter, Gregor Trimmel, and Franz Stelzer. Precise Tuning of Micelle, Core, and Shell Size by the Composition of Amphiphilic Block Copolymers Derived from ROMP Investigated by DLS and SAXS. *Macromolecules*, 39(17):5865–5874, 2006.

[228] Frederic Calderara and Gerard Riess. Characterization of polystyrene-block-poly(4-vinyl-pyridine) block copolymer micelles in toluene solution. *Macromol. Chem. Phys.*, 197(7):2115–2132, 1996.

[229] Stephan Reiling, Marcel Besnard, and Philippe A. Bopp. Theoretical Studies on the Pyridine-I2 Charge-Transfer Complex. 1. Ab-Initio Calculations on I2 and Pyridine-I2. *J. Phys. Chem. A*, 101(24):4409–4415, 1997.

[230] Maxim E. Dokukin and Igor Sokolov. Quantitative mapping of the elastic modulus of soft materials with HarmoniX and PeakForce QNM AFM modes. *Langmuir*, 28(46):16060–16071, 2012.

[231] T. J. Young, M. A. Monclus, T. L. Burnett, W. R. Broughton, S. L. Ogin, and P. A. Smith. The use of the PeakForce TM quantitative nanomechanical mapping AFM-based method for high-resolution Young's modulus measurement of polymers. *Meas. Sci. Technol.*, 22(12):125703, 2011.

[232] Greg Hanta. *Nanomechanical Dependence of Micelles on Salt Loading Ratios: A Story of Salt Complexation, Micellar Stability, and Nanoparticle Spatial Distribution.* Master of Applied Science, McMaster University, Hamilton, Ontario, August 2019.

[233] En Wang, Jie Lu, Frank S. Bates, and Timothy P. Lodge. Effect of Corona Block Length on the Structure and Chain Exchange Kinetics of Block Copolymer Micelles. *Macromolecules*, 51(10):3563–3571, May 2018.

[234] Atefeh Khoshnood and Abbas Firoozabadi. Polar Solvents Trigger Formation of Reverse Micelles. *Langmuir*, 31(22):5982–5991, June 2015.

[235] G. Ennas, G. Marongiu, A. Musinu, A. Falqui, P. Ballirano, and R. Caminiti. Characterization of Nanocrystalline γ–Fe2O3 Prepared by Wet Chemical Method. *J. Mater. Res.*, 14(4):1570–1575, April 1999.

[236] Tianshu Zhang, Hongmei Luo, Huanxing Zeng, Ruifang Zhang, and Yusheng Shen. Synthesis and gas-sensing characteristics of high thermostability γ-Fe2O3 powder. *Sensors and Actuators B: Chemical*, 32(3):181–184, June 1996.

[237] Sasanka Deka and Pattayil Alias Joy. Enhancement of the phase transformation temperature of γ-Fe2O3 by Zn2+ doping. *J. Mater. Chem.*, 17(5):453–456, January 2007.

[238] Xiaobin Xu, Mingyuan Ge, Cen Wang, and J. Z. Jiang. High temperature stable monodisperse superparamagnetic core-shell iron-oxide@SnO2 nanoparticles. *Appl. Phys. Lett.*, 95(18):183112, November 2009.

[239] Maria F. Casula, Young-wook Jun, David J. Zaziski, Emory M. Chan, Anna Corrias, and A. Paul Alivisatos. The Concept of Delayed Nucleation in Nanocrystal Growth Demonstrated for the Case of Iron Oxide Nanodisks. *J. Am. Chem. Soc.*, 128(5):1675–1682, February 2006.

[240] D Voulgaris, C Tsitsilianis, F. J Esselink, and G Hadziioannou. Polystyrene/poly(2-vinyl pyridine) heteroarm star copolymer micelles in toluene: Morphology and thermodynamics. *Polymer*, 39(25):6429–6439, 1998.

[241] Alan Boyde, Fergus A. Mccorkell, Graham K. Taylor, Richard J. Bomphrey, and

Michael Doube. Iodine vapor staining for atomic number contrast in backscattered electron and X-ray imaging. *Microsc. Res. Tech.*, 77(12):1044–1051, December 2014.

[242] Akira Fujishima and Kenichi Honda. Electrochemical Photolysis of Water at a Semiconductor Electrode. *Nature*, 238(5358):37–38, July 1972. Number: 5358 Publisher: Nature Publishing Group.

[243] Clara Santato, Martine Ulmann, and Jan Augustynski. Photoelectrochemical Properties of Nanostructured Tungsten Trioxide Films. *The Journal of Physical Chemistry B*, 105(5):936–940, February 2001. Publisher: American Chemical Society.

[244] Jong Hyeok Park, O Ok Park, and Sungwook Kim. Photoelectrochemical water splitting at titanium dioxide nanotubes coated with tungsten trioxide. *Applied Physics Letters*, 89(16):163106, October 2006. Publisher: American Institute of Physics.

[245] Tae Woo Kim and Kyoung-Shin Choi. Nanoporous BiVO4 Photoanodes with Dual-Layer Oxygen Evolution Catalysts for Solar Water Splitting. *Science*, 343(6174):990–994, February 2014. Publisher: American Association for the Advancement of Science.

[246] Xiaoxia Chang, Tuo Wang, Peng Zhang, Jijie Zhang, Ang Li, and Jinlong Gong. Enhanced Surface Reaction Kinetics and Charge Separation of p–n Heterojunction Co3O4/BiVO4 Photoanodes. *Journal of the American Chemical Society*, 137(26):8356–8359, July 2015. Publisher: American Chemical Society.

[247] Jae Young Kim, Ganesan Magesh, Duck Hyun Youn, Ji-Wook Jang, Jun Kubota, Kazunari Domen, and Jae Sung Lee. Single-crystalline, wormlike hematite photoanodes for efficient solar water splitting. *Scientific Reports*, 3(1):2681, September 2013. Number: 1 Publisher: Nature Publishing Group.

[248] Kevin Sivula, Florian Le Formal, and Michael Grätzel. Solar Water Splitting: Progress Using Hematite (α-Fe2O3) Photoelectrodes. *ChemSusChem*, 4(4):432–449, 2011. https://onlinelibrary.wiley.com/doi/pdf/10.1002/cssc.201000416.

[249] Shaohua Shen, Sarah A. Lindley, Xiangyan Chen, and Jin Z. Zhang. Hematite heterostructures for photoelectrochemical water splitting: rational materials design and charge carrier dynamics. *Energy & Environmental Science*, 9(9):2744–2775, August 2016. Publisher: The Royal Society of Chemistry.

[250] K. Itoh and J. O'm Bockris. Thin Film Photoelectrochemistry: Iron Oxide. *Journal of The Electrochemical Society*, 131(6):1266, June 1984. Publisher: IOP Publishing.

[251] Niclas Beermann, Lionel Vayssieres, Sten-Eric Lindquist, and Anders Hagfeldt. Photoelectrochemical Studies of Oriented Nanorod Thin Films of Hematite. *Journal of The Electrochemical Society*, 147(7):2456, July 2000. Publisher: IOP Publishing.

[252] S. David Tilley, Maurin Cornuz, Kevin Sivula, and Michael Gratzel. Light-induced water splitting with hematite: Improved nanostructure and iridium oxide catalysis. *Angewandte Chemie International Edition*, 49(36):6405–6408, 2010. https://onlinelibrary.wiley.com/doi/pdf/10.1002/anie.201003110.

[253] Ji-Wook Jang, Chun Du, Yifan Ye, Yongjing Lin, Xiahui Yao, James Thorne, Erik Liu, Gregory McMahon, Junfa Zhu, Ali Javey, Jinghua Guo, and Dunwei Wang. Enabling unassisted solar water splitting by iron oxide and silicon. *Nature Communications*, 6(1):7447, June 2015. Number: 1 Publisher: Nature Publishing Group.

[254] Chun Du, Xiaogang Yang, Matthew T. Mayer, Henry Hoyt, Jin Xie, Gregory McMahon, Gregory Bischoping, and Dunwei Wang. Hematite-Based Water Splitting with Low Turn-On Voltages. *Angewandte Chemie International Edition*, 52(48):12692–12695, 2013. https://onlinelibrary.wiley.com/doi/pdf/10.1002/anie.201306263.

[255] F. J. Morin. Electrical Properties of $\ensuremath{\alpha}{\mathrm{Fe}}_{2}{\mathrm{O} and $\ensuremath{\alpha}{\mathrm{Fe}}_{2}{\mathrm{O}}_{3}$ Containing Titanium. *Physical Review*, 83(5):1005–1010, September 1951. Publisher: American Physical Society.

[256] Nerine J. Cherepy, Dorion B. Liston, Jennifer A. Lovejoy, Hongmei Deng, and Jin Z. Zhang. Ultrafast Studies of Photoexcited Electron Dynamics in γ- and α-Fe_2O_3 Semiconductor Nanoparticles. *The Journal of Physical Chemistry B*, 102(5):770–776, January 1998. Publisher: American Chemical Society.

[257] Stephanie R Pendlebury, Xiuli Wang, Florian Le Formal, Maurin Cornuz, Andreas Kafizas, S. David Tilley, Michael Grätzel, and James R Durrant. Ultrafast Charge Carrier Recombination and Trapping in Hematite Photoanodes under Applied Bias. *Journal of the American Chemical Society*, 136(28):9854–9857, July 2014. Publisher: American Chemical Society.

[258] Woon Yong Sohn, Mika Inaba, Tsuyoshi Tokubuchi, James E. Thorne, Dunwei Wang, and Kenji Katayama. Uncovering Photo-Excited Charge Carrier Dynamics in Hematite (α-Fe_2O_3) Hidden in the Nanosecond Range by the Heterodyne Transient Grating Technique Combined with the Randomly Interleaved Pulse-Train Method. *The Journal of Physical Chemistry C*, 123(11):6693–6700, March 2019. Publisher: American Chemical Society.

[259] Mika Inaba, James E. Thorne, Dunwei Wang, Woon Yong Sohn, and Kenji Katayama. Comparative study of photo-excited charge carrier dynamics of atomic layer deposited and solution-derived hematite films: Dependence of charge carrier kinetics on surface orientations. *Journal of Photochemistry and Photobiology A: Chemistry*, 364:645–649, September 2018.

[260] Monica Barroso, Stephanie R. Pendlebury, Alexander J. Cowan, and James R. Durrant. Charge carrier trapping, recombination and transfer in hematite (α-Fe_2O_3) water splitting photoanodes. *Chemical Science*, 4(7):2724–2734, June 2013. Publisher: The Royal Society of Chemistry.

[261] Stephanie R. Pendlebury, Alexander J. Cowan, Monica Barroso, Kevin Sivula, Jinhua Ye, Michael Grätzel, David R. Klug, Junwang Tang, and James R. Durrant. Correlating long-lived photogenerated hole populations with photocurrent densities in hematite water oxidation photoanodes. *Energy & Environmental Science*, 5(4):6304–6312, March 2012. Publisher: The Royal Society of Chemistry.

[262] Woon Yong Sohn, James E. Thorne, Yaohong Zhang, Shota Kuwahara, Qing Shen, Dunwei Wang, and Kenji Katayama. Charge carrier kinetics in hematite

with NiFeOx coating in aqueous solutions: Dependence on bias voltage. *Journal of Photochemistry and Photobiology A: Chemistry*, 353:344–348, February 2018.

[263] Mika Inaba, Kenji Katayama, and Woon Yong Sohn. Cooperative effects of surface and interface treatments in a hematite (α-Fe_2O_3) photo-anode on its photo-electrochemical performance. *Sustainable Energy & Fuels*, 4(5):2174–2183, May 2020. Publisher: The Royal Society of Chemistry.

[264] Yuchao Zhang, Shiqi Jiang, Wenjing Song, Peng Zhou, Hongwei Ji, Wanhong Ma, Weichang Hao, Chuncheng Chen, and Jincai Zhao. Nonmetal P-doped hematite photoanode with enhanced electron mobility and high water oxidation activity. *Energy & Environmental Science*, 8(4):1231–1236, April 2015. Publisher: The Royal Society of Chemistry.

[265] Kirtiman Deo Malviya, Dino Klotz, Hen Dotan, Dmitry Shlenkevich, Anton Tsyganok, Hadar Mor, and Avner Rothschild. Influence of Ti Doping Levels on the Photoelectrochemical Properties of Thin-Film Hematite (α-Fe_2O_3) Photoanodes. *The Journal of Physical Chemistry C*, 121(8):4206–4213, March 2017. Publisher: American Chemical Society.

[266] Basanth S. Kalanoor, Hyungtak Seo, and Shankara S. Kalanur. Recent developments in photoelectrochemical water-splitting using WO3/BiVO4 heterojunction photoanode: A review. *Materials Science for Energy Technologies*, 1(1):49–62, June 2018.

[267] Jungang Hou, Huijie Cheng, Osamu Takeda, and Hongmin Zhu. Unique 3D heterojunction photoanode design to harness charge transfer for efficient and

stable photoelectrochemical water splitting. *Energy & Environmental Science*, 8(4):1348–1357, April 2015. Publisher: The Royal Society of Chemistry.

[268] Yu Dong, Sheng-You Chen, Yi Lu, Yu-Xuan Xiao, Jie Hu, Si-Ming Wu, Zhao Deng, Ge Tian, Gang-Gang Chang, Jing Li, Silvia Lenaerts, Christoph Janiak, Xiao-Yu Yang, and Bao-Lian Su. Hierarchical MoS2@TiO2 Heterojunctions for Enhanced Photocatalytic Performance and Electrocatalytic Hydrogen Evolution. *Chemistry – An Asian Journal*, 13(12):1609–1615, 2018. https://onlinelibrary.wiley.com/doi/pdf/10.1002/asia.201800359.

[269] Jing Zhang, Qian Xu, Zhaochi Feng, Meijun Li, and Can Li. Importance of the Relationship between Surface Phases and Photocatalytic Activity of TiO2. *Angewandte Chemie International Edition*, 47(9):1766–1769, 2008. https://onlinelibrary.wiley.com/doi/pdf/10.1002/anie.200704788.

[270] Ailong Li, Zhiliang Wang, Heng Yin, Shengyang Wang, Pengli Yan, Baokun Huang, Xiuli Wang, Rengui Li, Xu Zong, Hongxian Han, and Can Li. Understanding the anatase–rutile phase junction in charge separation and transfer in a TiO2 electrode for photoelectrochemical water splitting. *Chemical Science*, 7(9):6076–6082, August 2016. Publisher: The Royal Society of Chemistry.

[271] S. S. Pati, S. Gopinath, G. Panneerselvam, M. P. Antony, and John Philip. High temperature phase transformation studies in magnetite nanoparticles doped with Co2+ ion. *Journal of Applied Physics*, 112(5):054320, September 2012. Publisher: American Institute of Physics.

[272] F. Genuzio, A. Sala, Th. Schmidt, D. Menzel, and H. J. Freund. Phase transformations in thin iron oxide films: Spectromicroscopic study of velocity and shape of the reaction fronts. *Surface Science*, 648:177–187, June 2016.

[273] Matt Bumstead, Kunyu Liang, Gregory Hanta, Lok Shu Hui, and Ayse Turak. DisLocate: Tools to rapidly quantify local intermolecular structure to assess two-dimensional order in self-assembled systems. *Scientific Reports*, 2018.

[274] Mitsuhide Okuda and Kenji Katayama. Selective detection of real and imaginary parts of refractive index change in solutions induced by photoexcitation using near-field heterodyne transient grating method. *Chemical Physics Letters*, 443(1):158–162, July 2007.

[275] Daiki Shingai, Yusuke Ide, Woon Yong Sohn, and Kenji Katayama. Photoexcited charge carrier dynamics of interconnected TiO2 nanoparticles: evidence of enhancement of charge separation at anatase–rutile particle interfaces. *Physical Chemistry Chemical Physics*, 20(5):3484–3489, February 2018. Publisher: The Royal Society of Chemistry.

[276] Aaron M. Jubb and Heather C. Allen. Vibrational Spectroscopic Characterization of Hematite, Maghemite, and Magnetite Thin Films Produced by Vapor Deposition. *ACS Applied Materials & Interfaces*, 2(10):2804–2812, October 2010. Publisher: American Chemical Society.

[277] Maria F. Casula, Young-wook Jun, David J. Zaziski, Emory M. Chan, Anna Corrias, and A. Paul Alivisatos. The Concept of Delayed Nucleation in

Nanocrystal Growth Demonstrated for the Case of Iron Oxide Nanodisks. *Journal of the American Chemical Society*, 128(5):1675–1682, February 2006. Publisher: American Chemical Society.

[278] Igor Chourpa, Laurence Douziech-Eyrolles, Lazare Ngaboni-Okassa, Jean-François Fouquenet, Simone Cohen-Jonathan, Martin Soucé, Hervé Marchais, and Pierre Dubois. Molecular composition of iron oxide nanoparticles, precursors for magnetic drug targeting, as characterized by confocal Raman microspectroscopy. *Analyst*, 130(10):1395–1403, September 2005. Publisher: The Royal Society of Chemistry.

[279] Irina Chamritski and Gary Burns. Infrared- and Raman-Active Phonons of Magnetite, Maghemite, and Hematite: A Computer Simulation and Spectroscopic Study. *The Journal of Physical Chemistry B*, 109(11):4965–4968, March 2005. Publisher: American Chemical Society.

[280] D. Bersani, P. P. Lottici, and A. Montenero. Micro-Raman investigation of iron oxide films and powders produced by sol–gel syntheses. *Journal of Raman Spectroscopy*, 30(5):355–360, 1999. https://onlinelibrary.wiley.com/doi/pdf/10.1002/%28SICI%291097-4555%28199905%2930%3A5%3C355%3A%3AAID-JRS398%3E3.0.CO%3B2-C.

[281] D. L. A. de Faria, S. Venâncio Silva, and M. T. de Oliveira. Raman microspectroscopy of some iron oxides and oxyhydroxides. *Journal of Raman Spectroscopy*, 28(11):873–878, 1997.

[282] M. Ibrahim Dar and S. A. Shivashankar. Single crystalline magnetite, maghemite, and hematite nanoparticles with rich coercivity. *RSC Advances*, 4(8):4105–4113, December 2013. Publisher: The Royal Society of Chemistry.

[283] Prince Saurabh Bassi, Gurudayal, Lydia Helena Wong, and James Barber. Iron based photoanodes for solar fuel production. *Physical Chemistry Chemical Physics*, 16(24):11834–11842, May 2014. Publisher: The Royal Society of Chemistry.

[284] Juan Yao, Junying Chen, Kui Shen, and Yingwei Li. Phase-controllable synthesis of MOF-templated maghemite–carbonaceous composites for efficient photocatalytic hydrogen production. *Journal of Materials Chemistry A*, 6(8):3571–3582, February 2018. Publisher: The Royal Society of Chemistry.

[285] L. B. Hunt. The true story of Purple of Cassius. *Gold Bulletin*, 9(4):134–139, December 1976.

[286] Leslie B Hunt. Gold based glass and enamel colours. *Endeavour*, 5(2):61–67, January 1981.

[287] Huan Li, Fengwei Zhang, Li Guo, Bo Han, Shuai-Ting Yan, and Xian-Ming Zhang. Role of Au–Sn bonding for stabilizing a gold nanocatalyst: a reinvestigation of purple of Cassius. *Dalton Transactions*, September 2022. Publisher: The Royal Society of Chemistry.

[288] Matthias Batzill and Ulrike Diebold. The surface and materials science of tin oxide. *Progress in Surface Science*, 79(2):47–154, January 2005.

[289] Yihong Chen and Matthew W. Kanan. Tin Oxide Dependence of the CO2 Reduction Efficiency on Tin Electrodes and Enhanced Activity for Tin/Tin Oxide Thin-Film Catalysts. *Journal of the American Chemical Society*, 134(4):1986–1989, February 2012. Publisher: American Chemical Society.

[290] J. Watson. The tin oxide gas sensor and its applications. *Sensors and Actuators*, 5(1):29–42, January 1984.

[291] Çetin Kılıç and Alex Zunger. Origins of Coexistence of Conductivity and Transparency in ${\mathrm{SnO}}_{2}$. *Physical Review Letters*, 88(9):095501, February 2002. Publisher: American Physical Society.

[292] Priyanka Chetri and Jay Chandra Dhar. Self-powered UV detection using SnO2 nanowire arrays with Au Schottky contact. *Materials Science in Semiconductor Processing*, 100:123–129, September 2019.

[293] Shih–Chia Chang. Oxygen chemisorption on tin oxide: Correlation between electrical conductivity and EPR measurements. *Journal of Vacuum Science and Technology*, 17(1):366–369, January 1980. Publisher: American Vacuum Society.

[294] Ireneusz Kocemba, Sławomir Szafran, Jacek Rynkowski, and Tadeusz Paryjczak. Relationship between the Catalytic and Detection Properties of SnO2 and Pt/SnO2 Systems. *Adsorption Science & Technology*, 20(9):897–905, November 2002. Publisher: SAGE Publications Ltd STM.

[295] M. Dinesh, R. Ravindran, V. Rukkumani, K. Srinivasan, and M. Saravanakumar. Effect of Oxygen Vacancy on Structural, Optical and Magnetic Behavior of Tin Oxide Nanoparticles. *International Journal of Nanoscience*, 19(01):1850045, February 2020. Publisher: World Scientific Publishing Co.

[296] Pawan Chetri, Biswajit Choudhury, and Amarjyoti Choudhury. Room temperature ferromagnetism in SnO2 nanoparticles: an experimental and density functional study. *Journal of Materials Chemistry C*, 2(43):9294–9302, October 2014. Publisher: The Royal Society of Chemistry.

[297] Nguyen Hoa Hong, Nathalie Poirot, and Joe Sakai. Ferromagnetism observed in pristine $\mathrm{Sn}{\mathrm{O}}_{2}$ thin films. *Physical Review B*, 77(3):033205, January 2008. Publisher: American Physical Society.

[298] Majid Ghanaatshoar, Mehrdad Moradi, and Parsis Tohidi. Surface plasmon resonance enhancement of the magneto-optical Kerr effect in Cu/Co/Ag/SnO2 structure. *The European Physical Journal - Applied Physics*, 68(1):10402, October 2014. Publisher: EDP Sciences.

[299] Hiroshi Yao and Yuki Ishikawa. Finite Size Effect on Magneto-Optical Responses of Chemically Modified Fe3O4 Nanoparticles Studied by MCD Spectroscopy. *The Journal of Physical Chemistry C*, 119(23):13224–13230, June 2015. Publisher: American Chemical Society.

[300] T. M. Chmereva and M. G. Kucherenko. Faraday Effect and Magnetic Circular Dichroism in Media with Magneto-Plasmonic Nanoparticles and Two-Particle Clusters. *Journal of Applied Spectroscopy*, 86(4):698–704, September 2019.

[301] Hiromasa Shimizu, Saori Umetsu, and Terunori Kaihara. Characterization of Transverse Magneto-optic Kerr Effect in Ferromagnetic Metals for Semiconductor Optical Isolators. *Japanese Journal of Applied Physics*, 52(2R):028006, January 2013. Publisher: IOP Publishing.

[302] Archana V.n., Shan Abraham Sam, Aravind Puthirath Balan, and Anantharaman M.r. Magneto-optical properties of a magneto-plasmonic nanofluid based on superparamagnetic iron oxide and gold nanoparticles. *Journal of Magnetism and Magnetic Materials*, 536:168092, October 2021.

[303] D. A. Petrov, R. D. Ivantsov, S. M. Zharkov, D. A. Velikanov, M. S. Molokeev, C. R. Lin, C. T. Tso, H. S. Hsu, Y. T. Tseng, E. S. Lin, and I. S. Edelman. Magnetic and magneto-optical properties of Fe3O4 nanoparticles modified with Ag. *Journal of Magnetism and Magnetic Materials*, 493:165692, January 2020.

[304] Alexander Miles, Yue Gai, Palash Gangopadhyay, Xinyu Wang, Robert A. Norwood, and James J. Watkins. Improving Faraday rotation performance with block copolymer and FePt nanoparticle magneto-optical composite. *Optical Materials Express*, 7(6):2126–2140, June 2017. Publisher: Optica Publishing Group.

[305] Li-Li Xing, Bin He, Zhao-Hui Chen, and Xin-Yu Xue. Schottky barrier and catalytic effect induced high gas sensing of one-step synthesized Pd–SnO2 nanorods. *Solid State Sciences*, 15:42–46, January 2013.

[306] Bongho Jang, Taegyun Kim, Sojeong Lee, Won-Yong Lee, and Jaewon Jang. Schottky Nature of Au/SnO2 Ultrathin Film Diode Fabricated Using Sol–Gel

Process. *IEEE Electron Device Letters*, 39(11):1732–1735, November 2018. Conference Name: IEEE Electron Device Letters.

[307] Andrei Kolmakov, Xihong Chen, and Martin Moskovits. Functionalizing Nanowires with Catalytic Nanoparticles for Gas Sensing Application. *Journal of Nanoscience and Nanotechnology*, 8(1):111–121, January 2008.

[308] S. Basu and P. K. Basu. Nanocrystalline Metal Oxides for Methane Sensors: Role of Noble Metals. *Journal of Sensors*, 2009:e861968, October 2009. Publisher: Hindawi.

[309] Huiqing Fan, Xiaokun Zheng, Qi Shen, Weijia Wang, and Wenqiang Dong. Hydrothermal synthesis and their ethanol gas sensing performance of 3-dimensional hierarchical nano Pt/SnO2. *Journal of Alloys and Compounds*, 909:164693, July 2022.

[310] Yeon-Tae Yu and Prabhir Datta. Examination of Au/SnO2 core-shell architecture nanoparticle for low temperature gas sensing applications. *Sensors and Actuators B: Chemical*, 157(2):444–449, October 2011. Publisher: Elsevier.

[311] Shurong Wang, Yaojie Wang, Junqing Jiang, Rui Liu, Minyan Li, Yanmei Wang, Yan Su, Baolin Zhu, Shoumin Zhang, Weiping Huang, and Shihua Wu. A DRIFTS study of low-temperature CO oxidation over Au/SnO2 catalyst prepared by co-precipitation method. *Catalysis Communications*, 10(5):640–644, 2009.

[312] Mei Lei, Wei Wu, Lingling Sun, Qingyong Tian, Changzhong Jiang, and Xiangheng Xiao. Controlled preparation of hollow SnO2@M (M=Au, Ag) heterostructures through template-assist method for enhanced photocatalysis. *Colloids and Surfaces A: Physicochemical and Engineering Aspects*, 482:276–282, October 2015.

[313] G. Korotcenkov, V. Brinzari, and B. K. Cho. Surface functionalization by gold nanoparticles and its prospects for application in conductometric metal oxide gas sensors. *AIP Conference Proceedings*, 1808(1):020026, March 2017. Publisher: American Institute of Physics.

[314] Lili Wang, Huimin Dou, Zheng Lou, and Tong Zhang. Encapsuled nanoreactors (Au@SnO2): a new sensing material for chemical sensors. *Nanoscale*, 5(7):2686–2691, March 2013. Publisher: The Royal Society of Chemistry.

[315] Amr Ibrahim. Synthesis and characterization of magnetic nanoparticles to incorporate into silicon waveguides to be used as optical isolators.

[316] B. Roldan Cuenya, Sung-Hyeon Baeck, Thomas F. Jaramillo, and Eric W. McFarland. Size- and Support-Dependent Electronic and Catalytic Properties of Au0/Au3+ Nanoparticles Synthesized from Block Copolymer Micelles. *Journal of the American Chemical Society*, 125(42):12928–12934, October 2003. Publisher: American Chemical Society.

[317] Thomas F. Jaramillo, Sung-Hyeon Baeck, Beatriz Roldan Cuenya, and Eric W. McFarland. Catalytic Activity of Supported Au Nanoparticles Deposited from Block Copolymer Micelles. *Journal of the American Chemical Society*, 125(24):7148–7149, June 2003. Publisher: American Chemical Society.

[318] Steven Jay Oldenburg. *Light scattering from gold nanoshells.* Thesis, Rice University, 2000. Accepted: 2009-06-04T06:50:45Z.

[319] Dawson Bonneville. *Low-cost and versatile fabrication of silicon-compatible photonic integrated circuits for active devices and sensors.* Thesis, 2022. Accepted: 2022-10-24T19:50:26Z.

[320] Fatima Abla, Sofian M. Kanan, Yeji Park, Changseok Han, Maria Omastova, Mohamed M. Chehimi, and Ahmed A. Mohamed. Exceptionally redox-active precursors in the synthesis of gold core-tin oxide shell nanostructures. *Colloids and Surfaces A: Physicochemical and Engineering Aspects*, 616:126266, May 2021.

[321] J. F. Scott. Raman Spectrum of SnO2. *The Journal of Chemical Physics*, 53(2):852–853, July 1970. Publisher: American Institute of Physics.

[322] A. Dieguez, A. Romano-Rodriguez, A. Vila, and J. R. Morante. The complete Raman spectrum of nanometric SnO2 particles. *Journal of Applied Physics*, 90(3):1550–1557, August 2001. Publisher: American Institute of Physics.

[323] Jian Zuo, Cunyi Xu, Xianming Liu, Changsui Wang, Chengyun Wang, Yuan Hu, and Yitai Qian. Study of the Raman spectrum of nanometer SnO2. *Journal of Applied Physics*, 75(3):1835–1836, February 1994. Publisher: American Institute of Physics.

[324] A. Diéguez, A. Romano-Rodríguez, J. R. Morante, U. Weimar, M. Schweizer-Berberich, and W. Göpel. Morphological analysis of nanocrystalline SnO2 for

gas sensor applications. *Sensors and Actuators B: Chemical*, 31(1):1–8, February 1996.

[325] C. H Shek, G. M Lin, and J. K. L Lai. Effect of oxygen deficiency on the Raman spectra and hyperfine interactions of nanometer SnO2. *Nanostructured Materials*, 11(7):831–835, October 1999.

[326] L. Z. Liu, X. L. Wu, F. Gao, J. C. Shen, T. H. Li, and Paul K. Chu. Determination of surface oxygen vacancy position in SnO2 nanocrystals by Raman spectroscopy. *Solid State Communications*, 151(11):811–814, June 2011.

[327] Damra E. Mustafa, Tianming Yang, Zhou Xuan, Shizhen Chen, Haiyang Tu, and Aidong Zhang. Surface Plasmon Coupling Effect of Gold Nanoparticles with Different Shape and Size on Conventional Surface Plasmon Resonance Signal. *Plasmonics*, 5(3):221–231, September 2010.

[328] Soonwoo Chah, Matthew R. Hammond, and Richard N. Zare. Gold Nanoparticles as a Colorimetric Sensor for Protein Conformational Changes. *Chemistry & Biology*, 12(3):323–328, March 2005.

[329] Wolfgang Haiss, Nguyen T. K. Thanh, Jenny Aveyard, and David G. Fernig. Determination of Size and Concentration of Gold Nanoparticles from UV-Vis Spectra. *Analytical Chemistry*, 79(11):4215–4221, June 2007. Publisher: American Chemical Society.

[330] Agnieszka Zuber, Malcolm Purdey, Erik Schartner, Caroline Forbes, Benjamin van der Hoek, David Giles, Andrew Abell, Tanya Monro, and Heike Ebendorff-Heidepriem. Detection of gold nanoparticles with different sizes using absorption

and fluorescence based method. *Sensors and Actuators B: Chemical*, 227:117–127, May 2016.

[331] Sabine Szunerits, Jolanda Spadavecchia, and Rabah Boukherroub. Surface plasmon resonance: signal amplification using colloidal gold nanoparticles for enhanced sensitivity. *Reviews in Analytical Chemistry*, 33(3):153–164, October 2014. Publisher: De Gruyter.

[332] Iryna Tokareva, Sergiy Minko, Janos H. Fendler, and Eliza Hutter. Nanosensors Based on Responsive Polymer Brushes and Gold Nanoparticle Enhanced Transmission Surface Plasmon Resonance Spectroscopy. *Journal of the American Chemical Society*, 126(49):15950–15951, December 2004. Publisher: American Chemical Society.

[333] Chia-Chen Chang, Chie-Pein Chen, Tzu-Heng Wu, Ching-Hsu Yang, Chii-Wann Lin, and Chen-Yu Chen. Gold Nanoparticle-Based Colorimetric Strategies for Chemical and Biological Sensing Applications. *Nanomaterials*, 9(6):861, June 2019.

[334] Björn Landeke-Wilsmark, Leif Nyholm, and Carl Hägglund. Seeded Growth of Large-Area Arrays of Substrate Supported Au Nanoparticles Using Citrate and Hydrogen Peroxide. *Langmuir*, 36(24):6848–6858, June 2020.

[335] Funda Aksoy Akgul, Cebrail Gumus, Ali O. Er, Ashraf H. Farha, Guvenc Akgul, Yuksel Ufuktepe, and Zhi Liu. Structural and electronic properties of SnO2. *Journal of Alloys and Compounds*, 579:50–56, 2013.

[336] Michael A. Stranick and Anthony Moskwa. SnO by XPS. *Surface Science Spectra*, 2(1):45–49, January 1993. Publisher: American Vacuum Society.

[337] Davide Barreca, Simona Garon, Eugenio Tondello, and Pierino Zanella. SnO2 Nanocrystalline Thin Films by XPS. *Surface Science Spectra*, 7(2):81–85, April 2000. Publisher: American Vacuum Society.

[338] Fatima Abla, Sofian M. Kanan, Yeji Park, Changseok Han, Maria Omastova, Mohamed M. Chehimi, and Ahmed A. Mohamed. Exceptionally redox-active precursors in the synthesis of gold core-tin oxide shell nanostructures. *Colloids and Surfaces A: Physicochemical and Engineering Aspects*, 616:126266, 2021.

[339] David S. Jensen, Supriya S. Kanyal, Nitesh Madaan, Michael A. Vail, Andrew E. Dadson, Mark H. Engelhard, and Matthew R. Linford. Silicon (100)/SiO2 by XPS. *Surface Science Spectra*, 20(1):36–42, December 2013. Publisher: American Vacuum Society.

[340] Cedric Powell. X-ray Photoelectron Spectroscopy Database XPS,Version 4.1, NIST Standard Reference Database 20, 1989. Type: dataset.

[341] Alexander G. Shard. Practical guides for x-ray photoelectron spectroscopy: Quantitative XPS. *Journal of Vacuum Science & Technology A*, 38(4):041201, July 2020. Publisher: American Vacuum Society.

[342] Alexander Yu. Klyushin, Tulio C. R. Rocha, Michael Hävecker, Axel Knop-Gericke, and Robert Schlögl. A near ambient pressure XPS study of Au oxidation. *Physical Chemistry Chemical Physics*, 16(17):7881–7886, 2014. Publisher: Royal Society of Chemistry.

[343] M. P. Casaletto, A. Longo, A. Martorana, A. Prestianni, and A. M. Venezia. XPS study of supported gold catalysts: the role of Au0 and Au+ species as active sites. *Surface and Interface Analysis*, 38(4):215–218, 2006. https://onlinelibrary.wiley.com/doi/pdf/10.1002/sia.2180.

[344] Aylin Elci, Ozge Demirtas, Ibrahim Murat Ozturk, Alpan Bek, and Emren Nalbant Esenturk. Synthesis of tin oxide-coated gold nanostars and evaluation of their surface-enhanced Raman scattering activities. *Journal of Materials Science*, 53(24):16345–16356, December 2018.

[345] Merve T. Camci, Burak Ulgut, Coskun Kocabas, and Sefik Suzer. In-Situ XPS Monitoring and Characterization of Electrochemically Prepared Au Nanoparticles in an Ionic Liquid. *ACS Omega*, 2(2):478–486, February 2017. Publisher: American Chemical Society.

[346] L. Martinez, A. Mayoral, M. Espineira, E. Roman, F. J. Palomares, and Y. Huttel. Core@shell, Au@TiOx nanoparticles by gas phase synthesis. *Nanoscale*, 9(19):6463–6470, May 2017. Publisher: The Royal Society of Chemistry.

[347] H.-G. Boyen, G. Kästle, F. Weigl, B. Koslowski, C. Dietrich, P. Ziemann, J. P. Spatz, S. Riethmüller, C. Hartmann, M. Möller, G. Schmid, M. G. Garnier, and P. Oelhafen. Oxidation-Resistant Gold-55 Clusters. *Science*, 297(5586):1533–1536, August 2002. Publisher: American Association for the Advancement of Science.

[348] Hannoch Ron and Israel Rubinstein. Alkanethiol Monolayers on Preoxidized Gold. Encapsulation of Gold Oxide under an Organic Monolayer. *Langmuir*, 10(12):4566–4573, December 1994. Publisher: American Chemical Society.

[349] B. Koslowski, H. G. Boyen, C. Wilderotter, G. Kästle, P. Ziemann, R. Wahrenberg, and P. Oelhafen. Oxidation of preferentially (111)-oriented Au films in an oxygen plasma investigated by scanning tunneling microscopy and photoelectron spectroscopy. *Surface Science*, 475(1):1–10, March 2001.

[350] Masato Aizawa and Jillian M. Buriak. Nanoscale Patterning of Two Metals on Silicon Surfaces Using an ABC Triblock Copolymer Template. *Journal of the American Chemical Society*, 128(17):5877–5886, May 2006. Publisher: American Chemical Society.

[351] Gareth L. Nealon, Bertrand Donnio, Romain Greget, Jean-Paul Kappler, Emmanuel Terazzi, and Jean-Louis Gallani. Magnetism in gold nanoparticles. *Nanoscale*, 4(17):5244–5258, August 2012. Publisher: The Royal Society of Chemistry.

[352] T. Rueda, P. de la Presa, and A. Hernando. The influence of thermal annealing on the structural and magnetic properties of gold nanoparticles. *Solid State Communications*, 142(12):676–679, June 2007.

[353] Arne Billen, Amaury de Cattelle, Johanna K. Jochum, Margriet J. Van Bael, Johan Billen, Jin Won Seo, Ward Brullot, Guy Koeckelberghs, and Thierry Verbiest. Novel synthesis of superparamagnetic plasmonic core-shell iron oxide-gold nanoparticles. *Physica B: Condensed Matter*, 560:85–90, May 2019.

[354] Elyahb Allie Kwizera, Elise Chaffin, Yongmei Wang, and Xiaohua Huang. Synthesis and properties of magnetic-optical core–shell nanoparticles. *RSC Advances*, 7(28):17137–17153, March 2017. Publisher: The Royal Society of Chemistry.